LUCCAS KOJI KAVABATA

NUMERICAL INVESTIGATION OF NON-EQUILIBRIUM CONDENSATION OF WET STEAM

São Paulo
2022

LUCCAS KOJI KAVABATA

NUMERICAL INVESTIGATION OF NON-EQUILIBRIUM CONDENSATION OF WET STEAM

Dissertation submitted in fulfillment of the requirements for the degree of Master of Science in Mechanical Engineering

São Paulo
2022

LUCCAS KOJI KAVABATA

NUMERICAL INVESTIGATION OF NON-EQUILIBRIUM CONDENSATION OF WET STEAM

Revised Version

Dissertation submitted in fulfillment of the requirements for the degree of Master of Science in Mechanical Engineering

Field of Study:
Energy and Fluids

Supervisor:
Prof. Dr. Ernani Vitillo Volpe

São Paulo
2022

Este exemplar foi revisado e corrigido em relação à versão original, sob responsabilidade única do autor e com a anuência de seu orientador.

São Paulo, 20 de julho de 2022

Assinatura do autor: Luccas Koji Kavabata

Assinatura do orientador: ____________________

Catalogação-na-publicação

Kavabata, Luccas
Numerical investigation of non-equilibrium condensation of wet steam / L. Kavabata -- versão corr. -- São Paulo, 2022.
110 p.

Dissertação (Mestrado) - Escola Politécnica da Universidade de São Paulo. Departamento de Engenharia Mecânica.

1.Condensação 2.Separador superssônico 3.Método dos momentos 4.Metaestabilidade 5.Geração de entropia I.Universidade de São Paulo. Escola Politécnica. Departamento de Engenharia Mecânica II.t.

ACKNOWLEDGMENTS

Firstly, I would like to thank my supervisor, Prof. E.V. Volpe for guiding me in the course of my Msc degree and for always been available whenever we needed had doubts or wanted to discuss a specific topic. His insights were of the utmost importance in the development of the research of the present work and for all this I am very thankful to him.

I would also like to thank Conselho Nacional de Desenvolvimento Científico e Tecnológico, CNPq, for the M.S. scholarship and acknowledge the full support for the present research provided by CNPq under the Research Grant No. 309985/2013-7.

I gratefully acknowledge support of the RCGI – Research Centre for Gas Innovation, hosted by the University of São Paulo (USP) and sponsored by FAPESP – São Paulo Research Foundation (2014/50279-4) and Shell Brasil, and the strategic importance of the support given by ANP (Brazil's National Oil, Natural Gas and Biofuels Agency) through the R&D levy regulation.

I would also like to thank Prof. S. Oliveira, Prof. J.L.F. Azevedo, and Prof. M.T. Hayashi who have joined our team and have helped us greatly with their knowledge and expertise on the fundamentals of thermodynamics, Computational Fluid Dynamics, and Numerical methods and simulations, respectively. Their help and attention are much appreciated.

A few words of gratitude are now dedicated to all my research colleagues, especially PhD candidate U.A. Silva, for helping me in the first steps of the degree when I knew very little of their research and was as lost and confused as one can possibly be. His help is very much appreciated and it has been an honor working with him for the past three years.

I would like to thank Dr. N.K. Fukumasu and Dr. R. Galdino, who have recently joined our team and have been cooperating with our work. It has been quite a thrilling experience to work, discuss engineering topics and work with them.

I should now thank my dear family. The past few months have been quite harsh on all of us, especially on me. I am afraid I have not been at my best and that I have not been able to give them much joy lately. Yet, they always stood by my side and supported me. Without them, I am quite sure I would not be where I am nor would I have achieve as much as I have. My lack of ability with the words keeps me from saying something more meaningful, so I will simply say thank you, thank very much you for everything.

Finally, but not least important, I would like to thank God for all the wonderful opportunities I have been given in life. Not everybody is as lucky as I am. I regret though that lately I let the hardships get the best of me, but deep inside I am and will always be grateful to You.

”Le temps est la meilleur des critiques; et la patience le meilleur des professeurs.”

-F. Chopin

ABSTRACT

The present MSc dissertation is a part of the supersonic separator project of the Research Center for Gas Innovation (RCGI) of the Polytechnic School of the University of São Paulo. The project aims at researching and developing a supersonic separator which should remove most of the CO_2 contained in natural gas. This is desired since such a device would allow the exploration of natural gas reserves with high CO_2 content given that nowadays the separation process (or processes) involved is rather expensive. The main goal of this research is to investigate the physical consistency of the metastable condensation models available on the branch of the Stanford University Unstructured (SU2) for high-speed condensing flows of a pure vapor under low- and high-pressure conditions in a Laval nozzle. It is also a subject of interest of this research to analyze the entropy generation associated with metastable condensation phenomena which occurs due to the fact that the liquid and vapor phases exchange thermal energy under while being at different temperatures, i.e., heat exchange with temperature difference. Additionally a brief analysis on how the position of the condensation wave is affect by the stagnation conditions has also been performed. The evolution of the liquid phase is evaluated with the use of the method of moments, which replace the continuity equation for the liquid and evaluate statistical quantities such as the average liquid droplet radius, average liquid surface, and average liquid volume, whereas the conservation equations are written for the vapor phase. The nucleation and growth rate models employed were the factor f correction and Hill's growth rate model, respectively. The results obtained from the numerical simulations have shown that the code is able to predict the occurrence of metastable condensation within a certain degree of accuracy. However, the use of the saturation temperature as the trigger for metastable condensation may lead to inaccurate and physically inconsistent results. It has also been found that the process of metastable condensation generates entropy, which is an important aspect to be taken into account in the design of a supersonic separator owing to the fact that this irreversibility cannot be avoided given that metastable condensation must occur in order for the device to be able to remove CO_2 from natural gas.

Keywords – Condensation phenomena, supersonic separator, method of moments, metastability, entropy generation.

LIST OF FIGURES

Figure 1 Supersonic separator device. 18

Figure 2 Schematic representation of the metastable region on a Pressure–Temperature diagram 2. 22

Figure 3 Schematic representation of the thermodynamic processes involved in condensation in a Pressure–Temperature diagram 3a, Isentropic expansion of the vapor phase until the Wilson line is crossed in a Temperature–Entropy diagram. The black line represents the saturation line, the blue line represents the Wilson line, and the red line represents the spinodal line 3b. 23

Figure 4 Schematic plot of ΔG as a function of r as in equation (2.1). 25

Figure 5 Infinitesimal control volume undergoing a condensation process. . . 31

Figure 6 Moses nozzle geometry Moses and Stein (1978) and mesh. 41

Figure 7 Moore nozzle geometry Moore et al. (1973) and mesh. 42

Figure 8 Flow properties for Moses case 2. 46

Figure 9 P/P_0, average droplet radius, critical radius, and nucleation rate along with the moment of order zero. 47

Figure 10 Two-phase fluid stagnation enthalpy, supersaturation rate, and entropy generated for Moses case 2. 49

Figure 11 Flow properties for Moore B nozzle. 51

Figure 12 P/P_0 and average droplet radius along with the moment of order zero. 52

Figure 13 Two-phase fluid stagnation enthalpy, supersaturation rate, and entropy generated for Moore B nozzle. 53

Figure 14 Flow properties for a high-pressure nozzle flow. 56

Figure 15 P/P_0 and average droplet radius along with the moment of order zero. 57

Figure 16 Two-phase fluid stagnation enthalpy, supersaturation rate, and entropy generated in a high-pressure flow. 58

Figure 17 Plot of the supersaturation rate and moment of order zero along the length of the nozzle. 59

Figure 18 P/P_0 comparison for different stagnation pressures. 61

Figure 19 μ_0 and average droplet radius obtained for different stagnation pressures. 62

Figure 20 P/P_0 comparison for different stagnation pressures. 63

Figure 21 μ_0 and average droplet radius obtained for different stagnation temperatures. 64

Figure 23 Liquid droplet intersected by the control surface, reproduced from Young (1995). 94

LIST OF TABLES

Table 1 Boundary conditions for the simulation of the case 2 of Moses Moses and Stein (1978). 41

Table 2 Boundary conditions for the simulation of the Moore B nozzle. . . . 42

Table 3 Boundary conditions for the simulation of the Moses nozzle Moses and Stein (1978) under high-pressure conditions. 42

Table 4 Residuals obtained for the simulation of the case 2 of Moses Moses and Stein (1978). 45

Table 5 Residuals obtained for the simulation of Moore B nozzle. 50

Table 6 Residuals obtained for the simulation of the nozzle of Moses under high-pressure conditions. 54

Table 7 Residuals obtained for the stagnation pressure analysis simulations. . 60

Table 8 Residuals obtained for the stagnation temperature analysis simulations. 63

Table 9 Relations used to transform $\Delta G(r)$ into $\Delta G(g)$ 81

Table 10 Integration by parts relations 101

Table 11 Moses Moses and Stein (1978) nozzle geometry 107

Table 12 Moore B nozzle Moore et al. (1973) geometry obtained from Yang and Shen (2009). 108

LIST OF SYMBOLS

α_r	surface heat transfer coefficient of a critical droplet
ΔG_c	Critical Gibbs free energy
ΔT_s	Supercooling
ℓ	Mean free path
γ	Isentropic specific heat ratio
λ_v	Vapor thermal conductivity
μ_v	Vapor viscosity
ρ_d	Condensate density
ρ_l	Liquid density
ρ_v	Vapor density
σ	Surface tension
C_g	Condensation rate
C_g	Molecular rate of condensation on a g-mer
C_gc	Critical molecular rate of condensation on a g-mer
C_p^v	Vapor phase specific heat under constant pressure
E_g	Evaporation rate
G	Growth rate
g	Number of molecules in a cluster
g_c	Critical number of molecules in a cluster
H_e	Specific enthalpy of evaporation
h_v	Liquid enthalpy

h_v	Vapor enthalpy
J	Nucleation rate
J_f	Nucleation rate with the correction factor f
Kn	Knudsen number
M	Mach number
m	Mass of a molecule
n_1	Number of monomers per unit volume
n_1	number of monomers per unit volume
n_g	Number of g-mers per unit volume
n_g	number of g-mers per unit volume
P_l	Liquid pressure
$P_S(T_v)$	Saturated vapor pressure at temperature T_v
P_v	Vapor pressure
q_c	Condensation coefficient
q_e	Evaporation coefficient
R	Gas constant per unit mass
r	Droplet radius
r_c	Critical droplet radius
S	Supersaturation ratio
T_l	Liquid temperature
$T_s(P)$	Saturated vapor temperature at pressure P
T_v	Vapor temperaturee
T_W	Wilson temperature
T_{sat}	Dew temperature
Z	Zeldovich factor

CONTENTS

Dissertation overview **14**

1 Introduction **15**

1.1 Sources of energy . . . 15

1.2 The supersonic separator . . . 17

1.3 Scope of the present work . . . 19

2 Literature review **21**

2.1 Condensation phenomena . . . 21

2.1.1 The physics of condensation . . . 21

2.1.2 Nucleation rate model . . . 26

2.1.3 Growth rate model . . . 27

2.2 Equations for condensing flows of a pure vapor . . . 28

2.2.1 Vapor phase . . . 28

2.2.2 Liquid phase . . . 28

2.2.3 Two-phase fluid equations . . . 30

2.2.4 Entropy generation in metastable condensation . . . 30

2.3 The method of moments . . . 32

2.3.1 Hill's method of moments . . . 34

2.3.2 The approach of White and Hounslow (2000) . . . 35

3 Methods **38**

3.1 Numerical model . . . 38

3.2 Test cases . . . 40

3.2.1 Condensation of wet-steam under low-pressure conditions . . . 41

3.2.1.1 Moses & Stein nozzle 41

3.2.1.2 Moore B nozzle 41

3.2.2 Condensation of wet-steam under high-pressure conditions 42

3.2.3 Variation of the position of the condensation wave with respect to the stagnation conditions 43

4 Results and discussion **44**

4.1 Condensation of wet-steam under low-pressure conditions 44

4.1.1 Moses & Stein nozzle 44

4.1.2 Moore B nozzle 49

4.2 Condensation of wet-steam under high-pressure conditions 54

4.3 Variation of the position of the condensation wave with respect to the stagnation conditions 60

4.3.1 Stagnation pressure analysis 60

4.3.2 Stagnation temperature analysis 62

5 Conclusions **65**

5.1 Concluding remarks 65

5.2 Future work 67

Bibliography **70**

Appendix A – The ΔG expression **78**

Appendix B – Nucleation rate models **80**

B.1 The Classical Nucleation Theory (CNT) 81

B.2 Non-Isothermal correction 83

B.3 The Internally Consistent Classical Theory (ICCT) 84

B.4 The correction factor f 84

Appendix C – Growth rate models **86**

C.1 Fundamentals of growth rate models 86

C.2 Young's model 87

C.3 Gyarmathy's model 88

C.4 Hertz-Knudsen model 88

C.5 Hill's model 89

Appendix D – Conservation equations **90**

D.1 Droplet conservation equation 91

D.2 Mass conservation equation 92

D.3 Momentum equations 94

D.4 Energy conservation equation 95

D.5 Entropy production rate equation 97

D.6 Final remarks 97

Appendix E – The method of moments equations **99**

Appendix F – SU2 thermodynamic models for wet-steam and water **103**

F.1 Saturation pressure model 103

F.2 Saturation temperature model 104

F.3 Liquid temperature model 104

F.4 Liquid density model 105

F.5 Liquid enthalpy model 105

F.6 Surface tension model 106

Appendix G – Nozzle geometry **107**

G.1 Moses & Stein Moses and Stein (1978) 107

G.2 Moore B nozzle Moore et al. (1973) 108

DISSERTATION OVERVIEW

The following dissertation aims at investigating the physics of metastable condensation which occurs in supersonic separators. As the real problem is quite complex and difficult to tackle, the present work focuses on Euler flows of a single component. The working fluid of choice is wet steam owing to the fact that there are more data available in the literature for this fluid for both low- Moore et al. (1973); Moses and Stein (1978) and high-pressure cases Gyarmathy (2005) and also due to the fact that many models, e.g., nucleation rate, droplet growth rate, etc, have been calibrated for wet-steam.

A previous investigation by Costa (2020) has tested and validated the accuracy of these models for the condensation of wet-steam under low pressure conditions. The present dissertation shall focus on whether these models are able to produce physically consistent results, i.e., if the numerical results are in accordance with the theory of metastable condensation. Such a study is important to improve the understanding of the phenomena as well as to analyze the physical consistency of the models and of the results before moving on to more complex cases such as gas mixtures.

This dissertation is structured as follows: an introduction, which gives an overview of the context of the research; a literature review, which explains the main theoretical aspects of this work; a methods section, which provides details of the numerical test cases performed; a results section which shows and analyses the numerical results obtained; a conclusion section, which summarizes the main results and outlines next steps which may be followed in future research projects.

1 INTRODUCTION

1.1 Sources of energy

Energy is an important aspect of life in the 21st century. Most of the devices that have been developed, e.g., computers, cars, smartphones, airplanes and so forth, require a power source in order to work. To put it in other words, these devices require an energy supply.

For a long time oil and coal have been used and they are still among the main sources of energy. The combustion of these sources, however, release pollutants such as CO_2, NO_x, CO, primary SO_2 and particulate matter and they are reported to have harmful effects on the environment and to human health since they may for instance contribute to global warming, e.g., CO_2, acid rain, e.g., H_2S and SO_2, and decrease the air quality, e.g., particulate matter. As concerns over environmental matters grow, researchers have been working on developing new technologies and on exploring other sources of energy Liang et al. (2012).

An alternative that seems to be a promising one is natural gas which - according to Liang et al. (2012) - is the cleanest of fossil fuels - and can be a intermediate solution as new and cleaner sources of energy are developed Machado et al. (2012). The advantages of using natural gas are Liang et al. (2012) the fact that its emissions of CO_2 as well as other greenhouse gases are lower than those of oil and coal (lower carbon-fingerprint Machado et al. (2012)), it could reduce the occurrence of acid rain due to the fact that its emissions of NO_x and SO_2 are lower when compared to oil and coal, and it could improve the air quality since it produces lower levels of particulate matter Liang et al. (2012). The interested reader may refer to Table 1 from Liang et al. (2012) for further details.

Natural gas is found in reserves in the crust of the earth and its chemical composition varies depending on the reserve from where it is extracted. Natural gas consists mainly of saturated hydrocarbons, such as CH_4 Liang et al. (2012). As reported by Liang et al. (2012) and Cao and Bian (2019), H_2O, acid components, CO and H_2S, heavy hydrocarbons, and other chemical components are also found in natural gas and these components are regarded as impurities.

As reported by Cao and Bian (2019), the impurities found in natural gas, e.g., CO_2, H_2S, H_2O, heavy hydrocarbons, etc, have deleterious effects. Acid components, for instance, in the presence of water may result in corrosion of the pipelines. Another example is the fact that these impurities result in an increase in energy loss during transportation of the natural gas. Furthermore, when natural gas is extracted from reserves its chemical composition rarely satisfies the specifications required for commercial use of the gas. Thus it is necessary to separate these impurities from natural gas.

The presence of such impurities is one of the issues regarding the exploration of natural gas. Some natural gas reserves, for example, present high amounts of acid components and, to this date, it is not economically viable to explore such reserves due to the high costs involved in the separation processes. According to Imaev et al. (2014), it is estimated that around 30% of natural gas reserves around the world have high amounts of CO_2 while Machado et al. (2012) reports that around 10% of the natural gas reserves contain 15% to 80% mol CO_2. An example is the Natuna field in Indonesia, which is reported Imaev et al. (2014) to contain around 70% of CO_2 by volume.

Most separation technologies are based on chemical-absorption, physical-absorption, adsorption, membrane permeation or supersonic separation processes Machado et al. (2012). As stated by Imaev et al. (2014) absorption and adsorption processes are not suitable to be used for gas mixtures with high content of CO_2. Membrane processes can be used for separating CO_2 as well as other impurities. However, for high concentrations of CO_2 the complexity of the process increases considerably as well as its the energy costs.

According to Cao and Bian (2019); Imaev et al. (2014), supersonic separation processes - low-temperature processes that are based on the condensation of water, heavy carbons and acid components - seem to be one of the most promising technologies for removing acid components, as well as heavy hydrocarbons and water, from natural gas. The condensation phenomena that take place in such supersonic separators are the subject of this work.

1.2 The supersonic separator

The supersonic separator is a device in which a swirling gaseous mixture is accelerated to supersonic speed in a converging-diverging (Laval) nozzle. As the gas is accelerated part of its enthalpy is turned into kinetic energy Imaev et al. (2014) and this involves a rapid cooling of the gas mixture and, as a result of the temperature drop, some of its components condense Machado et al. (2012).

It is possible to separate undesirable components from natural gas using the principles previously stated. In this case a gas mixture containing CH_4, CO_2, and other impurities flow past a swirl device and then into the nozzle, as can be seen in figures 1b and 1c. In the convergent section the gas is accelerated until it reaches the sonic condition, i.e., Mach number equal to one ($M = 1$), at the throat of the nozzle. Pressure and temperature drop simultaneously as the velocity increases.

In the divergent section of the nozzle the gas continues to be accelerated and both pressure and temperature continue to fall. At a certain point the conditions for condensation are met, and some of the components of the gas mixture may condense. It is in the divergent section that condensation takes place. It is also in this section that shock waves may occur. The newly formed liquid phase is then centrifuged to the inner walls of the nozzle where it will be removed through collectors. A representation of the supersonic separator is illustrated in figure 1a.

As reported by Imaev et al. (2014), for Mach numbers slightly higher than one, i.e., between 1.3 and 1.5 Imaev et al. (2014), it is possible to achieve sufficiently low temperatures as to cause components heavier than ethane to condense. Thus, under these conditions the condensation of acid components such as CO_2 and H_2S can take place, thus making it possible to separate them from natural gas through the collectors. Since shock waves may occur in the nozzle, it is necessary that the collectors be placed before them since they lead to a increase of the flow temperature and pressure whereas decreasing the Mach number; in such cases the liquid phase may re-evaporate and the removal of the condensed components is no longer possible Machado et al. (2012).

The main advantage of the supersonic separator lies in the fact that it does not release CO_2 into the atmosphere, since the CO_2 that is removed from natural gas may be reinjected into the reservoir. Some of its other advantages include the fact that there are no moving nor rotating parts Cao and Bian (2019); Imaev et al. (2014), the device is relatively small Imaev et al. (2014) and its operational cost is relatively low Imaev et al.

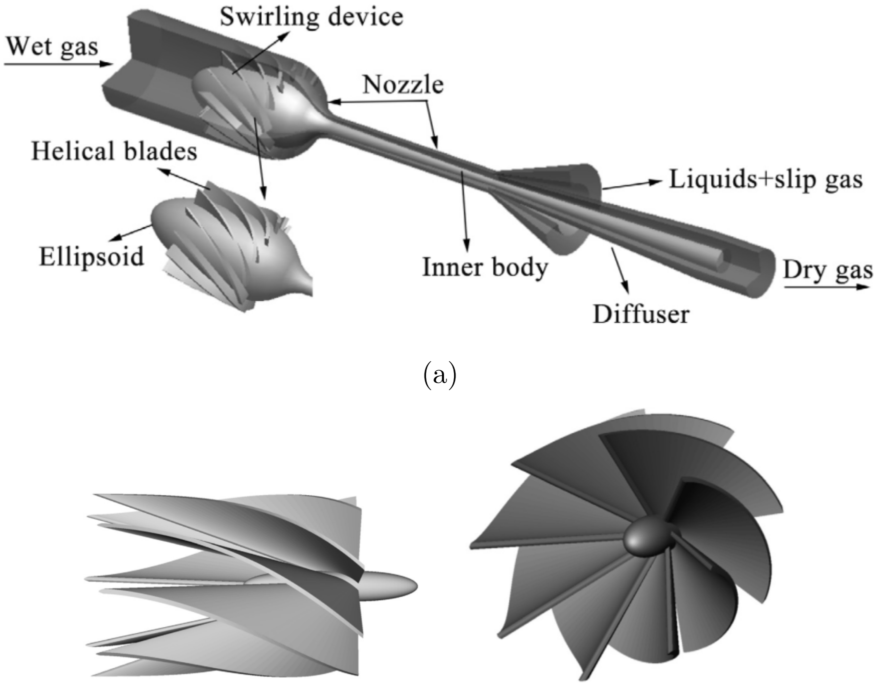

(a)

(b) (c)

Figure 1: 1a Schematic representation of a supersonic separator, reproduced from Wen et al. (2016), 1b side view of a swirling device, reproduced from Beaubert et al. (2015), and 1c frontal view of a swirling device, reproduced from Beaubert et al. (2015).

(2014). An economical and environmental analysis of the supersonic technology can be found in Machado et al. (2012).

According to Cao and Bian (2019) two main designs of supersonic separator are commercially available. One of the designs is the *Twister I* developed by Twister BV. The other one is the *Supersonic Separator* (3S) developed by ENGO. These designs differ in the position of the swirling device. In Twister I, the swirling device is placed downstream from the Laval nozzle whereas in the 3S the device is placed upstream from the Laval nozzle.

The position of the swirling device affects the flow pattern. If positioned after the Laval nozzle, the flow first reaches the supersonic condition and then it flows through the swirling device. It is reported Cao and Bian (2019) that the oblique shock waves that are formed in this case are somewhat difficult to be controlled and even if they are controlled the pressure recovery in this setup is limited - which results in an increase in energy loss.

The swirling device can also be placed before the Laval nozzle. In this case the flow that enters the nozzle is a swirling one. In the converging section it is subsonic, then it is accelerated to supersonic condition at the nozzle throat. According to Cao and Bian

(2019), condensation and swirl occur simultaneously in the nozzle - as opposed to the first case. It is reported Cao and Bian (2019) that this reduces the re-evaporation effect and it also improves the efficiency of the separator in removing CO_2 from natural gas. For further details on the supersonic separator device the interested reader may refer to Cao and Bian (2019); Imaev et al. (2014).

In spite of the fact that the principles of the supersonic separator are well known, its design, i.e., the swirling device used and its position, nozzle geometry, the working conditions, the efficiency in separating CO_2 from natural gas, and so forth, may vary - as is the case of *Twister I* and *3S*. Hence there are topics related to the supersonic separator that still need to be researched, improved or optimized.

The Research Center for Gas Innovation (RCGI) - of the Polytechnic School of the University of São Paulo (POLI-USP) - in partnership with Shell are developing a supersonic separator device and are studying topics related to it such as shape optimization, the effects of the swirl in the flow, condensation phenomena and so forth.

1.3 Scope of the present work

The present work was developed at the Polytechnic School of the University of São Paulo (POLI-USP) and was funded by the National Council of Scientific and Technological Development (CNPq) for the M.S. scholarship and acknowledge the full support for the present research provided by CNPq under the Research Grant No. 309985/2013-7. This project is part of the RCGI – Research Centre for Gas Innovation, hosted by the University of São Paulo (USP) and sponsored by FAPESP – São Paulo Research Foundation (2014/50279-4) and Shell Brasil, and the strategic importance of the support given by ANP (Brazil's National Oil, Natural Gas and Biofuels Agency) through the R&D levy regulation.

The main goal of the RCGI is to develop a supersonic separator device. On considering that a study and a research on the full problem, which involves the full Navier-Stokes equations with a suitable turbulence model to simulate a multi-phase flow of a swirling gas mixture in a a Laval nozzle, is quite a challenging task, it has been decided to break the problem into simpler ones, e.g., condensation of single phase flows, Euler flows both in the presence and in the absence of swirl, and so forth.

The research developed in this dissertation focuses on numerical simulations of metastable condensation of a pure vapor in high-speed nozzle flows. The choice for single phase flow is due to the fact that experimental data for the condensation of $CH_4 - CO_2$ is not readily available - most of the data is available on the topic is for wet-steam - and it was one of the objectives of the present research to analyze and to discuss the physical consistency of these thermodynamic models for condensation before moving on to more complex flows, i.e., metastable condensation of one or more components of a gas mixture.

In the present context only Euler flows have been analyzed since main objective is to understand and investigate the thermodynamics and the physics of condensing nozzle flows. The working fluid considered is wet steam and the main objectives are to analyze and to perform numerical simulation in order to try to understand the physics of the phenomena, e.g., the entropy generation, how the position of the condensation wave may vary with respect to the boundary conditions, and the differences between condensation under low- and high-pressure conditions.

In the context of Euler flows, entropy may be generated as a result of shockwaves or because of metastable condensation. The present work focuses only on the generation of entropy due to metastable condensation. Entropy generation due to shockwaves is a classical result which has been previously discussed and analyzed and is beyond the scope of the present work.

The contributions of this work were to analyze the physical consistency of condensation models, i.e., whether the condensation models are in agreement with the theory of metastable condensation, to discuss and to simulate the generation of entropy which occurs in metastable condensation, to add the contribution of the nucleation rate to the mass source term, and implement the growth rate model of Hill on the code.

The author of this dissertation has also taken part in writing papers - as co-author of three conference papers Cato et al. (2021); Cavalcante et al. (2020); Costa et al. (2020) and as main author in one conference paper Kavabata et al. (2021). The papers were presented on the *18th Brazilian Congress of Thermal Sciences and Engineering* (ENCIT 2020) Cavalcante et al. (2020); Costa et al. (2020), on the *International Council of Aeronautical Sciences* (ICAS) Cato et al. (2021), and on the *26th International Congress of Mechanical Engineering* (COBEM 2021) Kavabata et al. (2021).

The CFD code used in this work is a branch of the Stanford University Unstructured (SU2) Economon et al. (2015) code that has been further developed by the Flight Performance and Propulsion research group from Technische Universiteit Delft (TU Delft) Azzini (2019). More specifically, the branch that we used was the *feature_turbo2phase* Azzini (2019) which is available for download at Azzini (2018).

2 LITERATURE REVIEW

2.1 Condensation phenomena

2.1.1 The physics of condensation

Phase change phenomena may occur in several engineering applications such as compressors and supersonic separators. In the former case, it is undesirable since liquid droplets may have a negative effect on the service life of certain components such as the blades of the compressor Azzini (2019); Lettieri et al. (2017) whereas in the latter case, it is essential for the separation process. Therefore, understanding when this phenomena may occur is of the utmost importance in order to either prevent it from occurring or to make sure it occurs.

Condensation is a phase change phenomena that occurs when a gaseous substance turns into liquid. This process may occur in equilibrium or in non-equilibrium conditions. The first case is related to the saturation temperature (T_{sat}), whereas the latter is related to the Wilson temperature (T_W) - which is defined as the point of maximum supercoolingLettieri et al. (2017). The occurrence of the phenomena may be observed experimentally. One such possibility is through the use of Schlieren Method Lettieri et al. (2017); Simons and Bowen (1946).

These temperatures (T_{sat} and T_W) define when condensation is triggered, that is, under equilibrium conditions condensation starts when the vapor temperature T reaches T_{sat}. On the other hand, in non-equilibrium conditions condensation begins when T reaches T_W. Additionally, condensation may occur as a result of homogeneous or heterogeneous nucleation. In the former case, liquid droplet are formed in the bulk of the flow whereas in the latter case the droplets begin to form at the carrier gas, impurity particles or nozzle walls, i.e., the new phase may form at any interface. In high-speed nozzle flows the main nucleation mechanism is the homogeneous nucleation Azzini (2019). Therefore, the following discussions shall focus on this mechanism.

According to Azzini (2019), the Wilson temperature and the saturation temperature are related by the following inequality $T_W < T_{sat}(P_v)$, where P_v is the vapor pressure. If the vapor has temperature T such that $T_W < T < T_{sat}(P_v)$, then the vapor is said to be metastable, which is the orange region that lies between the saturation and Wilson lines in figure 2. The concept of metastability and metastable region, which is illustrated in figure 2, is an important one to understand the physics of non-equilibrium condensation since phase should occur in the aforementioned region

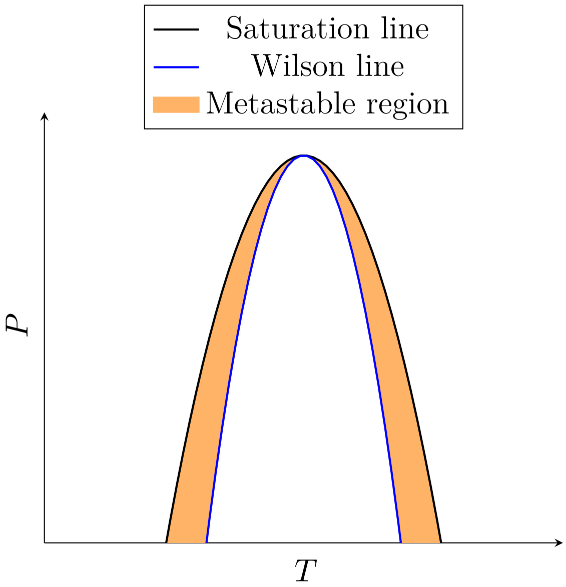

Figure 2: Schematic representation of the metastable region on a Pressure–Temperature diagram 2.

As stated by Azzini (2019); Lettieri et al. (2017), metastable condensation does not readily occur when the vapor reaches the saturation temperature, as indicated by phase diagrams, but rather when the vapor reaches the Wilson temperature. This fact is illustrated in figure 3 in which a schematic representation of metastable condensation is shown in figure 3a in a $P - T$ diagram and a representation of the isentropic expansion of the vapor until it reaches the Wilson line is shown in a $T - S$ diagram, figure 3b.

As reported by Lettieri et al. (2017) under non-equilibrium conditions, the vapor at point I, figures 3a and 3b, goes through isentropic expansion until it reaches point II in line AB that separates the gas and liquid phases, i.e., the saturation line. At that point the gas becomes supersaturated but it does not condense. For the phase change to take place it must keep on expanding isentropically until it becomes supersaturated, point III, which is when the vapor crosses the Wilson line. From this point on the assumption of isentropic expansion is dropped as thermal energy is exchanged between the phases with temperature difference, which leads to the generation of entropy.

Once the metastable vapor crosses the Wilson line it condenses forming liquid droplets and it releases latent which results in an increase in local pressure and temperature. According to Azzini (2019) due to curvature effects both pressure and temperature of the newly formed liquid phase are greater than those of the vapor phase. That is $T_l > T_v$ and $P_l > P_v$ where T_l and T_v denote the liquid and vapor temperatures, respectively, and P_l and P_v denote the liquid and vapor pressures, respectively.

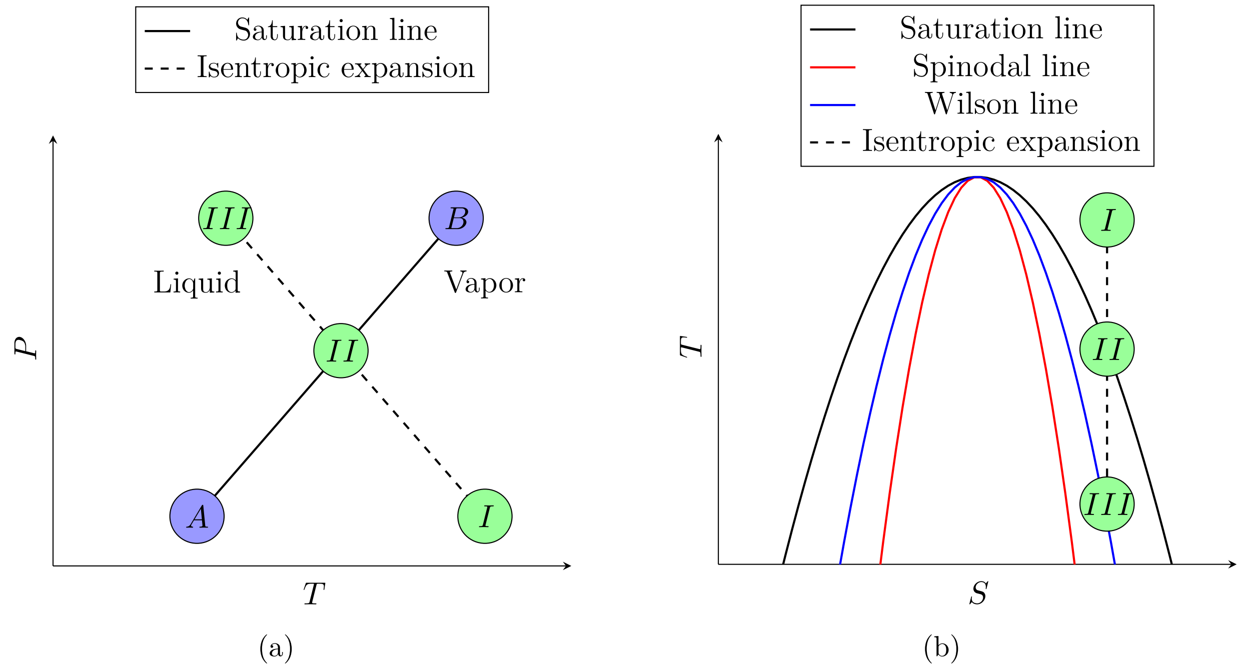

(a)

(b)

Figure 3: Schematic representation of the thermodynamic processes involved in condensation in a Pressure–Temperature diagram 3a, Isentropic expansion of the vapor phase until the Wilson line is crossed in a Temperature–Entropy diagram. The black line represents the saturation line, the blue line represents the Wilson line, and the red line represents the spinodal line 3b.

From a physical point of view, clusters of molecules can be formed in the flow and they are constantly acquiring and loosing molecules. If the clusters are too small they tend to evaporate. On the other hand, if they are big enough they tend to grow to form the liquid phase. The criteria that defines whether a cluster will dissolve or grow is the critical radius - here denoted as r_c.

It is then necessary to find an expression for the critical radius. This expression is based on the work required to form a spherical droplet (ΔG) of radius r. According to Bakhtar et al. (2005) this work is a reversible one and, by assuming that the vapor behaves as a perfect gas,Bakhtar et al. (2005) one has

$$\Delta G = -\frac{4}{3}\pi r^3 \rho_l R T_v \ln\left(\frac{P_v}{P_S(T_v)}\right) + 4\pi r^2 \sigma \tag{2.1}$$

Where ρ_l is the liquid density, R is the gas constant per unit mass, T_v is the vapor temperature, P_v is the vapor pressure, $P_S(T_v)$ is the saturated vapor pressure at temperature T_v, and σ is the surface tension.

Equation (2.1) presents two terms: 1) a volumetric term which is negative and a 2) surface term which is positive. The interested reader may refer to appendix A for a detailed deduction of equation (2.1).

The Gibbs free energy function (2.1) has a maximum (ΔG_c) that occurs at the so called critical radius (r_c), which is obtained by differentiating (2.1) with respect to r.

The critical radius is given by

$$r_c = \frac{2\sigma}{\rho_l R T_v \ln \varsigma} \tag{2.2}$$

where ς[1] is the supersaturation rate, which is defined as

$$\varsigma \equiv \frac{P_v}{P_S(T_v)} \tag{2.3}$$

where P_v stands for vapor pressure and $P_S(T_v)$ represents saturated vapor pressure at the vapor temperature T_v.

For a non-ideal gas, the expression of the critical radius is a bit more complex than the one in equation (2.1). Some authors Bakhtar and Zidi (1990); Bakhtar et al. (2005) suggest the use of a truncated virial equation to obtain a more suitable expression for non-ideal gases. The present work uses the expression presented by Azzini (2019), which is given by

$$r_c = \frac{2\sigma}{\rho_l dG_v - (P_v - P_{sat}(T_v))} \tag{2.4}$$

where dG_v is given by

$$dG_v = G_v(P_v, T_v) - G_v(P_sat(T_v), T_v) \tag{2.5}$$

The critical Gibbs free energy for an ideal gas is given by

$$\Delta G_c = \frac{4}{3}\pi r_c^2 \sigma \tag{2.6}$$

The critical radius is of significant importance because it makes it possible to establish a criterion to determine whether liquid droplets will shrink, i.e., evaporate, and when it

---

[1] In the literature, the supersaturation rate is often denoted by the letter S. However, preference has been given to ς in order to avoid interpreting S as entropy.

will grow, i.e., condensate. If the droplet radius r is less than the critical radius ($r < r_c$), it to evaporate in order to reduce the Gibbs free energy of the system. On the other hand if the droplet radius of is greater than the critical radius ($r > r_c$) than it tends to grow and form the liquid phase.

The situation previously described is illustrated in figure 4. The critical droplet radius may be expressed as in equation (2.2) for illustration purposes. It has a maximum point, indicated by the green dot in figure 4, which is an energy barrier that must be overcome in order for condensation to take place. This barrier represents the regions in which the liquid phase is stable and unstable. For droplet radii less than the critical value, the liquid phase is unstable whereas for radii greater than the critical value, it is stable.

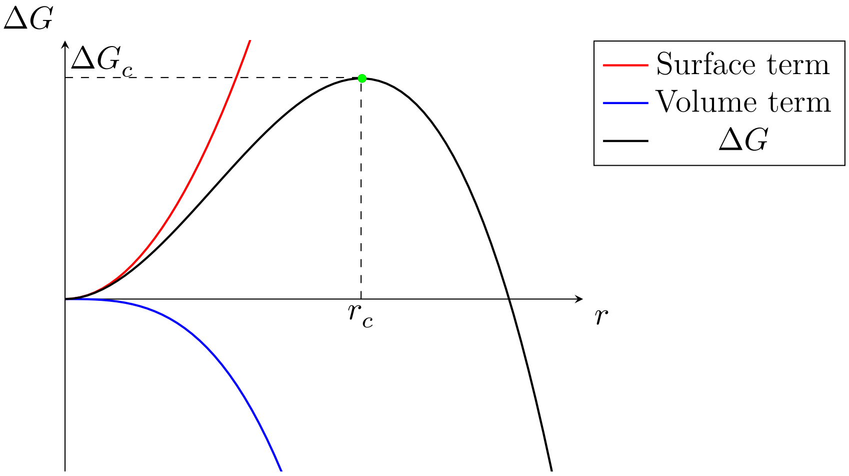

Figure 4: Schematic plot of ΔG as a function of r as in equation (2.1).

An analysis of the supersaturation rate ς is also important owing to the fact that it indicates the metastable region of the flow . If ς is a value between zero and one ($0 < \varsigma < 1$), then the reversible work required to form a spherical droplet is always positive ($\Delta G > 0$)and the nucleation of liquid droplets does not occur under these circumstances. However, if $\varsigma > 1$ the vapor phase is supersaturated, the flow is considered to be metastable, and under this condition nucleation may occur Bakhtar et al. (2005); Hric and Halama (2016). Note that the supersaturation rate does not predict when condensation occurs. Instead, it provides information related to the metastable region as well as where it is possible to occur metastable condensation and it is not. It is possible then to conclude that for condensation to occur it is necessary that the supersaturation ratio be strictly greater than one ($\varsigma > 1$) and that the droplet average radius be greater than the critical radius ($r > r_c$).

The simulation of the liquid phase requires a set of equations to evaluate its evolution as well as a closure model for the nucleation of droplets with critical size (J) and for the rate at which they grow, i.e., droplet growth rate (G). The models for nucleation and growth rate employed in the present work are presented briefly in the next subsections while the evolution of the liquid phase is discussed in the following section.

2.1.2 Nucleation rate model

The rate at which liquid droplets with critical size are formed, i.e., the nucleation rate (J), may be written in the following general form

$$J = \left(\frac{1}{1+\Phi}\right) q_c \frac{\rho_g^2}{\rho_l} \left(\frac{2\sigma}{\pi m^3}\right) \exp\left(-f \frac{4\pi\sigma}{3kT_v} r_c^2\right) \tag{2.7}$$

where q_c is the condensation coefficient, usually taken to be equal to unity, ρ_v is the vapor density, ρ_l is the liquid density, σ is the surface tension, m is the mass of a molecule, k is the Boltzmann constant, T_v is the vapor temperature, f is a correction factor, and r_c is the critical radius.

For the present research, the nucleation model adopts $f = 1.33$ and Φ is equal to the following expression

$$\Phi = 2\left(\frac{\gamma-1}{\gamma+1}\right) \frac{h_{lv}}{RT_v} \left(\frac{h_{lv}}{RT_v} - \frac{1}{2}\right) \tag{2.8}$$

where γ is the ratio of specific heats, R is the gas constant, h_{lv} is the difference between the specific vapor and specific liquid enthalpies, $h_v - h_l$, where h_v and h_l are the specific vapor and specific liquid enthalpies, respectively. This model is referred to as factor f correction Choi et al. (2017); Costa (2020); Grübel et al. (2018) and it is reported to be the nucleation rate model that produces the best results.

This model adds a correction factor $f = 1.33$ in the exponential term of the so-called Non-isothermal nucleation rate (J_{NonIso}) - this model is obtained by taking Φ to be equal to equation (2.8) and $f = 1$. Both the J_{NonIso} and the factor f models take into account the fact that the vapor and liquid phases are not in thermodynamic equilibrium when condensation takes place.

A brief description of some of the main nucleation rate models found in the literature is given in appendix (B). For a more comprehensive discussion on the topic, the interested reader may refer to Bakhtar et al. (2005).

The condensation coefficient (q_c) in equation (2.7) expresses the ratio between the molecules that collide with the droplet surface and are absorbed to the total number of molecules that collide with the droplet surface. If $q_c = 1.0$, for example, then all the molecules that collide with the droplet surface are absorbed. On the other hand if $q_c = 0.5$ then 50% of the molecules that collide with the droplet surface are absorbed whereas the other 50% are reflected.

According to Bakhtar et al. (2005), for the condensation of water vapor using the Non-isothermal correction the value of the condensation coefficient varies between $0.1 \leqslant q_c \leqslant 1.0$. Therefore it is possible that the condensation coefficient value could influence the numerical results.

2.1.3 Growth rate model

In order to simulate condensation phenomena it is also requires to model for the growth of liquid droplets that have acquired critical size. Models for representing the growth of liquid droplets are commonly referred to as growth rate. Different growth rate models have been proposed by different authors. An interesting discussion of these models can be found Luijten (1998); Peeters et al. (2001); Young (1982). A brief review of the main growth rate models in the literature can also be found in appendix C.

The growth rate model used for the simulations of the present work is the one proposed by Hill Hill (1966). The growth rate will be denoted as dr/dt. In the literature the notation G and $\dot{r}$ are sometimes used to represent the growth rate.

As reported by Starzmann et al. (2018), the most appropriate growth rate model to be used with the method of moments is Hill's growth rate model. Additionally, this model was proposed for a free molecular regime, i.e., large Knudsen numbers and small droplets, which is one of the hypothesis of the present investigation: liquid droplets are sufficiently small that phase slip can be neglected.

$$\left.\frac{dr}{dt}\right|_{Hill} = \frac{2q_c}{(2-q_c)}\frac{m}{\rho_l\sqrt{2\pi m k}}\left[\frac{P_v}{\sqrt{T_v}} - \frac{P_{sat}(T_v)}{\sqrt{T_l}}\right] \tag{2.9}$$

where m is the mass of a molecule, R is the gas constant, k the Boltzmann constant, and the Knudsen number (Kn) is given by

$$Kn = \frac{\lambda}{2r} \tag{2.10}$$

where λ is the mean free path of vapor molecules and r is the droplet radius.

2.2 Equations for condensing flows of a pure vapor

2.2.1 Vapor phase

The general case of condensing flows is that of a gas mixture which is composed of an inert gas and pure vapor where the liquid phase is composed of polydispersed droplets Young (1995). For high-speed condensing flows the main nucleation mechanism is the homogeneous one and phase change occurs when the vapor phase is supersaturated. According to Young (1995), for such case it is possible to assume that the liquid droplets are spherical and small in size. Note, that the liquid phase may be composed of droplets of different sizes, i.e., these assumptions allow the possibility of a droplet size distribution.

The present work focuses on high-speed condensing flows of pure vapor, i.e., single component multi-phase flow. For such case the equations presented in Put (2003); Young (1995) may be simplified to take into account only the vapor and liquid phases. The aim of this section is to provide the basic relationships for compressible flows of a gas-droplet single component substance. The following derivations are applicable to both two- and three-dimensional problems Young (1995).

The vapor phase is taken to be the continuum phase whereas the liquid phase is considered to be discontinuous which is composed of polydispersed spherical droplets. Furthermore, droplet-droplet interactions are neglected, on assuming that the volume fraction of the liquid droplets is small. Also, the effects of viscosity and thermal conductivity are considered only for inter-phase transfer processes Young (1995).

2.2.2 Liquid phase

The equations for the liquid droplets have been formulated by Young (1995) and follow the surface formulation of Gibbs. Hence, the model adopted assumes that gas-droplet system is composed of spherical droplets whose surface thickness is equal to zero. At the droplet surface there is a discontinuous change of properties, which are assumed to be constant in the vicinity of the surface for both phases. Also, the liquid phase model assumes thermodynamic equilibrium between the droplet surface temperature and the bulk temperature, which means that the surface temperature is equal to the bulk temperature.

As reported by Young (1995), the energy and entropy of a liquid droplet can be split into two terms, namely a bulk and a surface term as follows

$$E_l = E_{b,l} + E_{s,l} = \frac{4}{3}\pi\langle r\rangle^3\rho_l e_b + 4\pi\langle r\rangle^2 e_{s,l} \tag{2.11a}$$

$$S_l = S_{b,l} + S_{s,l} = \frac{4}{3}\pi\langle r\rangle^3\rho_l s_b + 4\pi\langle r\rangle^2 s_{s,l} \tag{2.11b}$$

Where $e_{b,l}$ and $s_{b,l}$ denote the the bulk energy and entropy per unit mass, respectively, and the terms $e_{s,l}$ and $s_{s,l}$ denote the energy and entropy per unit surface area, respectively, and and $\langle r\rangle$ is the average droplet radius.

Note that equations (2.11a) and (2.11b) are not written in the same way as in Young (1995). This is due to the fact that Young (1995) considers a group of n_i spherical liquid droplets per unit mass and writes equations (2.11a) and (2.11b) for each one of the i droplets. In the present work, this is not necessary since the method of moments is being employed to obtain an average droplet radius which is used to evaluate equations (2.11a) and (2.11b). On dividing equations (2.11a) and (2.11b) by $4\pi\rho_l\langle r\rangle^3/3$ one obtains the energy and entropy per unit mass of liquid.

The mechanical equilibrium condition between the liquid droplet and the vapor phase at pressure P_v is given by

$$P_l = P_v + \frac{2\sigma}{\langle r\rangle} \tag{2.12}$$

where P_l is the liquid droplet pressure, which is assumed to be uniform in the droplet, σ is the surface tension or surface free energy per unit area. According to Young (1995), this equations should hold for non-equilibrium conditions as well. Note that the terms surface energy (e_s) and surface free energy (σ) are not to be confused.

As reported by Young (1995), the enthalpy per unit mass of the liquid phase may be defined as

$$h_l \equiv e_l + \frac{P_v}{\rho_l} \tag{2.13}$$

Alternatively, it is possible to write the liquid specific enthalpy in terms of the vapor enthalpy as follows

$$h_l = h_v - h_{lv} = h_v - (h_{v,sat} - h_{l,sat}) \tag{2.14}$$

where $h_{v,sat}$ and $h_{l,sat}$ are the specific enthalpy of the vapor and of the liquid evaluated at the saturation line, respectively.

2.2.3 Two-phase fluid equations

This section focuses on the equations for the vapor and liquid phases together, which shall be referred to as two-phase fluid. Properties such as density, enthalpy, entropy, etc, can be written for each individual phase as well as for the two-phase fluid.

Let y be the wetness fraction, which is defined as the ratio between the mass of liquid and the mass if vapor plus liquid Young (1995). The mass fraction of vapor is thus $(1-y)$. By denoting the vapor density as ρ_v, the liquid density as ρ_l, one can obtain an average density for the two-phase fluid (ρ_m) which is given by Azzini (2019); Young (1995)

$$\frac{1}{\rho_m} = \frac{1-y}{\rho_v} + \frac{y}{\rho_l} \tag{2.15}$$

or, in terms of specific volume of the two-phase fluid ν_m, one has

$$\nu_m = (1-y)\nu_v + y\nu_l \tag{2.16}$$

where ν_v and ν_l denote the vapor and liquid specific volumes, respectively.

The specific enthalpy of the two-phase fluid (h_m) can be expressed analogously as Young (1984)

$$h_m = (1-y)h_v + yh_l \tag{2.17}$$

where $(1-y)$ is the mass fraction of the vapor phase, h_v and h_l are the specific enthalpies of the vapor and liquid phases, respectively.

The specific stagnation enthalpy for the two-phase fluid for an steady and adiabatic flow can be expressed as follows Young (1984)

$$H_m = (1-y)h_v + yh_l + \frac{\bar{u}_i\bar{u}_i}{2} \tag{2.18}$$

where $\bar{u}_i$ is the common velocity between the vapor and liquid phases. Note that equation (2.18) assumes that the relative velocity between the vapor and liquid is zero, i.e., no-slip between the phases.

2.2.4 Entropy generation in metastable condensation

The following analysis is based on Azzini (2019); Bakhtar et al. (2005) and on the notes of Prof. E. V. Volpe.

Irrevesibilities may arise in inviscid and adiabatic condensing flows due to irreversible heat and mass transfer, which may occur as a result of the temperature difference between the vapor and liquid phases Young (1984). This process is referred to as thermodynamic loss. Also, according to Young (1984), the supercooling, i.e., the difference between the saturation temperature and the vapor temperature, expresses a measure of deviation from the thermal equilibrium.

Consider the flow of a pure vapor in a steady processes, such that the mass flow rate $\dot{m}$ and the rate of vapor that condenses $\delta\dot{m}$ can be considered constant. Also, the kinetic and potential energy terms are assumed to be negligible and the pure vapor is assumed to behave as an ideal gas. The present analysis shall focus on Euler flows, i.e., inviscid flows no heat transfer, i.e., $\nu = 0$ and $\kappa = 0$ inside the control volume.

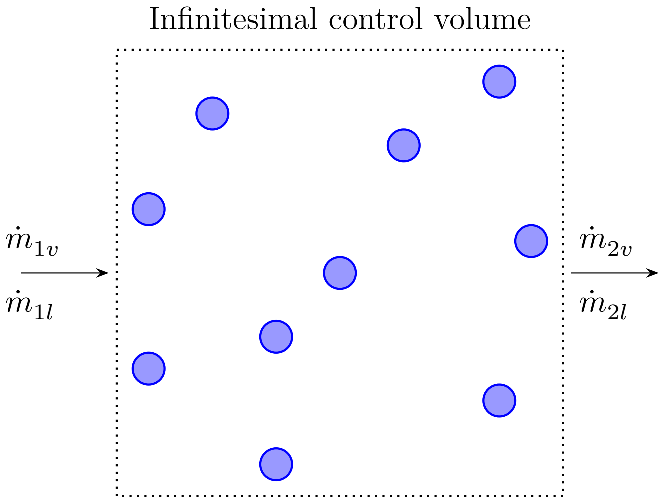

Figure 5: Schematic representation of an infinitesimal control volume undergoing a condensation process.

The mass flow rate that enters the control volume $\dot{m}$ is equal to the mass flow rate that leaves the control volume such that

$$\dot{m} = \dot{m}_{1v} + \dot{m}_{1l} = \dot{m}_{2v} + \dot{m}_{2l} \tag{2.19}$$

where $\dot{m}_{1v}$ and $\dot{m}_{1l}$ are the vapor and liquid flow rates that enters the control volume, $\dot{m}_{2v}$ and $\dot{m}_{2l}$ are the vapor and liquid flow rates that leave the control volume. A schematic representation of the infinitesimal control volume is shown in figure 5.

According to Bakhtar et al. (2005), four processes are involved in metastable condensation. The vapor phase undergoes an isentropic expansion of the pure vapor from pressure P to P_{sat}, the formation of spherical liquid droplets which requires work to be done, and the isentropic compression of the liquid phase. Condensation occurs at constant pressure and temperature (P_{sat}, T_{sat}) with $\Delta G = 0$ and during this process, thermal energy is exchanged between the vapor and liquid phases.

Once metastable condensation occurs the liquid and vapor phases are at different temperatures, T_{sat} and T_v, respectively, and the exchange of thermal energy takes place with temperature difference, which results in generation of entropy.

The second law of thermodynamics for an Euler problem can be written as follows

$$\delta q = T(dS + \delta \dot{S}_{irr}) \tag{2.20}$$

where q is the heat transfer, dS is the entropy variation, and $\delta \dot{S}_{irr}$ is the entropy generated.

On applying the second law to the control volume in figure 5 is given by

$$\begin{array}{rll} \delta \dot{m} \dfrac{h_{lv}}{T_v} & = \dot{m}_{2v} s_{2v} - \dot{m}_{1v} s_{1v} + \dot{s}_v & \text{(vapor contribution)} \\ -\delta \dot{m} \dfrac{h_{lv}}{T_{sat}} & = \dot{m}_{2l} s_{2l} - \dot{m}_{1l} s_{1l} + \dot{s}_l & \text{(liquid contribution)} \\ \hline \end{array}$$

$$\delta \dot{m} h_{lv} \left(\frac{1}{T_v} - \frac{1}{T_{sat}} \right) = \dot{m}_{1v}(s_{2v} - s_{1v}) + \dot{m}_{1l}(s_{2l} - s_{1l}) + \delta \dot{m}(s_{2l} - s_{2v}) + \dot{s}_v + \dot{s}_l \tag{2.21}$$

Note that

$$\dot{m}_{2v} = \dot{m}_{1v} - \delta \dot{m} \tag{2.22a}$$

$$\dot{m}_{2l} = \dot{m}_{1l} + \delta \dot{m} \tag{2.22b}$$

Equation (2.21) is similar to equation (D.28), appendix D, the difference being that the latter is written in differential form. The final form of the entropy generation equation is given by

$$\dot{S} = \dot{s}_v + \dot{s}_l = \delta \dot{m}(h_v - h_l) \left(\frac{1}{T_v} - \frac{1}{T_{sat}} \right) \tag{2.23}$$

where $\dot{S}$ is the entropy generated.

Note that according to equation (2.23), in Euler flows, the only mechanism of entropy generation, apart from shock-waves, is the exchange of thermal energy between the vapor and liquid which occurs with each phase being at a different temperature. If both phases were at the same temperature the entropy generation term would then become zero.

2.3 The method of moments

Liquid droplets may vary both in size and mass, which means there is a distribution of droplet sizes. The droplet size is an important aspect, since they may flow with the vapor phase if they are sufficiently light and small. On the other hand, if the droplets are large and heavy, they do not flow along with the vapor phase, i.e., there may be slip between the phases and separation effects may occur Azzini (2019). In the present research it is considered that the liquid droplets are small enough so that they flow along with the vapor phase, i.e., no-slip between the phases is assumed.

One of the ways to evaluate the evolution of the liquid phase is through the so-called method of moments. The method consists on evaluating the statistical moments of the droplet size probability density function (p.d.f.). Several papers discuss the application of this method to the condensation problem Afzalifar et al. (2017); Hagmeijer (2004); Luo et al. (2006, 2018); Put (2003); White and Hounslow (2000). The following section is dedicated to explaining the use of this method as proposed by Hill (1966).

A modification of the method was proposed by McGraw (1997), and it is based on the quadrature method to solve one of the integrals in the moment equations. This quadrature based method is termed Quadrature Method of Moments (QMOM). A thorough discussion of the QMOM is beyond the scope of the present work and the interested reader may refer to Afzalifar et al. (2017); Gerber and Mousavi (2007); McGraw (1997); Mousavi et al. (1920) for further details.

A rigorous treatment of the mathematical description of the method of moments can be found in Papoulis and Pillai (2002). The method is also illustrated for a different fluid mechanics application in the famous books by Monin and Yaglom (2013a,b). The reader who wants to study the method of moments in more details is advised to refer to these books.

An alternative method to evaluate the evolution of the liquid phase is the so called Eulerian-Lagrangian method Dykas and Wróblewski (2011); Young (1991, 1995). In this case the vapor conservation equations are written in an Eulerian reference frame whereas the liquid phase equations are written in a Lagragian reference frame. The continuous droplet radius distribution is discretized and the droplets are divided by size, i.e., droplets with the same radius belong to the same group. The reason why the method of moments has been chosen instead of the Eulerian-Lagrangian method is due to the computational cost, .i.e., the latter has lower computational cost than the former.

2.3.1 Hill's method of moments

Before proceeding to the equations it is worth to highlight the main hypothesis that are made in order to deduce the moment equations.

Firstly, coagulation and segregation effects are neglected. Secondly, mechanical equilibrium, i.e., there is no slip between the vapor and liquid phase, is assumed. Thirdly, it is considered that the growth rate (dr/dt) is not a function of the droplet radius (r). Fourthly, it is assumed that the liquid density is constant.

It is possible to deduce the method of moments from the General Dynamic Equation (GDE) which is a function of space ($\vec{x}$) and droplet radius r. The GDE is able to describe the evolution of the droplet radius distribution. For a detailed study of the GDE the interested reader may refer to Gelbard and Seinfeld (1979). Here we simply present the GDE.

$$\frac{\partial f}{\partial t} + \frac{\partial}{\partial r}\left(f\frac{dr}{dt}\right) + \frac{\partial (f u_i)}{\partial x_i} = J\delta(r - r_c) \tag{2.24}$$

Where f is the radius distribution function, J is the nucleation rate, δ is the Dirac delta distribution and dr/dt is the growth rate.

The distribution function is defined in terms of the droplet number density $n(r, \vec{x}, t)$, which expresses the number of droplets whose radius are smaller than r_c, as follows

$$f(r, \vec{x}, t) \equiv \frac{\partial n(r, \vec{x}, t)}{\partial t} \tag{2.25}$$

On multiplying equation (2.24) by r^n and then by integrating it with respect to r from 0 to ∞ one obtains the moment equations - a more detailed deduction of the moment equations - which is based on Put (2003) - is given in appendix E.

$$\frac{\partial \mu_k}{\partial t} + \frac{\partial (\mu_k u_i)}{\partial x_i} = J r_c^k + k\frac{dr}{dt}\mu_{k-1} \tag{2.26}$$

where

$$\mu_k \equiv \int_0^\infty r^k f dr \qquad (k = 0, 1, ...) \tag{2.27}$$

is referred to as the moment of order k or the kth order moment.

The moment equations (2.26) can be used to calculate as many moments as necessary. In the context of condensation the zeroth order moment ($k = 0$) as well as the first three moments ($k = 1, 2, 3$) are calculated and the following set of equations is obtained.

$$\frac{\partial \mu_0}{\partial t} + \frac{\partial(\mu_0 u_i)}{\partial x_i} = J \tag{2.28a}$$

$$\frac{\partial \mu_1}{\partial t} + \frac{\partial(\mu_1 u_i)}{\partial x_i} = J r_c + \mu_0 \frac{dr}{dt} \tag{2.28b}$$

$$\frac{\partial \mu_2}{\partial t} + \frac{\partial(\mu_2 u_i)}{\partial x_i} = J r_c^2 + 2\mu_1 \frac{dr}{dt} \tag{2.28c}$$

$$\frac{\partial \mu_3}{\partial t} + \frac{\partial(\mu_3 u_i)}{\partial x_i} = J r_c^3 + 3\mu_2 \frac{dr}{dt} \tag{2.28d}$$

This method was first proposed by Hill Hill (1966). The set of equations (2.28a) through (2.28d)., however, are not in the form originally proposed by Hill Hill (1966). In order obtain Hill's original method it is necessary to define the liquid or net moment (Q_k) as follows

$$\mu_k \equiv \rho Q_k \tag{2.29}$$

It is possible to obtain the moment equations using a slightly different approach which is to express the liquid mass fraction as a function of time. In this case the liquid moments will be integrals over time instead of integrals over the droplet radius. It has been proven Hagmeijer (2004) that both derivations are equivalent.

Some references Hill (1966); Put (2003) write the equation (2.28d) in terms of the liquid mass fraction y, since it is related to μ_3 by the following relation Azzini (2019); White and Hounslow (2000)

$$y = \frac{4}{3}\pi \rho_l \mu_3 \tag{2.30}$$

2.3.2 The approach of White and Hounslow (2000)

It is possible to obtain the moment equations in a slightly different form from equation (2.28) White and Hounslow (2000). Let $\mathbf{X}_p$ be a four dimensional phase space with three space coordinates plus a coordinate associated with the droplet size r. Let this phase space be defined as follows

$$\mathbf{X}_p = \begin{bmatrix} x_1 \\ x_2 \\ x_3 \\ r \end{bmatrix}; \tag{2.31}$$

On differentiating $\mathbf{X}_p$ with respect to time, one obtains the phase velocity $\mathbf{u}_p$, which is then given by

$$\mathbf{u}_p = \begin{bmatrix} dx_1/dt \\ dx_2/dt \\ dx_3/dt \\ dr/dt \end{bmatrix}; \tag{2.32}$$

On writing the droplet conservation equation, in integral form, one has

$$\iiint_{\vartheta} (\rho_m f) dV + \oiint_{\Omega} (\rho_m f) u_{p,i} dS_i = \iiint_{\vartheta} \rho_m J dV \tag{2.33}$$

On applying Gauss theorem to equation (2.33), one obtains the differential form of the droplet conservation equation

$$\frac{\partial(\rho_m f)}{\partial t} + \frac{\partial(\rho_m f u_{p,i})}{\partial X_{p,i}} = \rho_m J \tag{2.34}$$

where the term $\partial/\partial X_{p,i}$ is given by White and Hounslow (2000)

$$\frac{\partial}{\partial X_{p,i}} = \frac{\partial}{\partial x_1} + \frac{\partial}{\partial x_2} + \frac{\partial}{\partial x_3} + \frac{\partial}{\partial r} \tag{2.35}$$

Equation (2.34) can be rewritten in a more convenient way

$$\frac{\partial(\rho_m f)}{\partial t} + \frac{\partial(\rho_m f u_{p,i})}{\partial x_i} + \frac{\partial}{\partial r}\left(\rho_m f \frac{dr}{dt}\right) = \rho_m J \tag{2.36}$$

Now, the procedure is the same of the previous section. Equation (2.36) is multiplied by r^k and integrated from 0 to ∞, which leads to the final form on the nth order moment equation

$$\frac{\partial(\rho_m \mu_k)}{\partial t} + \frac{\partial(\rho_m \mu_k u_{p,i})}{\partial x_i} = k\rho_m \int_0^{\infty} r^{k-1}\left(f\frac{dr}{dt}\right) dr + \rho_m J r_c^k \tag{2.37}$$

The moment equations in the form of equation (2.37) were implemented on the SU2 branch by Azzini (2018, 2019).

Equations (2.37) have closure if the growth rate term can be written in the following form

$$\frac{dr}{dt} = a_0 + a_1 r \tag{2.38}$$

where a_0 and a_1 are functions of the vapor properties.

The variables μ_k are not the actual moments of the distribution f since this distribution is not normalized - it is not an actual p.d.f., that is, a probability density function. In order to obtain these quantities, the variables μ_n must be normalized with respect to the normalization condition, namely the μ_0. The same notation used by Hagmeijer (2004) shall be used here to denote the nth order moment

$$\langle r^k \rangle \equiv \frac{\mu_k}{\mu_0} \tag{2.39}$$

The four moments needed to simulate the evolution of the liquid phase have their own meaning. The zeroth order moment is related to the total number of droplets, the first order moment is related to the average droplet radius, the second order moment is related to the total droplet surface, and the third order moment is related to the total droplet volume and is related to the liquid mass fraction through equation (2.30)

3 METHODS

3.1 Numerical model

An equation of state is needed to perform the simulations. The present work aims at studying both low- and high-pressure condensing flows - while the former may allow assuming ideal gas behavior, the former does not since the gas behavior may deviate considerably from the ideal gas model under high pressure conditions - an EoS for non-ideal gases was chosen.

The Peng-Robinson-Stryjek-Vera EoS Stryjek and Vera (1986), which is a modification of the original Peng-Robinson EoS Peng and Robinson (1976) was the chosen equation. The use and study of other equations of state which are capable of predicting more accurately non-ideal gas behavior has been the subject of research in recent years in papers Kluwick (2017); Pini et al. (2017) and a dissertation by Nederstigt (2017), just to name a few examples.

Non-ideal gas behavior, as well as the different models available, have been the subject of great interest in recent years. The interested reader may refer, for instance, to Leal et al. (2019) for a comprehensive discussion on multi-parameters EoS and to Aursand et al. (2017) for a discussion on cubic EoS, which is the case of the PRSV EoS.

As for the system of equation to be solved, one must take the moment equations into account along with the conservation equations in order to simulate condensation and the evolution of the liquid phase.

The conservation equations for the vapor phase, for a two-dimensional Euler problem, can be written in conservation form as follows Azzini (2019)

$$\frac{\partial \mathbf{U}}{\partial t} + \frac{\partial \mathbf{F}_x}{\partial x} + \frac{\partial \mathbf{F}_y}{\partial y} = \mathbf{S} \tag{3.1}$$

where

$$\mathbf{U}=\begin{bmatrix}\rho_v\\ \rho_v u\\ \rho_v v\\ \rho E_{0,v}\end{bmatrix};\mathbf{F}_x=\begin{bmatrix}\rho_v u\\ \rho_v u^2+P\\ \rho_v uv\\ H_{0,v}u\end{bmatrix};\mathbf{F}_y=\begin{bmatrix}\rho_v v\\ \rho_v uv\\ \rho_v v^2+P\\ H_{0,v}v\end{bmatrix};\mathbf{S}=\begin{bmatrix}S_v\\ S_v u\\ S_v v\\ S_v H_{0,l}\end{bmatrix}; \tag{3.2}$$

where $\rho E_{0,v}$ is the total energy of the vapor phase per unit volume, $H_{0,v}$ is the stagnation enthalpy of the vapor phase, $H_{0,l}$ is the stagnation enthalpy of the liquid phase, and S_m is the term that models the mass exchange between the vapor and liquid phases and is given by Azzini (2019)

$$S_v=-\left[\rho_m\frac{3y}{\langle r\rangle}\frac{dr}{dt}+\frac{4}{3}\pi\rho_l r_c^3 J\right] \tag{3.3}$$

where ρ_m is the two-phase fluid density, given by equation (2.15), y is the liquid mass fraction, $\langle r\rangle$ is the droplet average radius, ν_l is the specific volume of the liquid phase, ν_v is the specific volume of the vapor phase, and dr/dt is the droplet growth rate Azzini (2019). A discussion on the conservation equations for condensing flows can be found in appendix D as well as in Dykas and Wróblewski (2011); Young (1995).

Equation (3.3) added the term related to the nucleation rate to the mass source term. Originally, this term accounted for the term related to the growth rate (first term on the right hand side of (3.3)) Azzini (2019). However, research on the topic has suggested that a second nucleation rate related term may be needed Dykas and Wróblewski (2011); Luo et al. (2018).

The numerical method used for the conservation equations is a modification of Roe's Upwind scheme Hirsch (2007); Roe (1981) for non-ideal EoS which was developed by Vinokur and Montagné (1990) and was implemented on SU2 by Vitale et al. (2015).

The moment equations for the liquid phase can also be written in conservation form as follows

$$\frac{\partial\mathbf{W}}{\partial t}+\frac{\partial\mathbf{H}_x}{\partial x}+\frac{\partial\mathbf{H}_y}{\partial y}=\mathbf{S}_\mu \tag{3.4}$$

where

$$\mathbf{W}=\begin{bmatrix}\rho_m\mu_0\\ \rho_m\mu_1\\ \rho_m\mu_2\\ \rho_m\mu_3\end{bmatrix};\mathbf{H}_x=\begin{bmatrix}\rho_m\mu_0 u\\ \rho_m\mu_1 u\\ \rho_m\mu_2 u\\ \rho_m\mu_3 u\end{bmatrix};\mathbf{H}_y=\begin{bmatrix}\rho_m\mu_0 v\\ \rho_m\mu_1 v\\ \rho_m\mu_2 v\\ \rho_m\mu_3 v\end{bmatrix};\mathbf{S}_\mu=\begin{bmatrix}\rho_m J\\ \rho_m J r_c+\mu_0 G\\ \rho_m J r_c^2+2\mu_1 G\\ \rho_m J r_c^3+3\mu_2 G\end{bmatrix}; \tag{3.5}$$

where r is the droplet radius, $\mathbf{x}$ represents the spatial coordinates, t is the time coordinate, and $f(\mathbf{x}, r, t)$ is the droplet radius distribution function Hagmeijer (2004); Put (2003). Note that $(\mathbf{x}, r)$.

The numerical scheme for the moment equations is that of Rusanov Rusanov (1961), which is also an upwind scheme, and was implemented on SU2 by Azzini (2019).

The conservation and moment equations are weakly coupled and the liquid temperature is evaluated by using the capillarity model, which is given by Azzini (2019)

$$T_l = T_{sat}(P) - (T_{sat}(P) - T_v)\frac{r_c}{\langle r \rangle} \tag{3.6}$$

The liquid and vapor phases are assumed to be in mechanical and kinematic equilibrium, i.e., $P_l \approx P_v$ and their velocity fields are also the same Azzini (2019); Dykas and Wróblewski (2011). As for the kinematic equilibrium hypothesis, it is assumed that the liquid droplets are small enough so that they have negligible inertia and as a consequence, they flow along with the vapor phase.

The saturation pressure (P_{sat}) and temperature (T_{sat}) as well as other thermodynamic models are given in appendix F.

3.2 Test cases

Three sets of numerical simulations were performed in order to obtain the desired results. In all of them the Euler equations were employed with the following boundary conditions: 1) steady state flows, 2) adiabatic wall, i.e., no heat transfer between the nozzle and the surroundings, 3) the static back pressure was set to $0.25P_0$ for all flows, which corresponds to the supersonic outlet condition. Furthermore all the meshes used for the present work were unstructured ones and the mesh elements were triangles.

The first set consists of metastable condensation under low-pressure conditions and two well-known cases were simulated: Moses case 2 and Moore B nozzle. The second set consist of a simulation under high-pressure condition using Moses nozzle and the third set consists of simulations in which the stagnation conditions were varied in order to verify how such variations affected the position of the condensation wave. The following subsections provide a detailed explanation of the set of simulations performed.

3.2.1 Condensation of wet-steam under low-pressure conditions

3.2.1.1 Moses & Stein nozzle

The following results were obtained using the nozzle geometry of Moses & Stein Moses and Stein (1978), figure 6, with an unstructured mesh of approximately 25k elements, also shown in figure 6. The algorithm for generation of the mesh was the frontal-Delauney Remacle et al. (2010) and a total of 10k iterations were needed to obtain convergence. The nozzle throat is located at approximately $x \approx 0.0622$ (m). Further details of the nozzle geometry, i.e., the (x, y) coordinates of the points, can be found in appendix G, section G.1.

The case simulated was case 02 of Moses and Stein (1978), with a stagnation pressure of approximately 0.4 bar, stagnation temperature of 366.15 K and the back pressure was set to $0.25P_0$. The parameters of the numerical setup and boundary conditions are summarized in table 1.

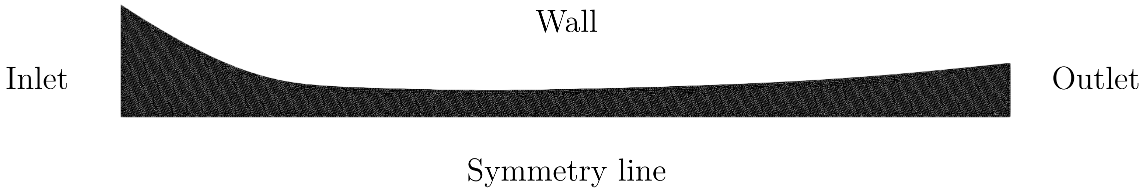

Figure 6: Moses nozzle geometry Moses and Stein (1978) and mesh.

Table 1: Boundary conditions for the simulation of Moses case 2.

P_0 (bar)	T_0 (K)	P_b (bar)	EoS	Mesh size	Mesh type	Nozzle throat
0.4	366.15	$0.25P_0$	PRSV	25k	Unstructured	0.0622

3.2.1.2 Moore B nozzle

A low-pressure simulation was performed using Moore B nozzle geometry Moore et al. (1973), which can be found in Yang and Shen (2009). The nozzle throat is located at $x = 0.0$ (m). The mesh used for the simulations was also an unstructured one which was generated with the frontal-Delaunay algorithm. The mesh had approximately the same size of the previous case, i.e., 25k elements. It was required around 20k iterations to reach convergence. Figure 7 shows the nozzle geometry and the mesh generated for the simulation. Details on the geometry, i.e., the (x,y) points of the nozzle, can be found in appendix G, section G.2. The stagnation pressure and temperature were set to 0.25 bar and 354.60 K, respectively, with a back pressure of $0.25P_0$. The boundary conditions for Moore B nozzle are summarized in table 2.

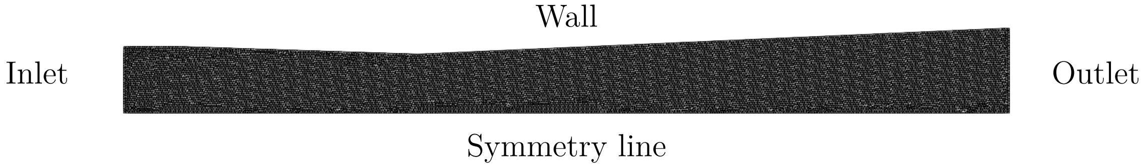

Figure 7: Moore nozzle geometry Moore et al. (1973) and mesh.

Table 2: Boundary conditions for the simulation of Moore B nozzle Moore et al. (1973).

P_0 (bar)	T_0 (K)	P_b (bar)	EoS	Mesh size	Mesh type	Nozzle throat
0.25	354.60	$0.25P_0$	PRSV	25k	Unstructured	0.00

3.2.2 Condensation of wet-steam under high-pressure conditions

This section now analyses condensing flows under high-pressure conditions and compares the results with those obtained for low-pressure conditions. For the present analysis the geometry chosen was the one by Moses & Stein Moses and Stein (1978), figure 6. An unstructured mesh of approximately 25k elements was generated using the frontal-Delaunay algorithm - the geometry and mesh used were the same on used for Moses case 2 simulation. A total of 100k iterations were needed to obtain convergence.

A stagnation pressure of 100.70 bar, a stagnation temperature of 663.08 K, and a back pressure of $0.25P_0$ were chosen - the inlet stagnation conditions used are the same as the ones used by Gyarmathy Gyarmathy (2005) on his experiment (run number 23-A), though with a different nozzle geometry. The boundary conditions used for the high-pressure simulation are summarized in table 3.

Table 3: Boundary conditions for the simulation of Moses nozzle under high-pressure conditions.

P_0 (bar)	T_0 (K)	P_b (bar)	EoS	Mesh size	Mesh type	Nozzle throat (m)
100.7	663.08	$0.25P_0$	PRSV	25k	Unstructured	0.0622

3.2.3 Variation of the position of the condensation wave with respect to the stagnation conditions

Reports from the industry that the efficiency of the supersonic separator varies considerably with respect to the inlet initial conditions. On considering this technological difficulty, a study has been proposed in which two sets of simulations were performed in order to evaluate how the position of the condensation wave may be affected by the stagnation conditions, namely the stagnation pressure and stagnation temperature. The nozzle geometry used for these simulations was the one of Moses & Stein Moses and Stein (1978) with a mesh of approximately 25 k elements.

In the first set, three simulations were performed with three different stagnation pressures 20.82 bar, 50.04 bar, and 100.70 bar. The stagnation temperature for all the simulations was the same, 615.35 K, and the back pressure was set to $0.25P_0$. The goal was to analyze how the stagnation position may affect the position of the condensation wave.

In the second set, two simulations were performed for the analysis with stagnation temperatures of $T_0 = 615.35$ K and $P_0 = 674.40$ K. The stagnation pressure was set to $P_0 = 50.04$ bar for both cases and the back pressure was set to $0.25P_0$. In this case it was analyzed the variations in the position of the condensation wave with respect to the stagnation temperature.

4 RESULTS AND DISCUSSION

This section is dedicated to discussing numerical results obtained for high-speed condensing flows under different conditions. The first section presents results obtained for condensation under low-pressure conditions for two well known nozzle geometries: Moses & SteinMoses and Stein (1978) and Moore B nozzle Moore et al. (1973). In the second section the results of a numerical simulation under high-pressure conditions are shown. The discussion of the results of these sections, i.e., 4.1 and 4.2, shall focus on metastability, entropy generation, and comparisons between the results obtained for low- and high-pressure condensation.

The last section, i.e., 4.3, present a brief analysis of the position of the condensation wave with respect to the initial conditions, namely P_0 and T_0, respectively. This discussion is important in the development of a supersonic separator since the closer to the nozzle throat condensation occurs the better it is as it allows more room for separating the condensed phase from the gas-mixture.

All simulations were performed using the SU2 branch *feature_2phase* Azzini (2018) with pure wet-steam as working fluid, it is assumed that the nozzle walls are adiabatic, and only two-dimensional Euler flows are considered in the present work.

4.1 Condensation of wet-steam under low-pressure conditions

4.1.1 Moses & Stein nozzle

For the Moses & Stein case 2 simulation, the logarithm of the maximum residual obtained was around -16.28 whereas the logarithm of the residues of ρ, ρE, the number of droplets per unit mass (μ_0), and the liquid mass fraction (y) were around -17.43, -11.58, $+1.37$, and -22.68, respectively. The residuals of the simulation are shown in table 4.

Table 4: Residuals obtained for the simulation of Moses case 2 with a mesh of approximately 25k elements.

Residuals	value
log(Max. res.)	-16.2765
$log(Res[\rho])$	-17.427608
$log(Res[\rho E])$	-11.582593
$log(Res[\mu_0])$	+1.365384
$log(Res[y])$	-22.682952

Figure 8 shows the results of the simulation, such as the vapor thermodynamics temperature 8a, the liquid mass fraction 8b, the droplet number density 8c, and the compressibility factor 8d.

The droplet number density indicates where the liquid phase begins to form. It can be seen from figure 8c that it occurs at $x \approx 0.09$ (m), where the droplet number density increases sharply from 0.0 to 10^{17} droplets per unit mass. From figure 8b it can also be seen that once the liquid phase is formed the mass fraction of liquid keeps on growing.

Note from figure 8a that the vapor temperature increases slightly near the condensation onset. This is also accompanied by an increase in static pressure, figure 9a, and a slight decrease in the Mach number. The flow regime does not change, i.e., it continues in the supersonic regime, despite the decrease in Mach number. This fact has been observed experimentally by Lettieri et al. (2017) and in numerical studies, such as Afzalifar et al. (2017); Azzini (2019).

Figure 8d shows that the compressibility factor remains close to unity throughout the whole length of the nozzle. This is somewhat expected as the pressure used in this simulation is relatively low and it is expected that for such low pressures the gas behaves as an ideal one.

Figure 9a shows a plot of the static and stagnation pressures ratio along the length of the nozzle. The plot was taken with respect to the symmetry line. It can be seen that right after $x \approx 0.09$ (m) there is an increase in the vapor static pressure. This occurs as a result of the condensation phenomena due to the fact that the liquid phase transfers thermal energy to the vapor in the form of enthalpy, i.e., $h_v - h_l$. The vapor then absorbs the thermal energy, which then this leads to an increase in the vapor thermodynamic temperature and static pressure Lettieri et al. (2017).

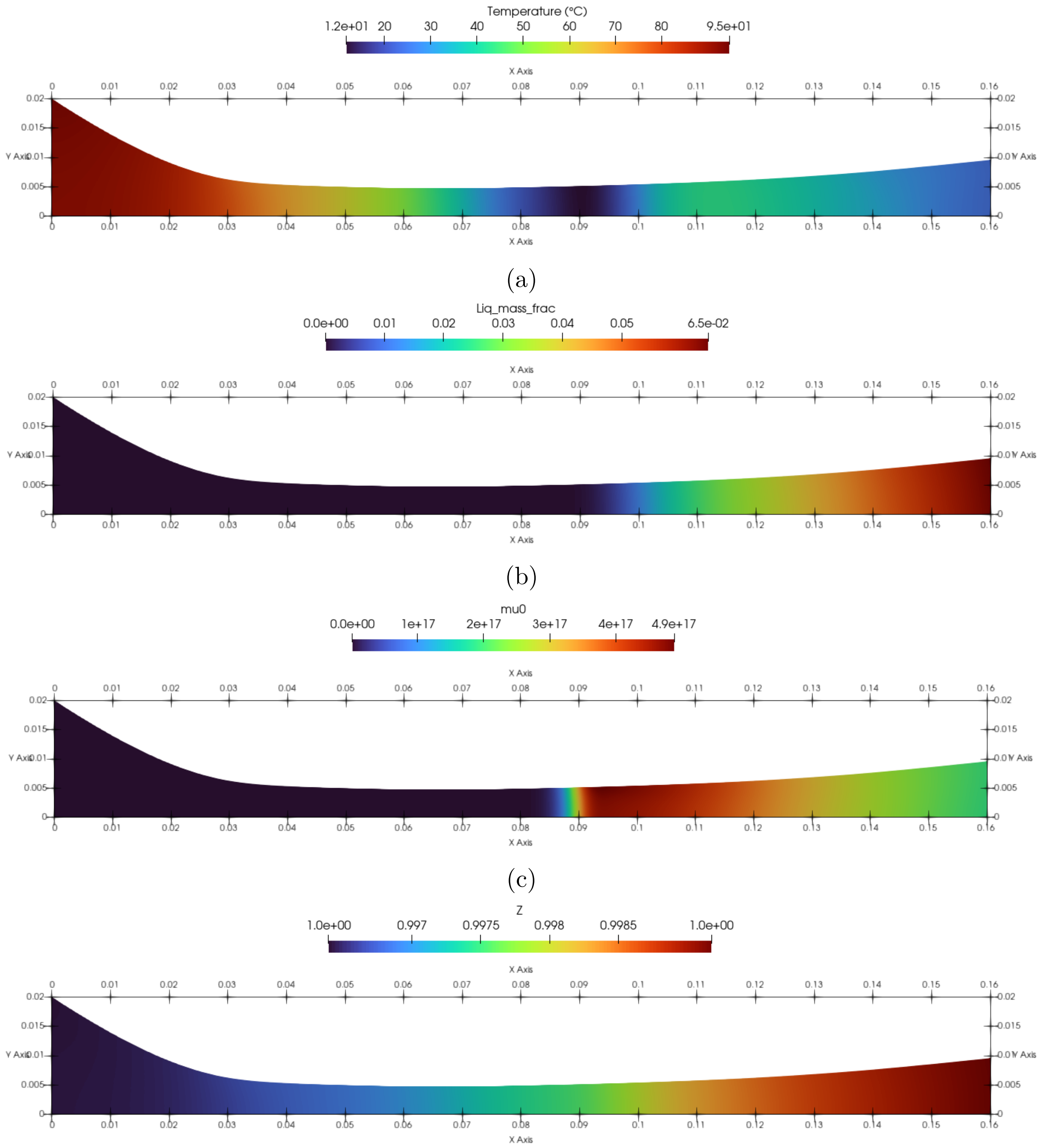

(a)

(b)

(c)

(d)

Figure 8: Vapor thermodynamic temperature 8a, liquid mass fraction 8b, droplet number density 8c, and compressibility factor 8d for Moses case 2 simulation.

The pressure ratio, as the one shown in figure 9a, is used to compare numerical results with experimental data. Such data can be found in the literature, e.g., Moses and Stein (1978); Yang and Shen (2009), and the experimental data provided is plotted along with the pressure curve obtained with numerical simulations in order to evaluate the accuracy of the models used in the simulations.

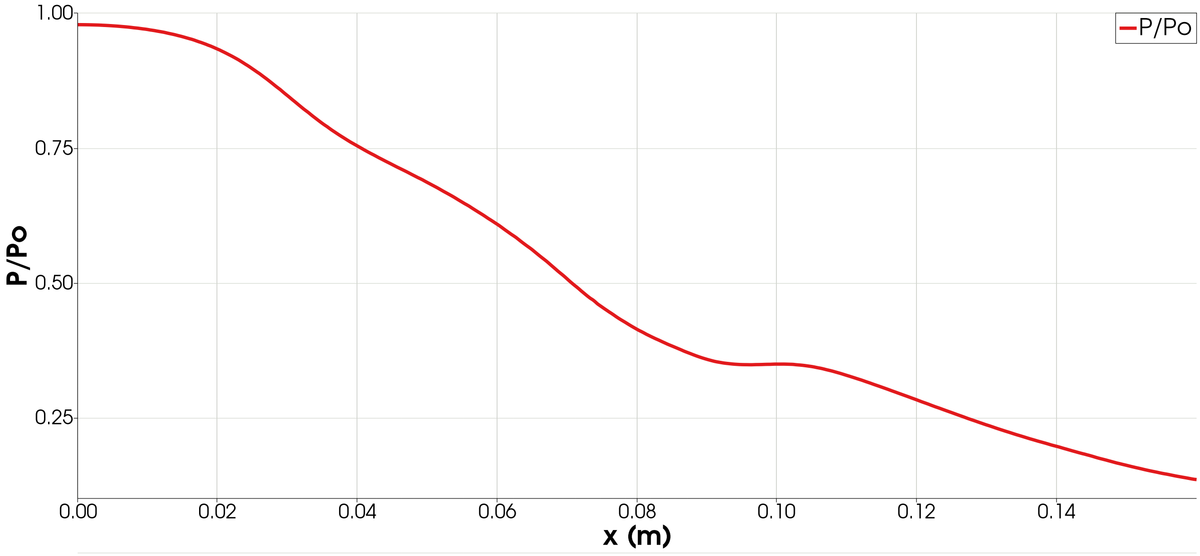

(a)

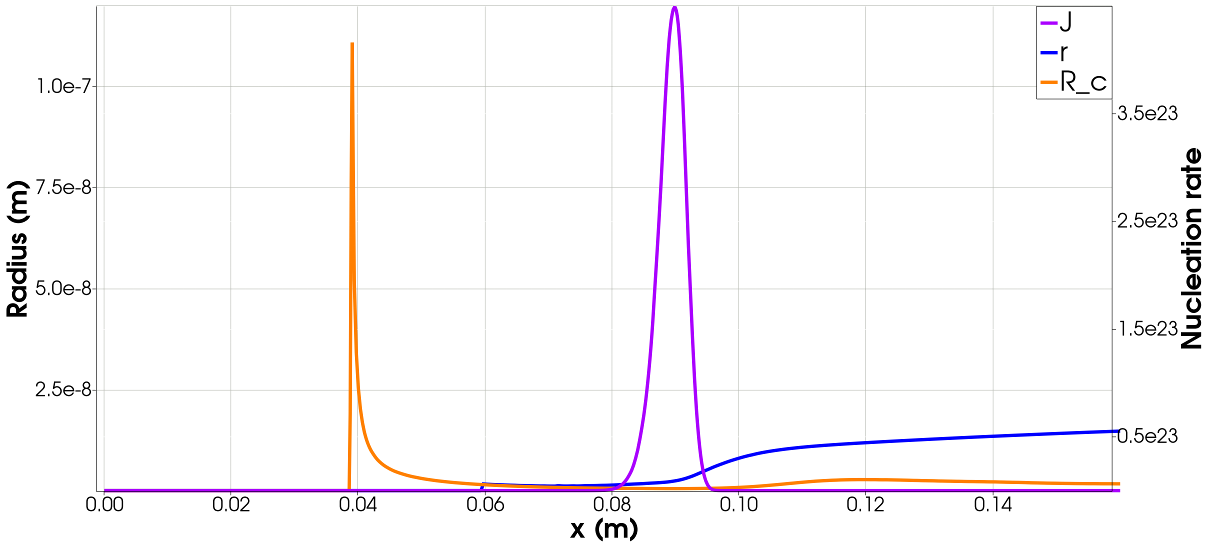

(b)

Figure 9: Ratio between the static and stagnation pressures along the length of the nozzle with respect to the symmetry line 9a and plot with respect to the symmetry line of the average droplet radius and critical radius (bottom-left axis) and nucleation rate (bottom-right axis) along the length of the nozzle 9b for Moses case 2.

Note that the pressure increase does not occur at the exact same position of the condensation onset. It is possible to say that the flow ”notices” that condensation has occurred only when a certain amount of liquid has formed - and the vapor has absorbed the corresponding amount of thermal energy transferred from the liquid phase. This is also illustrated in figure 9b in which it can be seen that the nucleation rate reaches a maximum value at $x \approx 0.09$ (m) and the increase in vapor static pressure occurs at a later position, near $x \approx 0.10$ (m).

Figure 9b shows the average droplet radius and critical radius on the bottom-left axis and the nucleation rate on the bottom-right axis. It can be seen that the average droplet radius begins to appear before the condensation onset. However this average radius is below the critical radius and therefore condensation does not occur - the liquid phase is not stable until the critical radius is reached. It is only when the average radius becomes greater than the critical radius that the droplet size begins to grow consistently.

Figure 10 shows the stagnation enthalpy of the two-phase fluid, figure 10a, which is calculated according to equation 2.18, the supersaturation rate 10b, and entropy generated in the condensation process 10c.

For the two-phase fluid analysis of adiabatic flows through a nozzle, the net heat transfer is equal to zero and the stagnation enthalpy should therefore remain constant throughout the nozzle. However, figure 10a shows that the stagnation enthalpy does vary along the nozzle which, strictly speaking, should not occur. On considering numerical errors and the fact that the thermodynamic models used have limitations, it is understandable that the values of stagnation enthalpy may fluctuate. Moreover, the variation in the stagnation enthalpy values are relatively small (a 1.47% variation) and may be neglected.

$$\frac{(6.9 - 6.8) \times 10^5}{6.8 \times 10^5} \approx 0.0147 = 1.47\%$$

It can be seen from figure 10b that at the nozzle inlet the supersaturation rate is less than unity, which means that condensation cannot occur. At $x \approx 0.05$ (m) it is around unity and keeps on increasing until it is greater than unity. Near the condensation onset at $x \approx 0.09$ (m) the supersaturation rate reaches a maximum value of 10 and then decreases.

Note that although phase change occurs, the values of supersaturation decrease but remain greater than unity. This indicates that the flow remains metastable even though condensation has already taken place.

Figure 10c shows the entropy generated in the flow. It can be seen that between $0.00 \leq x \leq 0.09$ (m) there is no generation of entropy. It is near $x \approx 0.09$ (m), which coincides with the position of the condensation wave, that the generation of entropy begins. The irreversibilities arise from the fact that the vapor and liquid phases exchange thermal energy while being at different temperatures.

After condensation occurs, the generation of entropy drops from $89kJ/K$ to approximately $20kJ/K$ but does not reach zero, which means that entropy is still being generated. This situation may be explained by analyzing figures 10b and 10c. Figure 10b indicates

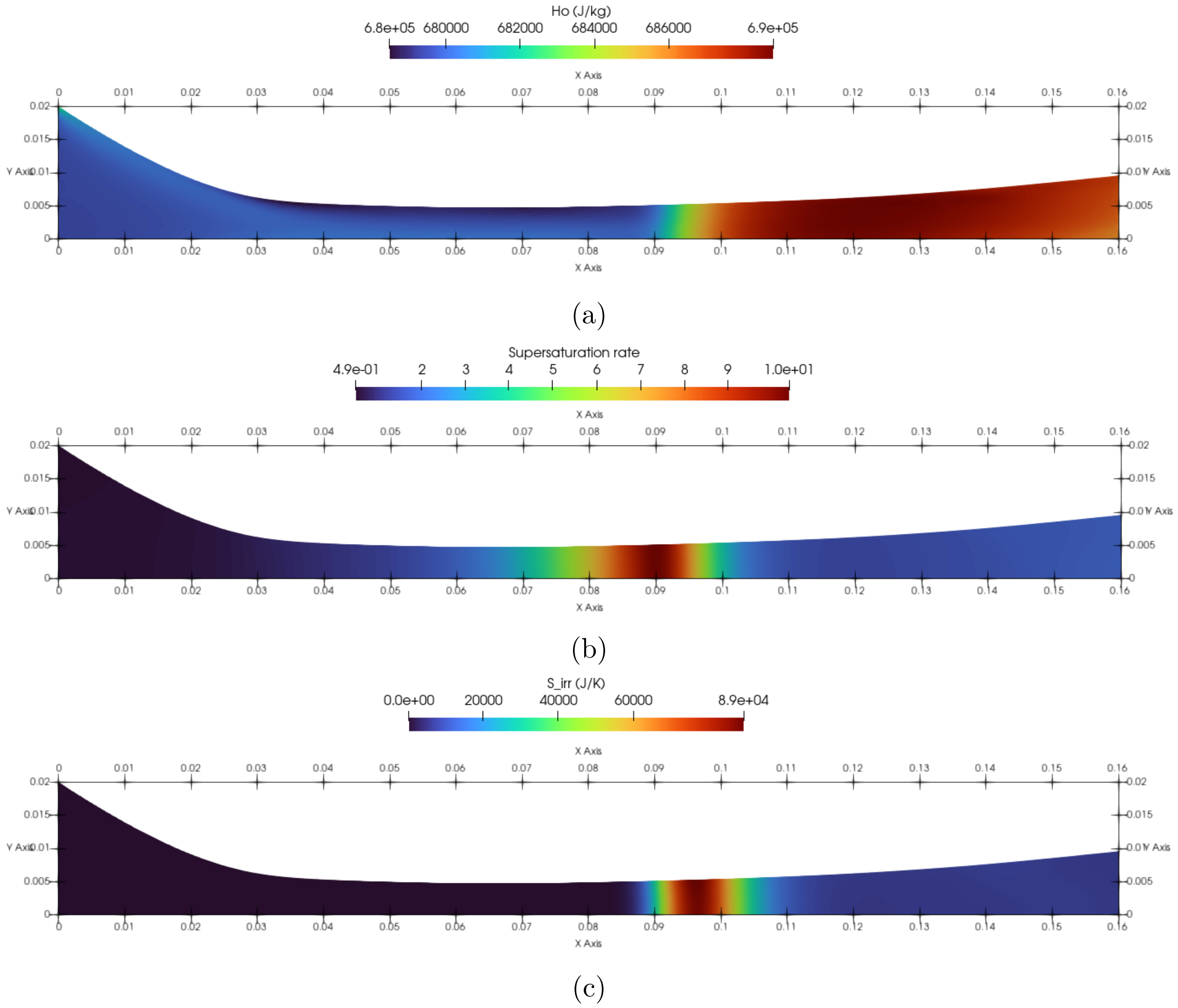

(a)

(b)

(c)

Figure 10: Two-phase fluid stagnation enthalpy of the two-phase fluid along the nozzle 10a, supersaturation rate along the nozzle 10b, and entropy generated in metastable condensation 10c for Moses case 2 simulation.

that flow is still metastable after condensation has occurred and this may be related to the entropy generation not reaching zero after condensation - the vapor and liquid continue to exchange thermal energy with each phase being at a different temperature, which means that the mechanism of generation of irreversibilities is still being triggered.

4.1.2 Moore B nozzle

For Moore B nozzle, the logarithm of the maximum residual for this case was around -15.68 and the logarithm of the residues of ρ, ρE, μ_0, and y were around -16.33, -10.61, $+1.39$, and -21.28, respectively. The residuals of the simulation are shown in table 5. Overall, Moses case 2 has produced lower residuals than Moore B case - both cases were simulated with meshes of approximately the same size.

Table 5: Residuals obtained for the simulation of Moore B nozzle with approximately 25k elements.

Residuals	value
$log(\text{Max. res.})$	-15.6816
$log(Res[\rho])$	-16.326081
$log(Res[\rho E])$	-10.611358
$log(Res[\mu_0])$	+1.387763
$log(Res[y])$	-21.277684

Figure 11 show the vapor thermodynamics temperature 11a, liquid mass fraction 11b, number density 11c, and compressibility factor 11d. For the Moore B nozzle, condensation occurs at $x \approx 0.05$ (m), where the moment of order zero increases and reaches values of order 10^{16} droplets per unit mass. Again, the liquid mass fraction keeps on increasing once condensation occurs.

It is interesting to note that Moses case 2 resulted in less droplets per unit mass (10^{16} vs 10^{17}) and less liquid mass fraction (0.045 vs 0.065) than Moses case 2. Overall, the flow seems to follow the same pattern as the previous case, i.e., the vapor thermodynamic temperature increases as the result of thermal energy exchange between with the liquid phase and the compressibility factor remains close to unity throughout the nozzle.

Figure 12a shows the plot with respect to the symmetry line of the ratio between static and stagnation pressures along the length of the nozzle. It can be seen that the vapor static pressure increases right after the condensation onset, just like in the previous case. Figure 12b shows the average droplet radius along with the critical radius (bottom-left axis) and the nucleation rate (bottom-right axis) along the length of the nozzle. It appears that the average droplet radius becomes greater than the critical size before the nozzle throat. This behavior is somewhat unexpected and may be related to the accuracy of critical radius expression (2.4) which leads to the critical radius being less than the average droplet radius in the converging part of the nozzle. On the other hand, this may be due to numerical errors or maybe the mesh quality near in the vicinity if the nozzle throat. It has also been found that in the SU2 branch the formation of the liquid phase is triggered when the vapor temperature reaches the saturation temperature. According to the literature this is not correct due to the fact that metastable condensation is triggered when the Wilson temperature is reached and this inconsistency may be the reason why the average droplet radius becomes greater than the critical radius at the converging section of the nozzle.

So far, both simulations seem quite similar. By analyzing figure 13, however, it is possible to notice a few important differences between the simulations. Figure 13a shows the two-phase stagnation enthalpy along the nozzle, figure 13b shows the supersaturation rate along the nozzle, and figure 13c shows the generation of entropy in the nozzle.

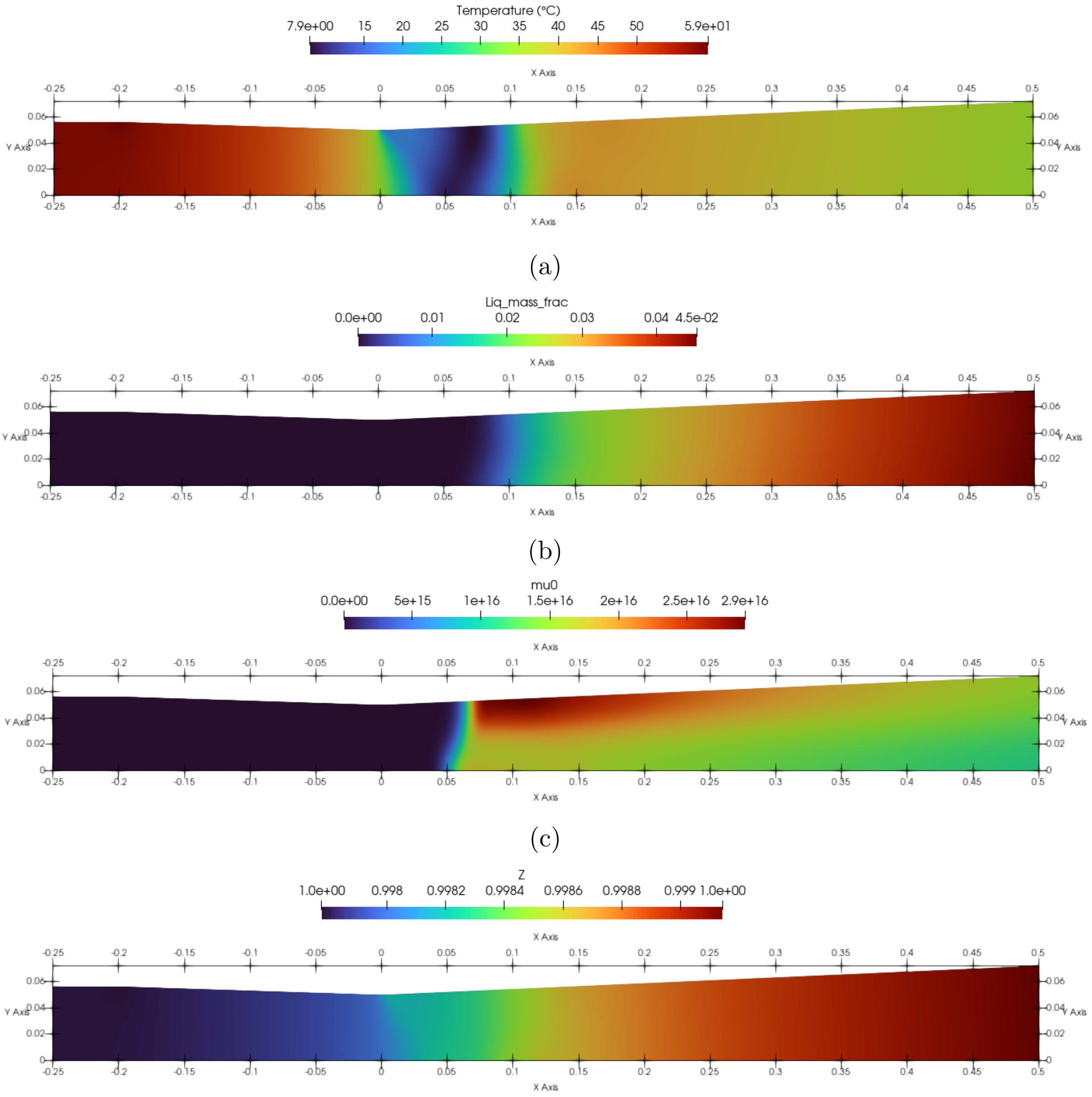

(a)

(b)

(c)

(d)

Figure 11: Vapor thermodynamic temperature in Celsius degree 11a, liquid mass fraction 11b, droplet number density 11c, and compressibility factor 11d obtained for Moore B simulation.

The stagnation enthalpy behaves similarly to Moses case 2 and remains approximately constant, with a variation of approximately 1.52%. The supersaturation rate is equal to unity at the nozzle inlet, begins to increase near the nozzle throat up until a maximum value of 9.0, and then begins decreasing at $x \approx 0.1$ (m). In this case, however, the supersaturation rate approaches unity as the flow moves downstream towards the nozzle outlet, figure 13b.

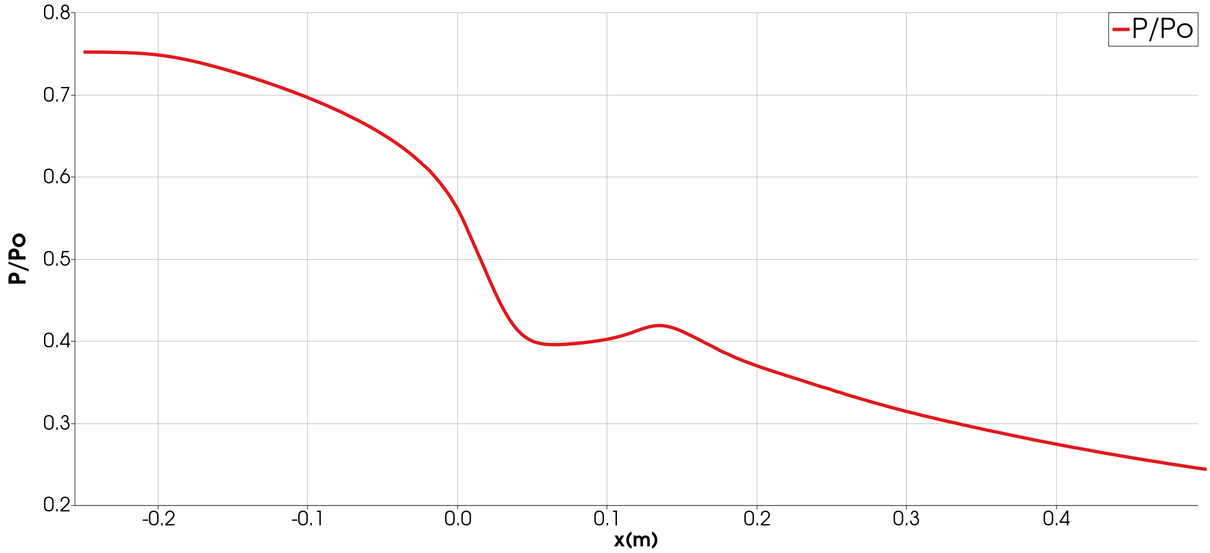

(a)

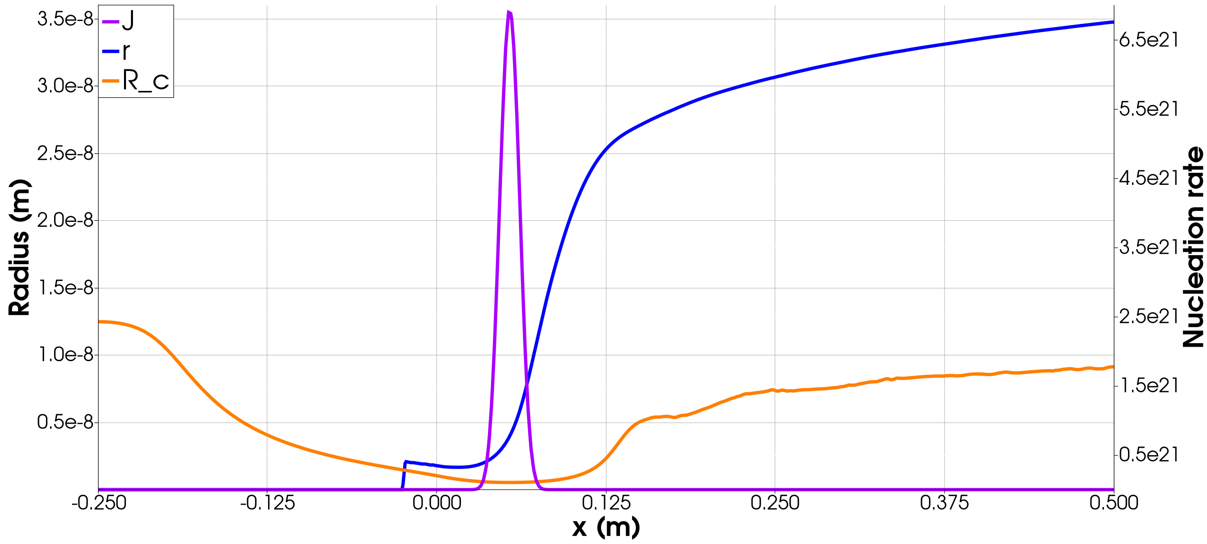

(b)

Figure 12: Ratio between the static and stagnation pressures along the length of the nozzle with respect to the symmetry line 12a and average droplet radius and the number density along the length of the nozzle 12b for Moore B nozzle.

As for the entropy generation, it grows from 0 kJ/K to 12 kJ/K in the condensation onset. So far, the behavior is the same as the previous case of Moses. However, as the flow moves downstream towards the nozzle outlet and away from the condensation onset, the entropy generation drops to approximately zero, figure 13c, unlike case 2 of Moses.

By analyzing figures 13b and 13c, it would seem that the entropy generation drops to zero when the supersaturation rate approaches unity.

The results of Moses case 2 and Moore B nozzle suggest a relationship between metastable condensation and entropy generation. For case 2 of Moses, the supersaturation rate does not reach unity after condensation occurs. In parallel to that, the entropy generation does not drop to zero. The fact that the supersaturation rate is not equal to unity indicates that the flow is metastable and thus metastable condensation may still occur, which may be the reason why figure 10c indicates that there is still entropy being generated after the condensation onset.

The simulation of Moore B nozzle seems to be in agreement with the results of Moses case 2. For Moore B nozzle the supersaturation rate approaches unity after condensation occurs and in parallel with that the entropy generation approaches zero. A supersaturation rate equal to unity means that should condensation occur the vapor and liquid phases will exchange thermal energy while both phases are at the same temperature. Phase change under such conditions, i.e., the flow is no longer metastable, does not appear to generate entropy, as indicated by figure 13c and from equation (2.23).

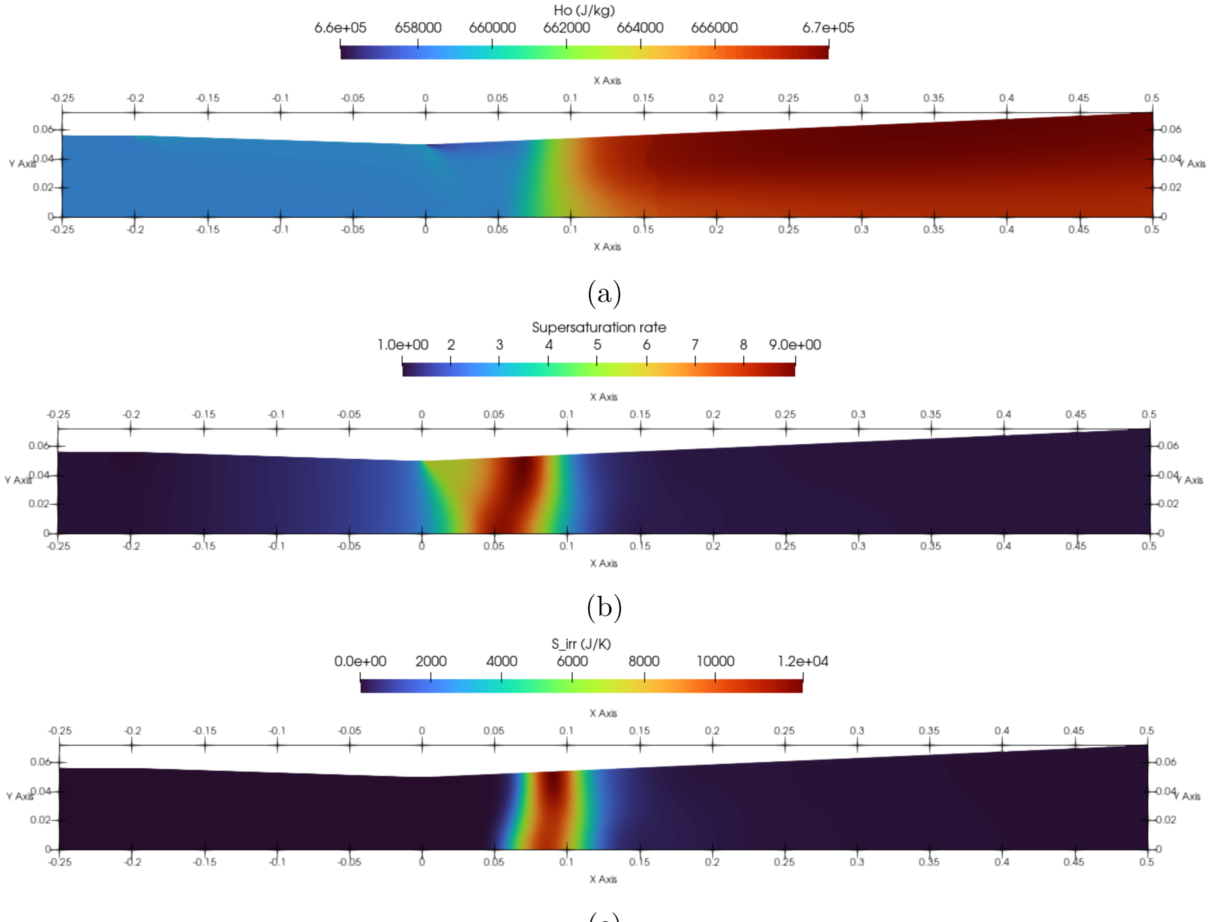

(a)

(b)

(c)

Figure 13: Two-phase fluid stagnation enthalpy along the nozzle 13a, supersaturation rate along the nozzle 13b, and entropy generated in metastable condensation 13c for Moore B simulation.

As for the error in the evaluation of the stagnation enthalpy, it is evaluate to be around 1.52%.

$$\frac{(6.7-6.6)\times 10^5}{6.6\times 10^5}\approx 0.0152 = 1.52\%$$

On comparing the two low-pressure simulations it can be seen that both flows display the same behavior, such as the increase in static pressure and a slight reduction in Mach number after the condensation onset. On the other hand, it has been found that the total number of droplets per unit mass and the liquid mass fraction formed were greater in the nozzle geometry of Moses than in the geometry of Moore. Additionally, the entropy generated for Moses case 2 was also greater than the entropy generated for Moore B.

4.2 Condensation of wet-steam under high-pressure conditions

For the simulation of condensation under high-pressure, the logarithm of the maximum residual was around -14.01 and the logarithm of the residuals of ρ, ρE, μ_0, y, were around -14.88, -8.81, $+1.02$, and -19.23, respectively. The residuals obtained for high-pressure condensing flows are summarized in table 6. Note that these residuals are greater than the ones obtained for condensation under low-pressure conditions which indicate greater error in the solutions.

Table 6: Residuals obtained for the simulation with Moses nozzle with approximately 25k elements under high-pressure conditions.

Residuals	value
$log(\text{Max. res.})$	-14.0101
$log(Res[\rho])$	-14.883092
$log(Res[\rho E])$	-8.802501
$log(Res[\mu_0])$	+1.023228
$log(Res[y])$	-19.227101

Some of the flow properties are shown in figure 14, such as the vapor thermodynamic temperature 14a, the liquid mass fraction 14b, and the compressibility factor 14d. It is worth noting a few differences between the Moses case 2 (low-pressure condition) and the present simulation which deals with a high-pressure condition. The first one is the position of the condensation wave. In figure 8c the number density begins increasing around $x \approx 0.09$ (m) whereas in figure 14c the same quantity begins growing at an earlier position, at $x \approx 0.085$ (m). It would seem that for higher pressure the position of the condensation wave moves upstream closer to the nozzle throat. A more detailed analysis of the effect of the stagnation pressure effect on the position of the condensation wave will be discussed in the next section.

Secondly, figure 14c indicates a lower number of droplets per unit mass than the low pressure case (10^{15} for high pressure condition versus 10^{17} for low pressure conditions). On the other hand, the maximum liquid mass fraction is greater than the one obtained for the low pressure case (0.15 for the high pressure case versus 0.065 for the low pressure case). A possible explanation for this may be related to the droplet size. Low pressure condensation may lead to more droplet per unit mass than the high pressure case, but the size of the droplets formed in low-pressure condensation may be smaller than those formed under high-pressure conditions, which could explain the fact that high-pressure condensation leads to a greater liquid mass fraction. Figure 15b shows that condensation under high-pressure conditions does generate bigger droplets. For the present case, the average droplet radius is of the order of 10^{-7} whereas for Moses case 2 it was of order 10^{-8}.

Additionally, the compressibility factor for condensation under high-pressure varies between 0.83 and 0.93, according to figure 14d. This contrasts with the compressibility factors obtained for both cases of condensation under low-pressure conditions, which were quite close to unity throughout the nozzle. This behavior was expected and shows that the code is producing results that are physically consistent. Note that for simulations under high-pressure conditions the vapor phase behavior may differ considerably from the ideal behavior and it is thus important to take non-ideal gas behavior into account when dealing with condensation under these conditions.

Figure 15a shows a plot taken with respect to the symmetry line of the ratio between the vapor static and stagnation pressures along the length of the nozzle. It can be seen the increase in the vapor static pressure due to the occurrence of condensation. Figure 15b shows the average droplet radius along with the critical droplet radius (bottom-left-axis) and the nucleation rate (bottom-right axis). Here the average droplet radius becomes greater than the critical radius only after the nozzle throat.

This contrasts with the previous cases. For Moses case 2, the values of average droplet radius was quite close to the values of critical radius near the nozzle throat and for Moore B the average droplet radius became greater than the critical radius before the nozzle throat. These results for high-pressure seem to be more consistent with the literature than the low-pressure results. Numerical errors and mesh quality may be to blame for this seemingly erroneous behavior, but this could also be due to the fact that the critical radius expression given by equation (2.4) is suitable for high-pressure cases but not so accurate for low-pressure cases. It is possible that for low-pressure cases equation (2.2) is more suitable for evaluating the critical radius.

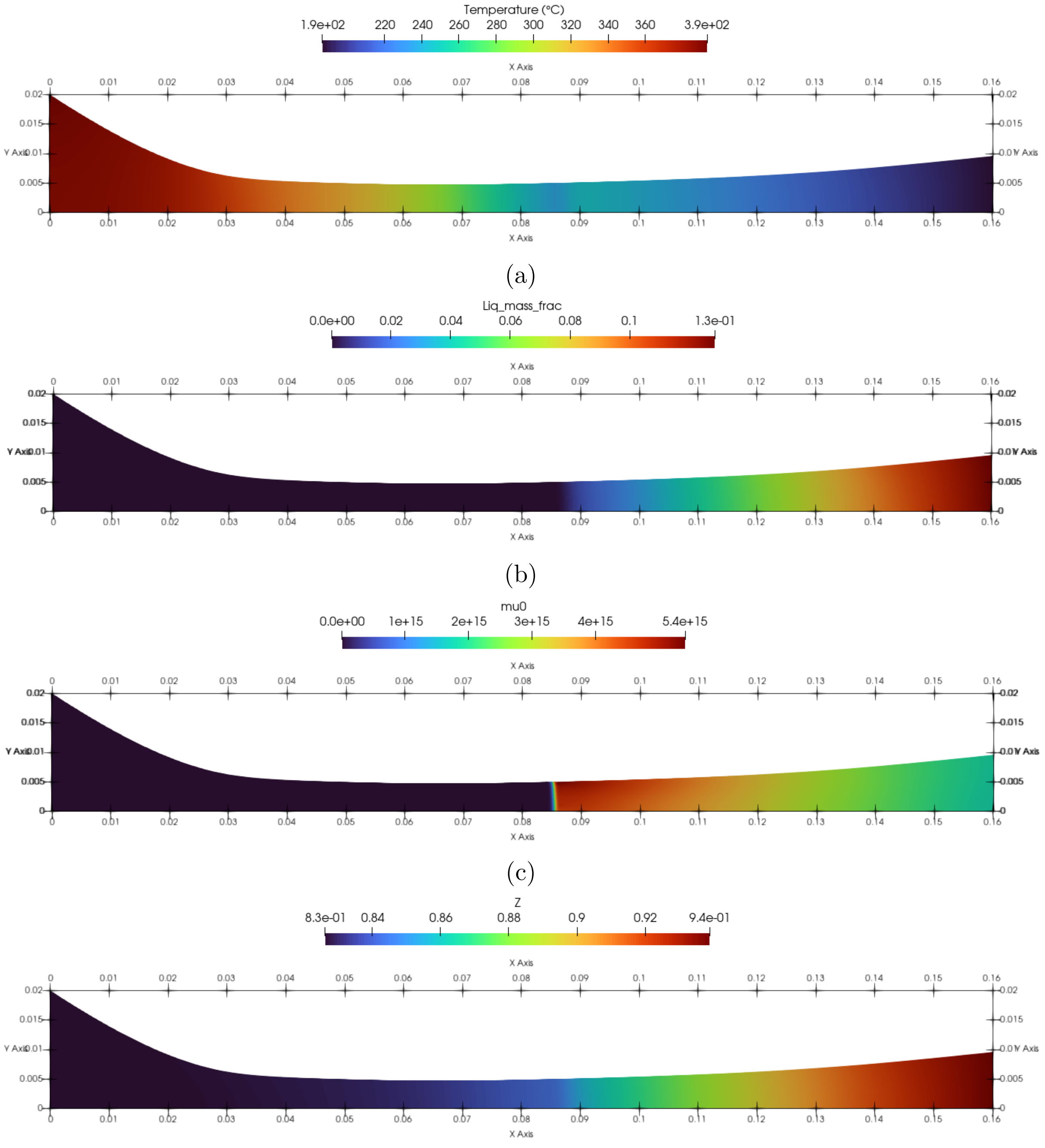

(a)

(b)

(c)

(d)

Figure 14: Vapor thermodynamic temperature in Celsius degree 14a, liquid mass fraction 14b, droplet number density 14c, and compressibility factor 14d obtained for the simulation of Moses nozzle geometry under high-pressure conditions.

On analyzing figure 16, it can be seen that the variation of the stagnation enthalpy, figure (16a), is greater than the low-pressure cases. For this case the variation is a 10% one, which is almost 10 times greater than the one obtained for the low-pressure case. This may be related to the fact that the residuals obtained for high-pressure simulations were greater than the ones obtained for the low-pressure simulations.

$$\frac{(1.1 - 1.0) \times 10^6}{1.0 \times 10^6} = 0.1 = 10\%$$

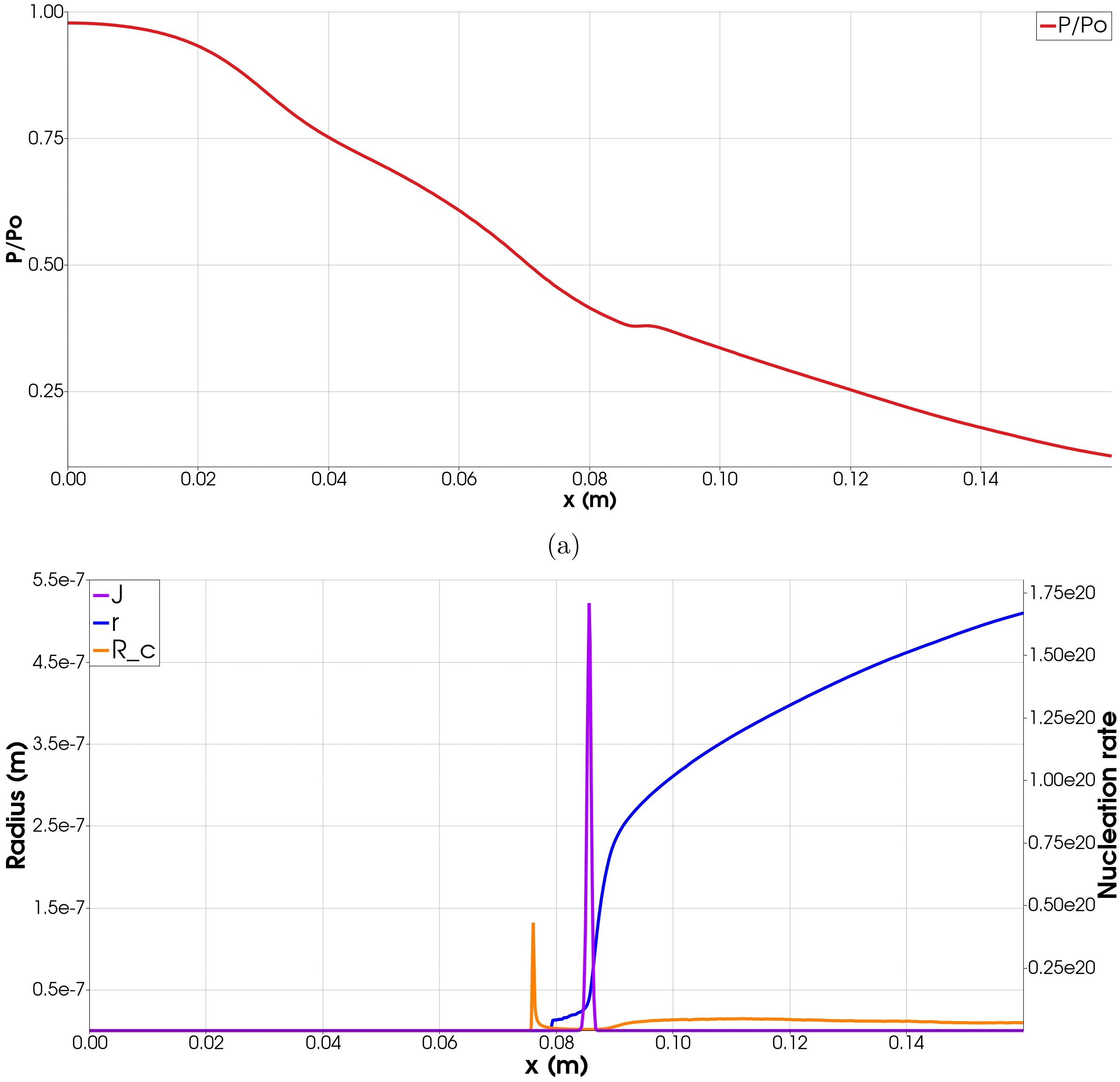

(a)

(b)

Figure 15: Ratio between the static and stagnation pressures along the length of the nozzle with respect to the symmetry line for Moses nozzle geometry (15a) and average droplet radius and the number density along the length of the nozzle (15b) for condensation under high-pressure condition.

The supersaturation rate values obtained for the high-pressure case are considerably lower than the ones obtained for low-pressure cases. Here condensation is triggered when the flow reaches a maximum supersaturation value of 1.3, whereas in the previous cases it was around 10. Once condensation occurs the values of supersaturation rate drop and approach unity, see figure 17.

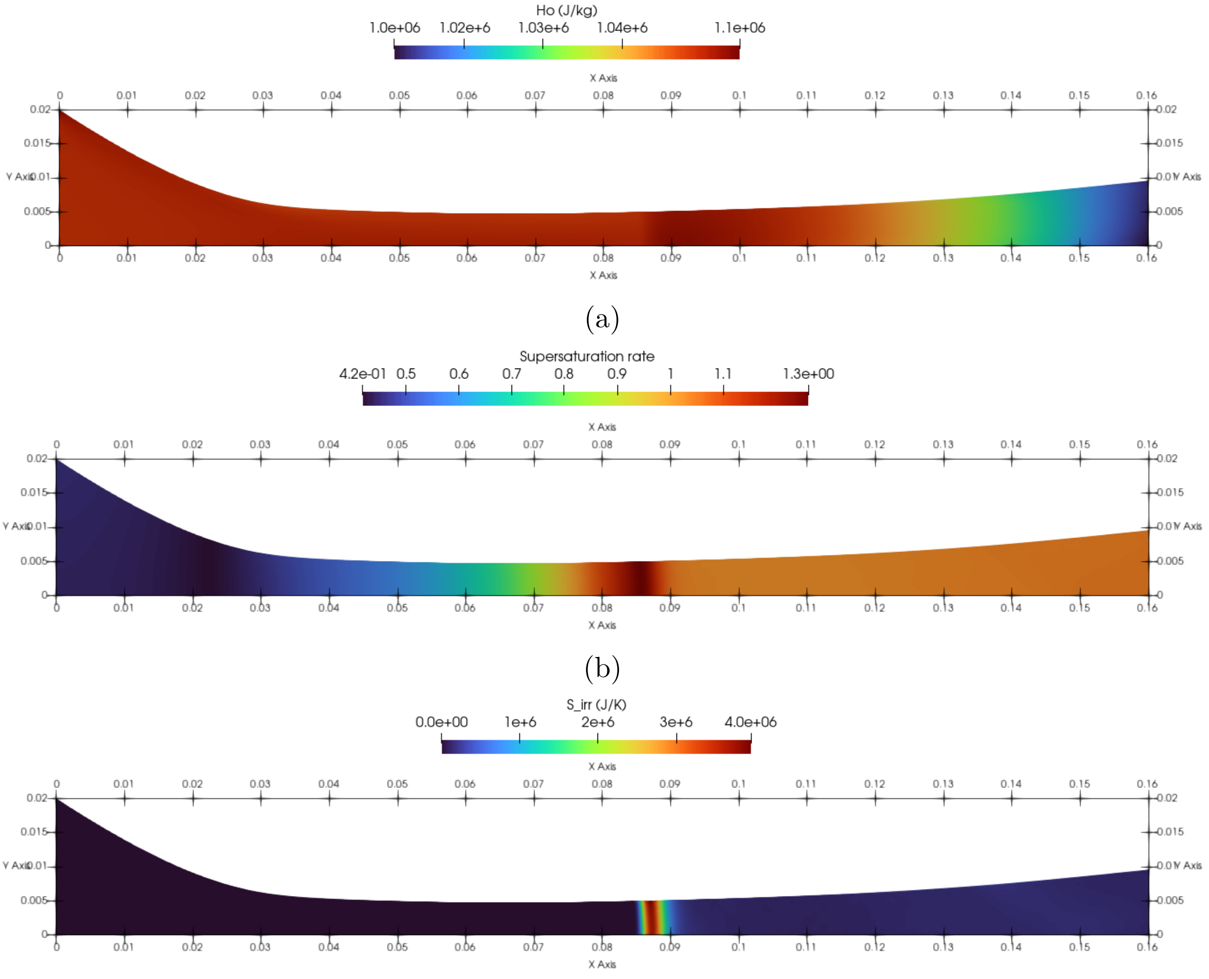

(a)

(b)

(c)

Figure 16: Two-phase fluid stagnation enthalpy along the nozzle 16a, supersaturation rate 16b, and entropy generated in metastable condensation 16c obtained for simulation of Moses nozzle geometry under high-pressure conditions.

The generation of entropy reaches a maximum value of approximately 4000 kJ/K, which is considerably greater than the entropy generated for the low -pressure cases - around two orders of magnitude. Additionally, once condensation has occurred the entropy generation drops to nearly zero. It is possible that there is still entropy being generated owing to the fact that the flow is still metastable after the condensation wave - the supersaturation rate is close to but slightly greater than unity. This is agreement with the previous results and it seems that entropy is generated in the condensation process and it may continue to generate irreversibilities even after condensation has occurred if the flow remains metastable after the condensation onset.

Figure 17 shows a plot with respect to the symmetry line of the nozzle of the supersaturation rate (left-bottom axis) and the droplet number density (right-bottom axis) along the length of the nozzle. It is worth noting that the droplet number density only grows inside the metastable region and there is a sharp increase in it from 0 to nearly 4.5×10^{15} droplets per unit mass when the flow reaches a maximum value of supersaturation rate.

Note that once the condensation wave occurs both the supersaturation rate and the droplet number density decrease. The supersaturation rate does not reach unity and the droplet number density does not reach zero, which means that liquid droplets are still being formed but at a lower rate.

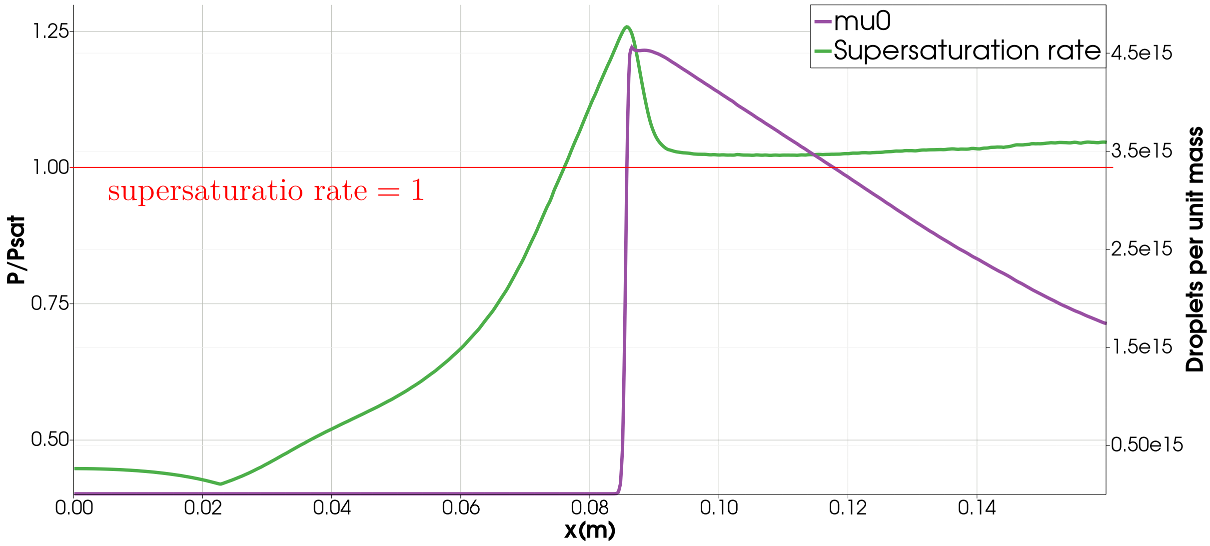

Figure 17: Plot of the supersaturation rate (left-bottom axis) and moment of order zero (right-bottom axis) along the length of the nozzle. The green line represents the supersaturation rate, the purple line represents the moment os order zero, and the red line represents supersaturation rate equal to unity. The plot was taken with respect to the symmetry line.

On comparing the case of condensation under high-pressure case with the cases of condensation under low-pressure cases, it can be seen that the greater the liquid mass fraction, the greater the entropy generation.

4.3 Variation of the position of the condensation wave with respect to the stagnation conditions

This section is dedicated to analyzing how the position of the condensation wave varies with respect to the inlet stagnation conditions. Firstly, it shall be discussed how the inlet stagnation pressure affects the position of the condensation wave while keeping the stagnation temperature at a constant value. Then, an analysis of the effect of the stagnation temperature in the position of the condensation wave while keeping the stagnation pressure constant will be made.

4.3.1 Stagnation pressure analysis

The residuals obtained for these simulations were similar to each other except for the simulation performed for 100.70 bar, whose residuals were slightly greater than the other simulations. The Residuals, as well as the number of iterations needed in order to obtain convergence, are shown in table 7.

Table 7: Residuals obtained for the simulations in which the stagnation temperature was held constant at $T_0 = 615.35$K whereas the stagnation pressure was allowed to vary.

P_0 (bar)	n	log(Max. res.)	$log(Res[\rho])$	$log(Res[\rho E])$	$log(Res[\mu_0])$	$log(Res[y])$
20.82	20k	-14.5929	-15.648671	-9.516761	+2.048064	-20.987144
50.04	22k	-14.2470	-15.211146	-9.127755	+1.050285	-19.913425
100.70	50k	-13.8901	-14.795685	-8.771749	+0.608876	-18.838681

Figure 18 shows the ratio between static and stagnation pressure along the length of the nozzle taken with respect to the symmetry line for the three cases. It can be seen that as the stagnation pressure increases the position of the condensation wave moves upwards closer to the nozzle throat. For $P_0 = 20.82$ bar, the condensation wave occurs near the nozzle outlet at $x \approx 0.15$ (m), for $P_0 = 50.04$ bar it occurs at $x \approx 0.10$ (m), and for $P_0 = 100.70$ bar it occurs right after the nozzle throat around $x \approx 0.065$ (m).

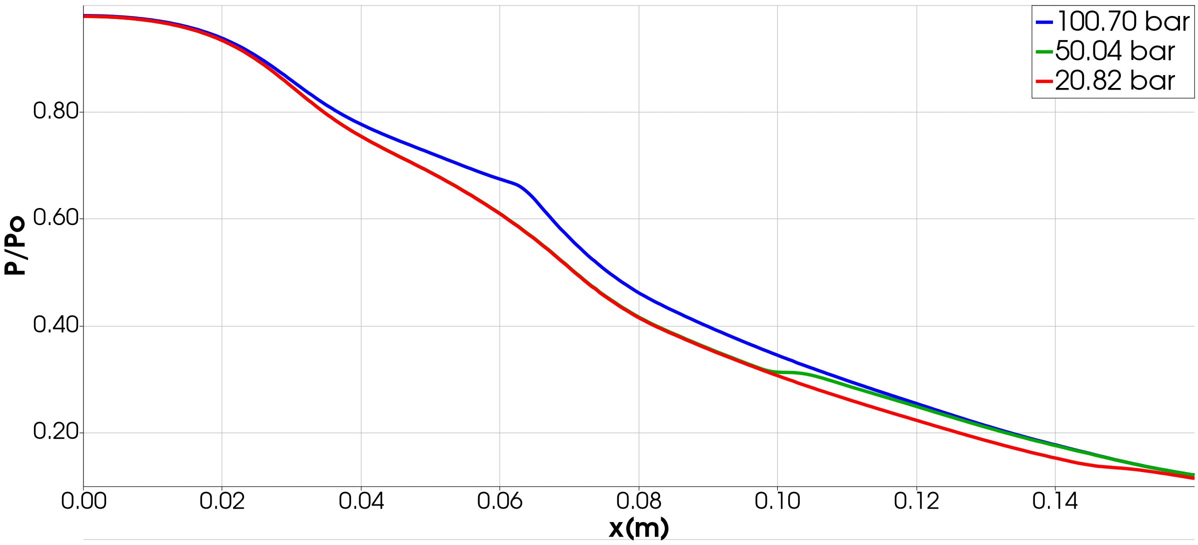

Figure 18: Comparison between the plots of P/P_0 for $P_0 = 100.70$ bar (blue line), $P_0 = 50.04$ bar (green line), and $P_0 = 20.82$ bar (red line). The plots were taken with respect to the symmetry line of the nozzle.

Figure 19a shows the moment of order zero for $P_0 = 20.82$ bar, $P_0 = 50.04$ bar, and $P_0 = 100.70$ bar. This figure helps illustrate the fact that the greater the stagnation pressure, the closer to the nozzle throat condensation occurs. Additionally, it is interesting to note that for greater stagnation pressures the number of droplets per unit mass decreases - 10^{17} droplets per unit mass for $P_0 = 20.82$ bar, 10^{16} droplets per unit mass for $P_0 = 50.04$ bar, and 10^{15} droplets per unit mass for $P_0 = 100.70$ bar. So, the results indicate that by increasing the inlet stagnation pressure the position of the condensation wave moves upstream and occurs closer to the nozzle throat and the number of droplets per unit mass decreases.

Figure 19b shows a plot of the moment of order one, i.e., the droplet average radius, along the length of the nozzle, taken with respect to the symmetry line, for the various stagnation pressures. It can be seen that greater values of stagnation pressure led to greater average droplet radius which may be related to the growth rate since once the liquid phase is formed it tends to grow. So if the condensation wave occurs at an earlier position, then droplets would reside longer inside the nozzle and would tend to keep on growing as they move downstream towards the nozzle outlet.

In a real situation this could be related to coagulation mechanism. However, the present models do not take this phenomena into account, so the greater droplet size can only be attributed to the droplet growth mechanism.

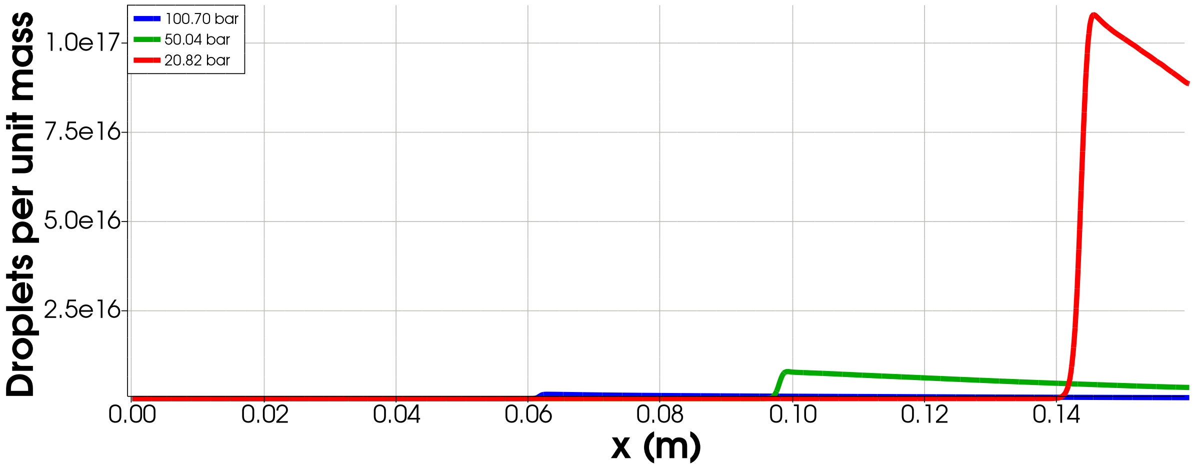

(a)

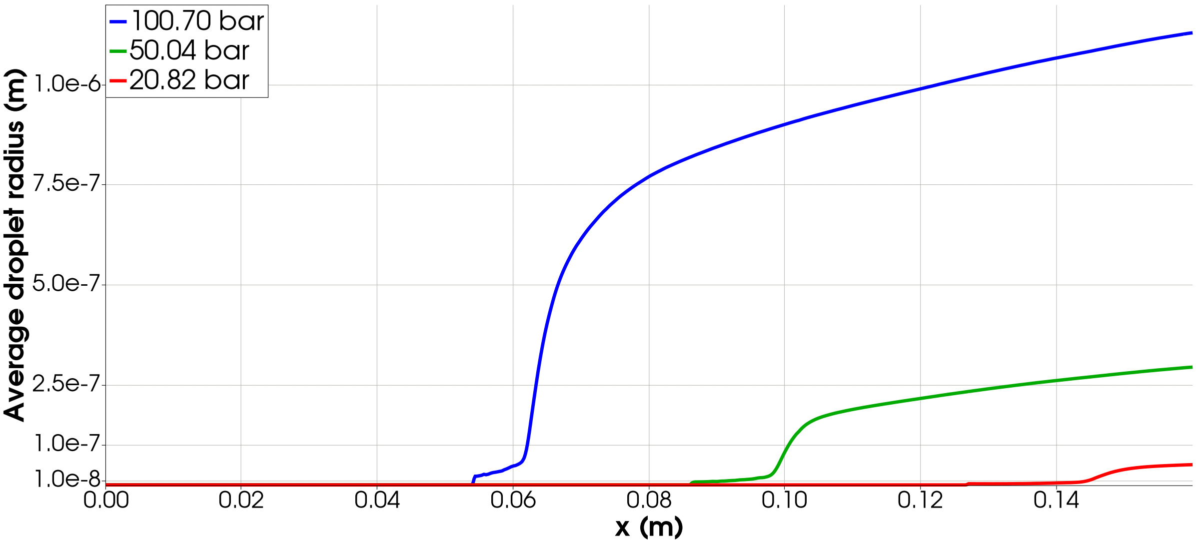

(b)

Figure 19: Moment of order zero obtained for a stagnation pressure of 20.82 bar, 50.04 bar, 100.70 bar 19a and the average droplet radius obtained for each of these simulations along the length of the nozzle 19b where the blue line represents $P_0 = 100.70$ bar simulation, the green line represents $P_0 = 50.04$ bar, and the red line represents $P_0 = 20.82$ bar. All plots were taken with respect to the symmetry line of the nozzle.

4.3.2 Stagnation temperature analysis

The residuals obtained for the simulation $T_0 = 674.40$ K were greater than those obtained for $T_0 = 615.35$ K - the maximum residual for the $T_0 = 674.40$ K simulation was around two orders of magnitude greater than the one for the $T_0 = 615.35$ K simulation. The residuals obtained and the number of iterations need to obtain convergence (n) are shown in table 8.

Table 8: Residuals obtained for the simulations in which the stagnation pressure was held constant at $P_0 = 50.04$ bar whereas the stagnation temperature was allowed to vary.

T_0 (K)	n	log(Max. res.)	$log(Res[\rho])$	$log(Res[\rho E])$	$log(Res[\mu_0])$	$log(Res[y])$
615.35	25k	-14.1912	-15.201081	-9.118497	+1.009131	-19.911102
674.40	25k	-11.7186	-14.069809	-8.036969	+1.875879	-20.284549

The results are a bit intuitive as shown in figure 20. It can be seen that by increasing the stagnation temperature the condensation wave moves downstream towards the nozzle outlet and away from the nozzle throat. This may be due to the fact that by increasing the stagnation temperature one also increases the difference between the vapor temperature and the vapor boiling temperature and, as a result, the temperature drop needed to obtain the condensation also increases and the condensation wave position tends occur at a later position.

Figure 21a illustrates it more clearly that on increasing the stagnation temperature the position of the condensation wave moves downstream further away from the nozzle throat. Also, the number of droplets per unit mass is different for both cases. For $T_0 = 615.35$ K the number of droplets per unit mass is less than 10^{16} whereas for $T_0 = 674.40$ K it is greater than 4×10^{16}.

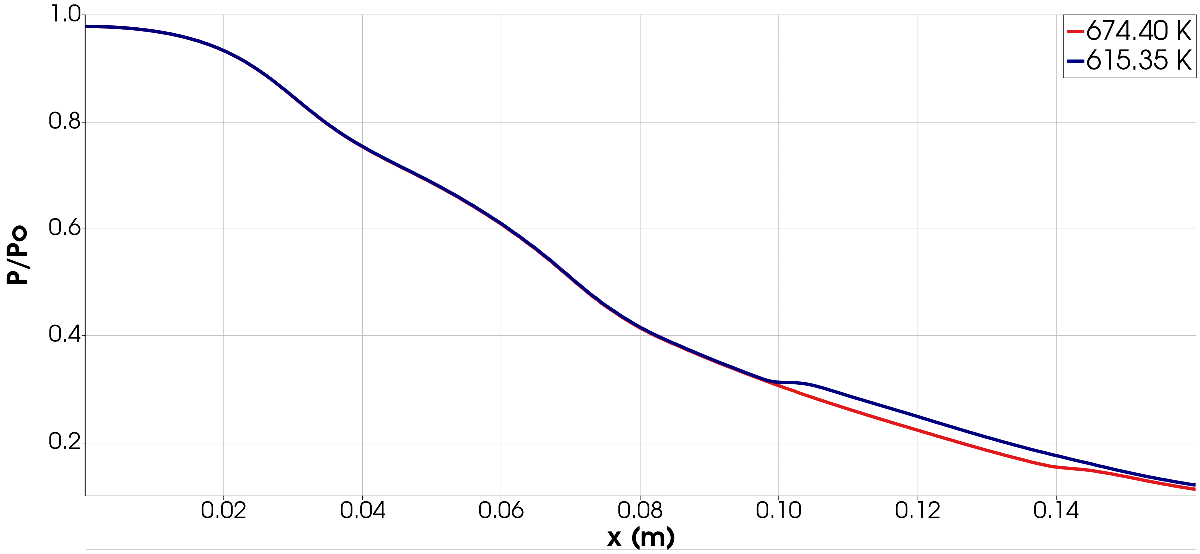

Figure 20: Comparison between the plots of P/P_0 obtained for different stagnation temperatures - $T_0 = 615.35$ bar (blue line) and $T_0 = 674.40$ bar (red line). The stagnation pressure for both cases was $P_0 = 50.04$ bar. The plots were taken with respect to the symmetry line of the nozzle.

Figure 21b shows the average droplet radius obtained for each case. For $T_0 = 615.35$

K the average droplet radius is greater than the one obtained for $T_0 = 674.40$ K. On analyzing these results with the previous ones it would seem that if condensation is triggered at an earlier position it produces bigger droplets than when condensation is triggered at a later position.

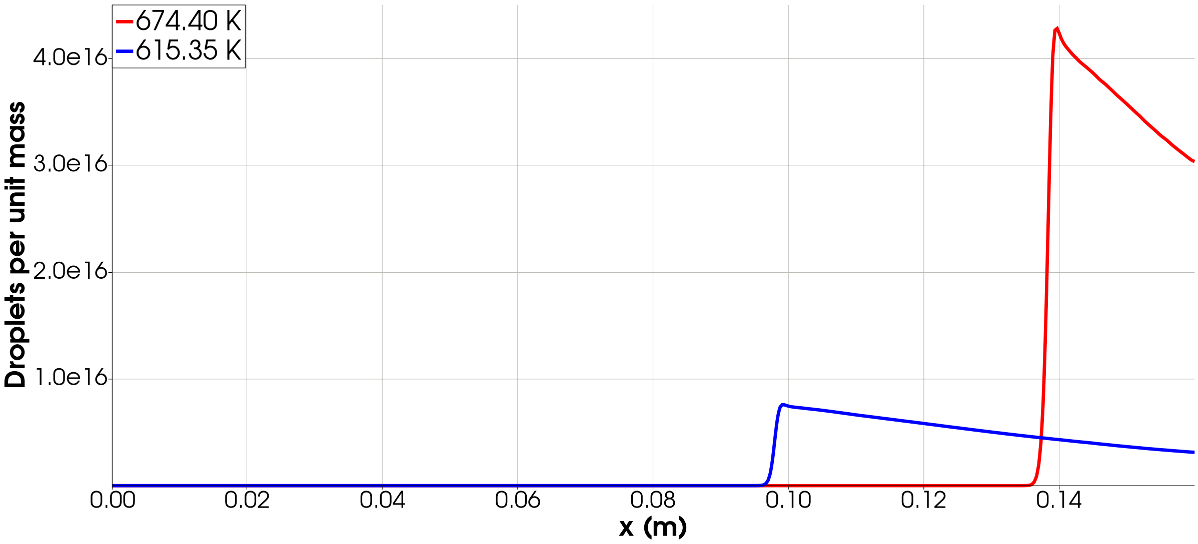

(a)

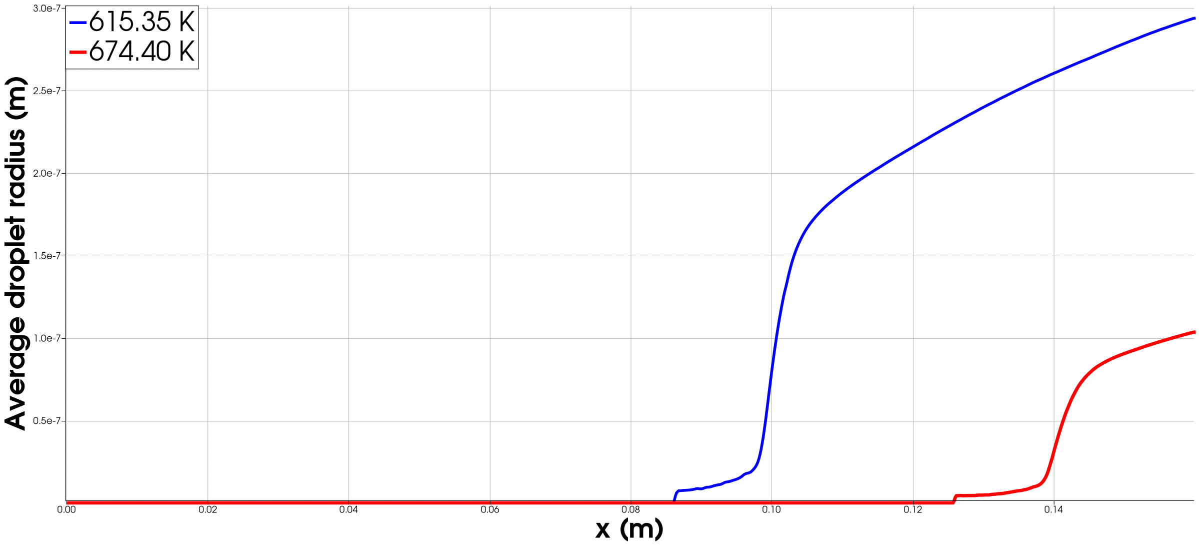

(b)

Figure 21: Moment of order zero obtained for a stagnation temperature of 615.15 K and 674.40 K 21a and the average droplet radius obtained for each of these simulations along the length of the nozzle (19b) where the blue line represents $T_0 = 674.40$ K simulation and the red line represents $T_0 = 615.15$ K. All plots were taken with respect to the symmetry line of the nozzle.

5 CONCLUSIONS

5.1 Concluding remarks

The main goal of the present work was to study and discuss the main physical aspects of high-speed condensing, i.e., metastability, the generation of entropy, differences between low- and high-pressure, and how the inlet boundary conditions may change the position of the condensation wave.

The discussions focused on the study of two-dimensional Euler flows and for such cases, the only sources of entropy generation would be shock waves and phase change phenomena. Flows with shock waves were not considered as shocks could result in (partial or total) re-evaporation of the vapor phase and re-evaporation models have not been implemented on the SU2 branch.

The simulations were performed for high-speed condensing nozzle flows under low- and high-pressure conditions, with condensation occurring under metastable conditions. Two well known nozzle were used for the simulations: Moses & Stein and Moore B nozzle. The meshes used were unstructured and were generated using the frontal-Delaunay algorithm. All the meshes had around 25k elements.

A few observations may be drawn based on the results obtained. Firstly, the simulations indicate that entropy is generated in the condensation process as a result of the exchange of thermal energy in the form of enthalpy difference ,i.e., $h_v - h_l$, between the vapor and liquid phases with each phase being at a different temperature.

Furthermore, it seems that entropy may still be generated after the condensation wave if the flow remains metastable, i.e., supersaturation rate greater than unity, after the condensation onset. Consequently, the entropy generation would only be zero if the supersaturation rate reaches unity after condensation. In such case, condensation may still occur but reversibly - the exchange of thermal energy between the vapor and liquid phases would occur with both phases being at the same temperature and would thus be a reversible heat exchange. Moreover, the high-pressure flow resulted in greater values of entropy than the low-pressure ones, i.e., 4×10^3 kJ/K versus 89 kJ/K for Moses case 2 and 12 kJ/K for Moore B nozzle. In addition to that, greater entropy generation was associated with greater liquid mass fraction, which indicates that the more liquid phase formed in metastable condensation the more entropy is generated in the flow.

A few questions may be raised by the results of the average droplet radius and the critical radius for the low-pressure condensation cases. For such cases the values of average droplet radius were either close or even greater the values of critical radius in the converging part of the nozzle (before the throat) where the flow is subsonic. Numerical errors as well as mesh quality may have been an issue. Yet, it is possible that the expression for the critical radius for a non-ideal vapor may not be so accurate for low-pressure flows - this did not occur for the high-pressure simulation. Furthermore, the SU2 branch has an inconsistency with the literature of metastable condensation, since the formation of liquid droplets is triggered with respect to the saturation line instead of the Wilson line. An investigation on the topic would be required to address the matter properly.

The inlet boundary conditions seem to affect the position of the condensation wave. Higher stagnation pressures resulted in the position of the condensation wave moving upstream towards the nozzle throat whereas higher stagnation temperatures resulted in the position of the condensation wave moving downstream away from the nozzle throat.

Additionally, the numerical results have hinted that if condensation occurs at an earlier position it tends to generate a lower number of droplets per unit mass and greater average droplet radius. Also, for higher stagnation pressures the liquid mass fraction obtained was also greater than the one obtained for lower pressures.

Among the results here presented the link between metastable condensation and entropy generation, the possibility that the greater the liquid mass fraction that condenses due to metastable condensation the greater the values of entropy generation, and how the stagnation conditions affect the position of the condensation wave seem to be the most important ones in designing a suitable supersonic separator device.

As an example, on the one hand, the more CO_2 is removed from natural gas the more efficient the device is. On the other hand, more entropy is being generated and more reversible work, i.e., exergy, is being lost. Also, by increasing the stagnation pressure it is possible to force condensation to occur closer to the nozzle throat, which is advantageous in the removal of liquid CO_2 as there is more space to remove it, which could lead to a better efficiency.

These remarks were aimed at highlighting some of the relevant aspects of condensing flows so that they may help in the design of supersonic separators and in choosing the best setup for these devices, such as low- or high-pressures, the boundary conditions, the entropy generated in the process and what can be done to reduce the generation of such irreversibilities.

Finally, the main objectives of the present research were to analyze the physical consistency of the thermodynamics models of single component metastable condensation. The branch of SU2 code performed reasonably well and is suitable for such simulations. However, it is necessary to adjust the trigger for metastable condensation, which should be when the vapor temperature reaches the Wilson temperature instead of the saturation temperature. It is believed that in the context of the supersonic separator research it is now possible to move on to metastable condensation of one or more components of a gas mixture, high-speed condensing flows with a swirl device and full Navier-Stokes simulations of metastable condensation.

5.2 Future work

This research project has analyzed the physical accuracy of metastable condensation models available on the branch of the SU2 code as well as generation of entropy which is associated with metastable condensation. Further, only single component Euler flows with condensation and in the absence of shockwaves and re-evaporation of the liquid phase were considered. In order to achieve the results required for the development of the supersonic separator it is necessary to proceed the researches on the topic.

I is necessary to analyze, for instance, the possibility of re-evaporation of the liquid phase. It has been pointed out Azzini (2019); Luo et al. (2006) that re-evaporation may occur in flows with shockwaves. The reason for this is the fact that once a shockwave takes place both pressure and temperature increase while the Mach number decreases. This may lead to total or partial re-evaporation of the liquid phase. On considering that oblique shockwaves may be present in the supersonic separator device as a result of the collectors placed in the divergent section of the nozzle to remove the liquid phase, it is necessary to take re-evaporation into account in the modeling of the device.

Moreover, it is also necessary to implement a more accurate condensation model since the condensation model available on the SU2 branch is triggered with respect to the saturation temperature and, according to the literature Azzini (2019); Lettieri et al.

(2017), it should be the Wilson temperature for metastable condensation. This lead to the average droplet radius becoming greater than the critical radius in the convergent section of the nozzle in the Moore B nozzle simulation. This result is incorrect since it is expected that this should only occur in the divergent section of the nozzle where the flow is supersonic. Therefore, it is necessary to correct the code in order to obtain results which are in better agreement with the theory.

At this point the accuracy of the condensation models Costa (2020) and their physical consistency have been tested it is now possible to correctly locate within a certain degree of precision the position of the condensation wave. This allows for the possibility of performing simulations with collectors and to analyze the removal of the liquid phase and whether methane is lost through the collectors. Such simulations only make sense once the position of the condensation wave can be accurately predicted in order to place the collectors after the condensation wave - if the collectors are placed incorrectly before the occurrence of the condensation wave no liquid phase will be removed.

The supersonic separator device has a swirl generator positioned before the Laval nozzle. Therefore, an interesting and important analysis would be to simulate swirling flows with condensation in order to verify how the swirl generator affects the flow and condensation itself. Additionally, the models used in this work assume that the liquid droplets are small enough such that there is no slip between the vapor and liquid phases. A simulation with a swirl generator can also show if this model can predict the centrifugation of liquid phase.

In this dissertation the generation of entropy associated with metastable condensation was analyzed. However, the evolution of entropy throughout the flow was not addressed. Such an investigation requires implementing a suitable equation to evaluate the evolution of entropy such as equation (D.29) in appendix D for the no-slip case. Furthermore, the condensation model available on the SU2 code evaluates the liquid phase temperature by using the so-called capillarity model, equation (3.6), instead of using an equation for the conservation of energy for the liquid phase. An interesting line of investigation could be to implement the equation of conservation of energy for the liquid phase and to analyze the accuracy of both approaches, i.e., the capillarity model and the conservation of energy for the liquid.

Another research opportunity related to this topic is to run numerical simulations of high-speed condensing nozzle flows with the Navier-Stokes equations using a suitable turbulence model. Currently the SU2 branch only has Sparlat-Allmaras (SA) model implemented for such problems. However, the SA model was developed for external flows and may not be the best choice for an internal flow. As a result, a future research project may be related to the implementation of a more suitable turbulence model to be used with high-speed condensing nozzle flows.

In a supersonic separator a gas mixture flows through the nozzle and some of the components of the mixture condense. Therefore, it is necessary to extend the models studied here to gas mixtures, such as in the works of Put (2003); Young (1995). These references analyze two component mixtures, which should be good enough to simulate $CH_4 - CO_2$ mixtures, since these are the main components of natural gas.

BIBLIOGRAPHY

A. Afzalifar, T. Turunen-Saaresti, and A. Grönman. Comparison of Moment-Based Methods for Representing Droplet Size Distributions in Supersonic Nucleating Flows of Steam. *Journal of Fluids Engineering*, 140(2), 10 2017. doi: 10.1115/1.4037979. URL `https://doi.org/10.1115/1.4037979`. 021301.

P. Aursand, M. A. Gjennestad, E. Aursand, M. Hammer, and Øivind Wilhelmsen. The spinodal of single- and multi-component fluids and its role in the development of modern equations of state. *Fluid Phase Equilibria*, 436:98–112, 2017. ISSN 0378-3812. doi: https://doi.org/10.1016/j.fluid.2016.12.018. URL `https://www.sciencedirect.com/science/article/pii/S0378381216306227`.

L. Azzini. Su2-feature_2phase. Available at: `https://github.com/su2code/SU2/tree/feature_2phase`, jan 2018. [Online; accessed 01/23/2022].

L. Azzini. *Numerical investigation of dense condensing flows for next-generation power units*. PhD thesis, Delft University of Technology, 2019.

F. Bakhtar and K. Zidi. Nucleation phenomena in flowing high-pressure steam part 2: Theoretical analysis. *Proceedings of the Institution of Mechanical Engineers, Part A: Journal of Power and Energy*, 204(4):233–242, 1990. doi: 10.1243/PIME_PROC_1990_204_032_02.

F. Bakhtar, J. Young, A. White, and D. Simpson. Classical nucleation theory and its application to condensing steam flow calculations. *Proceedings of The Institution of Mechanical Engineers Part C-journal of Mechanical Engineering Science - PROC INST MECH ENG C-J MECH E*, 219:1315–1333, 12 2005. doi: 10.1243/095440605X8379.

J. Barrett and C. Clement. Growth rates for liquid drops. *Journal of Aerosol Science*, 19(2):223–242, 1988. ISSN 0021-8502. doi: https://doi.org/10.1016/0021-8502(88)90225-X. URL `https://www.sciencedirect.com/science/article/pii/002185028890225X`.

F. Beaubert, H. Pálsson, S. Lalot, I. Choquet, and H. Bauduin. Design of a device to induce swirling flow in pipes: A rational approach. *Comptes Rendus Mécanique*, 343(1):

1–12, 2015. ISSN 1631-0721. doi: https://doi.org/10.1016/j.crme.2014.09.004. URL `https://www.sciencedirect.com/science/article/pii/S1631072114001776`.

R. Becker and W. Döring. Kinetische behandlung der keimbildung in übersättigten dämpfen. *Annalen der Physik*, 416(8):719–752, 1935. doi: https://doi.org/10.1002/andp.19354160806.

X. Cao and J. Bian. Supersonic separation technology for natural gas processing: A review. *Chemical Engineering and Processing - Process Intensification*, 136:138 – 151, 2019. ISSN 0255-2701. doi: https://doi.org/10.1016/j.cep.2019.01.007. URL `http://www.sciencedirect.com/science/article/pii/S0255270118312698`.

A. Cato, M. Hayashi, J. Cavalcante, J. Qasem, L. Kavabata, U. Costa, and E. Volpe. Adjoint-based study of the aerodynamic center shift in the transonic flow regime. International Council of Aeronautical Sciences (ICAS), September 2021.

J. Cavalcante, U. Costa, E. Volpe, M. Hayashi, L. Kavabata, and A. Cato. Parametric optimization of a supersonic swirling separator. 18th Brazilian Congress of Thermal Sciences and Engineering (ENCIT), November 2020. doi: doi://10.26678/ABCM.ENCIT2020.CIT20-0413.

B. Choi, J. Shim, C. Kim, J. Park, D. You, and J. Baek. Numerical simulation of homogeneous condensing wet-steam flow using an eulerian-lagrangian method. 2017.

U. Costa, L. Kavabata, E. Volpe, A. Cato, J. Cavalcante, and M. Hayashi. Numerical investigation of condensing flows in a supersonic separator. 18th Brazilian Congress of Thermal Sciences and Engineering (ENCIT), November 2020. doi: doi://10.26678/ABCM.ENCIT2020.CIT20-0422.

U. A. S. Costa. Numerical investigation of condensing flows in a supersonic separator. Master's thesis, Polytechnic School of the University of São Paulo, Department of Mechanical Engineering, 2020.

S. Dykas and W. Wróblewski. Single- and two-fluid models for steam condensing flow modeling. *International Journal of Multiphase Flow*, 37(9):1245–1253, 2011. ISSN 0301-9322. doi: https://doi.org/10.1016/j.ijmultiphaseflow.2011.05.008. URL `https://www.sciencedirect.com/science/article/pii/S0301932211001157`.

T. Economon, F. Palacios, S. Copeland, T. Lukaczyk, and J. Alonso. SU2: An open-source suite for multiphysics simulation and design. *AIAA Journal*, 54:1–19, 12 2015. doi: 10.2514/1.J053813.

F. Gelbard and J. H. Seinfeld. The general dynamic equation for aerosols. theory and application to aerosol formation and growth. *Journal of Colloid and Interface Science*, 68(2):363 – 382, 1979. ISSN 0021-9797. doi: https://doi.org/10.1016/0021-9797(79)90289-3. URL `http://www.sciencedirect.com/science/article/pii/0021979779902893`.

A. Gerber and A. Mousavi. Application of quadrature method of moments to the polydispersed droplet spectrum in transonic steam flows with primary and secondary nucleation. *Applied Mathematical Modelling - APPL MATH MODEL*, 31:1518–1533, 08 2007. doi: 10.1016/j.apm.2006.04.011.

S. Girshick, C. Chiu, and P. McMurry. Time-dependent aerosol models and homogeneous nucleation rates. *Aerosol Science and Technology*, 13(4):465–477, 1990. doi: 10.1080/02786829008959461. URL `https://doi.org/10.1080/02786829008959461`.

H. Grad. *Principles of the Kinetic Theory of Gases*, pages 205–294. Springer Berlin Heidelberg, 1958. ISBN 978-3-642-45892-7. doi: 10.1007/978-3-642-45892-7_3.

M. Grübel, J. Starzmann, M. Schatz, and D. M. Vogt. Modelling of condensing steam flows in laval nozzles with ansys cfx. *Proceedings of the Institution of Mechanical Engineers, Part A: Journal of Power and Energy*, 232(5):571–575, 2018. doi: 10.1177/0957650917730664. URL `https://doi.org/10.1177/0957650917730664`.

G. Gyarmathy. The spherical droplet in gaseous carrier streams: Review and synthesis. *Multiphase Science and Technology*, 1:99–279, 1982.

G. Gyarmathy. Nucleation of steam in high-pressure nozzle experiments. *Proceedings of the Institution of Mechanical Engineers, Part A: Journal of Power and Energy*, 219(6):511–521, 2005. doi: 10.1243/095765005X31388.

R. Hagmeijer. Equivalence of two different integral representations of droplet distribution moments in condensing flow. *Physics of Fluids*, 16(1):176–183, 2004. ISSN 1070-6631. doi: 10.1063/1.1630052.

R. Hagmeijer, R. H. A. Ijzermans, and F. Put. Solution of the general dynamic equation along approximate fluid trajectories generated by the method of moments. *Physics of Fluids*, 17(5):056101, 2005. doi: 10.1063/1.1921147.

P. G. Hill. Condensation of water vapour during supersonic expansion in nozzles. *Journal of Fluid Mechanics*, 25(3):593–620, 1966. doi: 10.1017/S0022112066000284.

C. Hirsch. *Numerical Computation of Internal and External Flows*, volume 2. Butterworth-Heinemann Limited, 2nd edition, 2007. ISBN 9780750665957.

V. Hric and J. Halama. Performance of simple condensation model in high-pressures. 01 2016. doi: 10.14311/TPFM.2016.009.

S. Imaev, L. Bagirov, V. Borisov, and E. Voytenkov. New low temperature process of co2 recovery from natural gases. 01 2014. doi: 10.2118/171427-MS.

R. Jackson and B. Davidson. An equation set for non-equilibrium two phase flow, and an analysis of some aspects of choking, acoustic propagation, and losses in low pressure wet steam. *International Journal of Multiphase Flow*, 9(5):491–510, 1983. ISSN 0301-9322. doi: https://doi.org/10.1016/0301-9322(83)90014-9. URL `https://www.sciencedirect.com/science/article/pii/0301932283900149`.

A. Kantrowitz. Nucleation in very rapid vapor expansions. *J. Chem. Phys.*, 19(9): 1097–1100, sep 1951. doi: 10.1063/1.1748482.

L. Kavabata, U. Costa, A. Cato, J. Cavalcante, J. Nunes, E. Volpe, J. Azevedo, and M. Hayashi. Numerical investigation of metastable condensation of wet steam under high-pressure conditions. 26th International Congress of Mechanical Engineering (COBEM), November 2021. doi: doi://10.26678/ABCM.COBEM2021.COB2021-0567.

A. Kluwick. Non-ideal compressible fluid dynamics: A challenge for theory. *Journal of Physics: Conference Series*, 821:012001, mar 2017. doi: 10.1088/1742-6596/821/1/012001. URL `https://doi.org/10.1088/1742-6596/821/1/012001`.

S. D. Leal, M. Embiruçu, G. M. N. Costa, and K. V. Pontes. Prediction of thermodynamic properties of CO2 by cubic and multiparameter equations of state for fluid dynamics applications. *Journal of Chemical & Engineering Data*, 64(4):1746–1759, 2019. doi: 10.1021/acs.jced.8b01238. URL `https://doi.org/10.1021/acs.jced.8b01238`.

C. Lettieri, D. Paxson, Z. Spakovszky, and P. Bryanston-cross. Characterization of non-equilibrium condensation of supercritical carbon dioxide in a de laval nozzle. *Journal of Engineering for Gas Turbines and Power*, 140, 09 2017. doi: 10.1115/1.4038082.

F.-Y. Liang, M. Ryvak, S. Sayeed, and N. Zhao. The role of natural gas as a primary fuel in the near future, including comparisons of acquisition, transmission and waste handling costs of as with competitive alternatives. *Chemistry Central journal*, 6 Suppl 1:S4, 04 2012. doi: 10.1186/1752-153X-6-S1-S4.

E. Lifshitz and L. Landau. *Course of Theoretical Physics Volume 10: Physical Kinetics*, volume 10 of *Course of theoretical physics*. Robert Maxwell, M.C., 1st edition, 1981. ISBN 9780750626354. Pergamon International Library of Science, Technology, Engineering and Social Studies.

C. Luijten. *Nucleation and droplet growth at high pressure*. PhD thesis, Applied Physics, 1998.

X. Luo, B. Prast, M. E. H. van Dongen, H. W. M. Hoeijmakers, and J. Yang. On phase transition in compressible flows: modelling and validation. *Journal of Fluid Mechanics*, 548:403–430, 2006. doi: 10.1017/S0022112005007809.

X. Luo, Y. Cao, and F. Qin. A phase-slip moment method for condensing flows. *International Journal of Heat and Mass Transfer*, 118:1257–1263, 03 2018. doi: 10.1016/j.ijheatmasstransfer.2017.11.028.

P. Machado, J. Monteiro, J. de Medeiros, H. Epsom, and O. Araújo. Supersonic separation in onshore natural gas dew point plant. *Journal of Natural Gas Science and Engineering*, 6:43, 05 2012. doi: 10.1016/j.jngse.2012.03.001.

R. McGraw. Description of aerosol dynamics by the quadrature method of moments. *Aerosol Science and Technology*, 27(2):255–265, 1997. doi: 10.1080/02786829708965471. URL `https://doi.org/10.1080/02786829708965471`.

A. Monin and A. Yaglom. *Statistical Fluid Mechanics: Mechanics of Turbulence*, volume 1 of *Dover Books on Physics*. Dover Publications, 2013a.

A. Monin and A. Yaglom. *Statistical Fluid Mechanics: Mechanics of Turbulence*, volume 2 of *Dover Books on Physics*. Dover Publications, 2013b.

M. Moore, P. Walters, R. Crane, and B. Davidson. Predicting the fog-drop size in wet-steam turbines. *Wet steam 4 Conf.*, 1973.

C. A. Moses and G. D. Stein. On the Growth of Steam Droplets Formed in a Laval Nozzle Using Both Static Pressure and Light Scattering Measurements. *Journal of Fluids Engineering*, 100(3):311–322, 09 1978. ISSN 0098-2202. doi: 10.1115/1.3448672. URL `https://doi.org/10.1115/1.3448672`.

A. Mousavi, A. Gerber, and M. Kermani. Representing polydispersed droplet behavior in nucleating steam flow with the quadrature - method - of - moments. *2006 ASME Joint U.S.-European Fluids Engineering Summer Meeting, FEDSM 2006*, 2006, 08 1920. doi: 10.1115/FEDSM2006-98459.

P. Nederstigt. Real gas thermodynamics: and the isentropic behavior of substances. Master's thesis, Delft University of Technology, 2017.

A. Papoulis and S. U. Pillai. *Probability, Random Variables, and Stochastic Processes.* McGraw Hill, Boston, 4th edition, 2002. ISBN 0071122567 9780071122566 0073660116 9780073660110 0071226613 9780071226615.

P. Peeters, C. Luijten, and M. van Dongen. Transitional droplet growth and diffusion coefficients. *International Journal of Heat and Mass Transfer*, 44(1):181–193, 2001. ISSN 0017-9310. doi: https://doi.org/10.1016/S0017-9310(00)00098-3. URL `https://www.sciencedirect.com/science/article/pii/S0017931000000983`.

D. Peng and D. Robinson. New two-constant equation of state. *Industrial & Engineering Chemistry Fundamentals*, 15, 02 1976. doi: 10.1021/i160057a011.

M. Pini, S. Vitale, P. Colonna, G. Gori, A. Guardone, T. Economon, J. Alonso, and F. Palacios. SU2: the open-source software for non-ideal compressible flows. *Journal of Physics: Conference Series*, 821:012013, mar 2017. doi: 10.1088/1742-6596/821/1/012013. URL `https://doi.org/10.1088/1742-6596/821/1/012013`.

F. Put. *Numerical Simulation of Condensation in Transonic Flows.* PhD thesis, Universiteit Twente, 9 2003.

R. Puzyrewski and T. Król. Numerical analysis of hertz-knudsen model of condensation upon small droplets in water vapor. In *Prace Instytutu Maszyn Przeplywowych*, pages 285–307, Poland, 1976. Polska Akademia Nauk Instytutu Maszyn Przeplywowych.

J.-F. Remacle, F. Henrotte, T. Baudouin, C. Geuzaine, E. Béchet, T. Mouton, and E. Marchandise. A frontal delaunay quad mesh generator using the L ∞ norm. *International Journal for Numerical Methods in Engineering*, pages 455–472, 2010. doi: 10.1007/978-3-642-24734-7_25.

P. Roe. Approximate riemann solvers, parameter vectors, and difference schemes. *Journal of Computational Physics*, 43(2):357–372, 1981. ISSN 0021-9991. doi: https://doi.org/10.1016/0021-9991(81)90128-5. URL `https://www.sciencedirect.com/science/article/pii/0021999181901285`.

V. Rusanov. Calculation of interaction of non-steady shock waves with obstacles. *jour Zh. Vychisl. Mat. Mat. Fiz.*, 1(2):267–279, 1961.

W. Simons and J. Bowen. Investigation of the condensation shock in air by use of the schlieren method. Master's thesis, Massachusetts Institute of Technology. Dept. of Naval Architecture and Marine Engineering, 08 1946.

J. Starzmann, F. R. Hughes, S. Schuster, A. J. White, J. Halama, V. Hric, M. Kolovratník, H. Lee, L. Sova, M. Št'astný, M. Grübel, M. Schatz, D. M. Vogt, Y. Patel, G. Patel, T. Turunen-Saaresti, V. Gribin, V. Tishchenko, I. Gavrilov, C. Kim, J. Baek, X. Wu, J. Yang, S. Dykas, W. Wróblewski, S. Yamamoto, Z. Feng, and L. Li. Results of the international wet steam modeling project. *Proceedings of the Institution of Mechanical Engineers, Part A: Journal of Power and Energy*, 232(5):550–570, 2018. doi: 10.1177/0957650918758779. URL `https://doi.org/10.1177/0957650918758779`.

R. Stryjek and J. H. Vera. PRSV: An improved peng—robinson equation of state for pure compounds and mixtures. *The Canadian Journal of Chemical Engineering*, 64(2):323–333, 1986. doi: https://doi.org/10.1002/cjce.5450640224. URL `https://onlinelibrary.wiley.com/doi/abs/10.1002/cjce.5450640224`.

P. Thompson. *Compressible-fluid Dynamics*. Advanced engineering series. McGraw-Hill Book Company, 1988.

N. B. Vargaftik, B. N. Volkov, and L. D. Voljak. International tables of the surface tension of water. *Journal of Physical and Chemical Reference Data*, 12(3):817,820, 1983-07. ISSN 0047-2689.

M. Vinokur and J.-L. Montagné. Generalized flux-vector splitting and roe average for an equilibrium real gas. *Journal of Computational Physics*, 89(2):276–300, 1990. ISSN 0021-9991. doi: https://doi.org/10.1016/0021-9991(90)90145-Q.

S. Vitale, G. Gori, M. Pini, A. Guardone, T. Economon, F. Palacios, J. Alonso, and P. Colonna. Extension of the SU2 open source CFD code to the simulation of turbulent flows of fluids modelled with complex thermophysical laws. In *22nd AIAA Computational Fluid Dynamics Conference*, 2015. doi: 10.2514/6.2015-2760. URL `https://arc.aiaa.org/doi/abs/10.2514/6.2015-2760`.

C. Wen, A.-Q. Li, J. Walther, and Y. Yang. Effect of swirling device on flow behavior in a supersonic separator for natural gas dehydration. *Separation and Purification Technology*, 168, 05 2016. doi: 10.1016/j.seppur.2016.05.019.

A. White and M. Hounslow. Modelling droplet size distributions in polydispersed wet-steam flows. *International Journal of Heat and Mass Transfer*, 43(11):1873 – 1884,

2000. ISSN 0017-9310. doi: https://doi.org/10.1016/S0017-9310(99)00273-2. URL `http://www.sciencedirect.com/science/article/pii/S0017931099002732`.

Y. Yang and S. Shen. Numerical simulation on non-equilibrium spontaneous condensation in supersonic steam flow. *International Communications in Heat and Mass Transfer*, 36(9):902–907, 2009. ISSN 0735-1933. doi: https://doi.org/10.1016/j.icheatmasstransfer.2009.06.001. URL `https://www.sciencedirect.com/science/article/pii/S0735193309001377`.

J. Young. Semi-analytical techniques for investigating thermal non-equilibrium effects in wet steam turbines. *International journal of heat and fluid flow*, 5(2):81–91, 1984.

J. Young. The condensation and evaporation of liquid droplets in a pure vapour at arbitrary knudsen number. *International Journal of Heat and Mass Transfer*, 34(7): 1649–1661, 1991. ISSN 0017-9310. doi: https://doi.org/10.1016/0017-9310(91)90143-3.

J. Young. The fundamental equations of gas-droplet multiphase flow. *International Journal of Multiphase Flow*, 21(2):175–191, 1995. ISSN 0301-9322. doi: https://doi.org/10.1016/0301-9322(94)00078-X. URL `https://www.sciencedirect.com/science/article/pii/030193229400078X`.

J. B. Young. Spontaneous condensation of steam in supersonic nozzles. 1982.

APPENDIX A – THE ΔG EXPRESSION

The derivation of expression for ΔG presented in this appendix follows the steps listed in Appendix 2 of Bakhtar et al. (2005). It is considered that the vapor phase behaves as a perfect gas, i.e., it is thermally perfect - it follows the ideal gas equation of state ($P = \rho RT$) - and it is calorically perfect ($\gamma = c_p/c_v = constant$). Also, it is assumed that the liquid droplets are perfectly spherical.

Firstly, suppose that a vapor is supersaturated and that it is maintained at constant temperature T_v and pressure P_v. According to Bakhtar et al. (2005) it is possible to split the ΔG calculation into four parts.

The first part of the calculation (ΔG_1) considers the isothermal expansion/compression in which the vapor goes from pressure P_v to $P_S(T_v)$ where $P_S(T_v)$ is the saturated vapor pressure at temperature T_v. The second part (ΔG_2) is condensation of the vapor at constant pressure $P_S(T_v)$ and constant temperature T_v. The third part (ΔG_3) is the isothermal compression of the liquid phase from pressure $P_S(T_v)$ to P_v . The fourth and final part (ΔG_4) is related to the formation of a spherical droplet of radius r.

For ΔG_1 we have

$$\Delta G_1 = \frac{4}{3}\pi r^3 \rho_l \int_{P_v}^{P_S(T_v)} \frac{dP}{\rho} \tag{A.1}$$

Where r is the droplet radius, and ρ_L the liquid density.

Considering the ideal gas EoS

$$P = \rho RT \tag{A.2}$$

Substituting (A.2) into (A.1) we have

$$\Delta G_1 = \frac{4}{3}\pi r^3 \rho_l R T_v \int_{P_v/(RT_v)}^{P_S(T_v)/(RT_v)} \frac{d\rho_v}{\rho_v} \tag{A.3}$$

Note that the limits of integration have changed from P_v to $\rho_v = P_v/(RT_v)$ which is the density at pressure P_v and from $P_S(T_v)$ to $\rho_S(T_v) = P_S(T_v)/(RT_v)$ which is the density at pressure $P_S(T_v)$.

Then, we have

$$\Delta G_1 = \frac{4}{3}\pi r^3 \rho_l R T_v \ln\left[\frac{P_S(T_v)/(RT_v)}{P_v/(RT_v)}\right] \tag{A.4}$$

or

$$\Delta G_1 = -\frac{4}{3}\pi r^3 \rho_l R T_v \ln\left(\frac{P_v}{P_S(T_v)}\right) \tag{A.5}$$

The change in Gibbs free energy for the condensation of the vapor to liquid ΔG_2 is zero Bakhtar et al. (2005) - the process happens at constant pressure and temperature. That is

$$\Delta G_2 = 0 \tag{A.6}$$

As for ΔG_3, the compression of the liquid phase from pressure $P_S(T_v)$ to P_v is

$$\Delta G_3 = \frac{4}{3}\pi r^3 [P_v - P_S(T_v)] \tag{A.7}$$

According to Bakhtar et al. (2005), ΔG_3 is small and ca be neglected. That is

$$\Delta G_3 \approx 0 \tag{A.8}$$

The final term ΔG_4 is related to the work required to form a spherical surface of radius r. Considering the capillarity approximation ΔG_4 is given by

$$\Delta G_4 = 4\pi r^2 \sigma \tag{A.9}$$

Where σ is the surface tension.

The sum of all these four terms then gives

$$\Delta G = \sum_{i=1}^{4} \Delta G_i = -\frac{4}{3}\pi r^3 \rho_l R T_v \ln\left(\frac{P_v}{P_S(T_v)}\right) + 4\pi r^2 \sigma \tag{A.10}$$

Simplifying (A.10) gives

$$\boxed{\Delta G = -\frac{4}{3}\pi r^3 \rho_l R T_v \ln\left(\frac{P_v}{P_S(T_v)}\right) + 4\pi r^2 \sigma} \tag{A.11}$$

Equation (A.11) is valid under the hypothesis that the vapor phase behaves as a perfect gas. For non-ideal gas behavior equation (A.11) cannot be applied and it is recommended Bakhtar et al. (2005) to use the virial equation to derive the ΔG expression.

APPENDIX B – NUCLEATION RATE MODELS

The nucleation of liquid droplets may be modeled using different theories. Some of these theories are phenomenological whereas others are based on statistical mechanics Bakhtar et al. (2005). The main nucleation theories are the Classical Nucleation Theory (CNT) and the Internally Consistent Classical Theory (ICCT) which are both phenomenological theories. There is also the discrete model whereof the results are in good agreement with experimental data but whose computational cost is relatively high Girshick et al. (1990).

The CNT is based on thermodynamic aspects of condensation whereas the ICCT also takes into account kinetic aspects of condensation Girshick et al. (1990). The CNT does not predict accurately the position of the condensation wave whereas the discrete model is able to predict it much more accurately. The main disadvantage of the discrete model is its high computational cost. According to Girshick et al. (1990) the ICCT has lower computational cost than the discrete model and it is able to predict the position of the condensation wave more accurately than the CNT.

A detailed description of the discrete model and of the Internally Consistent Classical Theory (ICCT) is beyond the scope of the present work which is focused on the CNT. For further details regarding the discrete model and the ICCT please refer to Girshick et al. (1990).

The main objective of this section is to describe the Classical Nucleation Theory as well as some of the corrections proposed to improve it. As shall be discussed later on, the CNT is able to predict the occurence of the condensation wave in a flow. However it does not predict its position accurately. Hence different corrections have been proposed to the CNT in order to improve its results.

B.1 The Classical Nucleation Theory (CNT)

The Classical Nucleation Theory (CNT) supposes that, when condensation occurs, the liquid phase consists of spherical droplets that are sufficiently light and small, so as to flow along with the gaseous phase. In other words it assumes mechanical equilibrium between the liquid and gaseous phases Azzini (2019). It also supposes that both phases have the same temperature, i.e., it supposes thermodynamic equilibrium Bakhtar et al. (2005).

As reported by Bakhtar et al. (2005) it is possible to express ΔG in terms of the number of molecules in the cluster (g) instead of r, as in equation (2.1) by making use of the relations presented in table 9

Table 9: Relations used to transform $\Delta G(r)$ into $\Delta G(g)$

Relations
$4\pi r^3\rho_l/3 = gm$
$4\pi r^2 = Ag^{2/3}$
$A^3 = 36\pi(m/\rho_l)^2$
$k = mR$

where m is the mass of a molecule, r the radius of the droplet, and ρ_l is the liquid density.

Then we have

$$\frac{\Delta G}{kT_v} = \frac{A\sigma}{kT_v}g^{2/3} - g\ln S \tag{B.1}$$

Where k is the Boltzmann constant.

It is also possible to write equation (B.1) in terms of the supercooling ΔT_s which is defined as the difference between the vapor temperature T_v and the saturated vapor temperature $T_s(P)$ at a pressure P, i.e., $\Delta T_s = T_v(P) - T_v$. This can be done by using the Clausius-Clapeyron equation Bakhtar et al. (2005) from which it is obtained

$$\ln S \approx \frac{H_e}{RT_s(P)}\frac{\Delta T_s}{T_v} \tag{B.2}$$

Then

$$\frac{\Delta G}{kT_v} \approx \frac{A\sigma}{kT_v}g^{2/3} - \frac{gH_e}{RT_s(P)}\frac{\Delta T_s}{T_v} \tag{B.3}$$

Equation (B.3) shows the relationship between the Gibbs free energy required to form a spherical droplet of radius r and the supercooling ΔT_s.

A cluster containing g molecules is called a g-mer. According to Bakhtar et al. (2005) the steady state number of g-mers per unit volume (n_g) follows approximately a Boltzmann law and it is given by

$$n_g \approx n_1 \exp\left(-\frac{\Delta G}{kT_v}\right) \tag{B.4}$$

Where n_1 is the number of monomers per unit volume and k is the Boltzmann constant.

The cluster concentration will remain steady if there is a balance between the acquisition of new molecules - condensation - and the loss of molecules - evaporation. The balance is given by the following equation

$$C_g n_g \rightleftharpoons E_{g+1} n_{g+1} \tag{B.5}$$

Where C_g is the condensation rate and E_{g+1} is the evaporation rate.

Equations (B.4) and (B.5) are valid for equilibrium conditions in which condensation and evaporation cancel each other out. As reported by Bakhtar et al. (2005), if a cluster grows beyond the critical radius then the balance stated in (B.5) no longer holds since the rate of condensation is greater than the rate of evaporation.

Let I_{CNT} denote the nucleation current which expresses the net rate per unit volume at which g-mers grow to (g+1)-mers, i.e., the rate at which a g-mer acquires a new molecule to become a (g+1)-mer. The nucleation current is then

$$I_g = C_g f_g - E_{g+1} f_{g+1} \tag{B.6}$$

Where f_g is the concentration of g-mers which are bigger than the critical size.

The expressions for C_g and E_{g+1} are derived from kinetic theory Bakhtar et al. (2005) considering spherical droplets

$$C_g = q_c A g^{2/3} \frac{P_v}{\sqrt{2\pi m k T_v}} \tag{B.7}$$

$$E_g = q_e A g^{2/3} \frac{P_S(T_l)}{\sqrt{2\pi m k T_v}} \exp\left(\frac{2\sigma}{\rho_l R T_l r}\right) \tag{B.8}$$

Where q_c is the condensation coefficient, q_e is the evaporation coefficient, $Ag^{2/3} = 4\pi r^2$, $A^3 = 36\pi(m/\rho_l)^2$, m is the mass of a molecule, T_l is the liquid temperature, P_l is the liquid pressure.

The nucleation rate may be expressed as - for a detailed deduction, please refer to sections 2.3 to 2.5 from Bakhtar et al. (2005)

$$J_{CNT} = \left(\int_1^{+\infty} \frac{dg}{C_g n_g} \right)^{-1} \tag{B.9}$$

The integral in equation (B.9) may be solved analytically to obtain a final expression for the nucleation rate - please refer to appendix **??** for the derivation of the nucleation rate equation. Thus, we have

$$J_{CNT} = q_c \frac{\rho_v^2}{\rho_l} \left(\frac{2\sigma}{\pi m^3} \right)^{1/2} \exp\left(-\frac{4\pi r_c^2 \sigma}{3kT_v} \right) \tag{B.10}$$

This was the first nucleation rate model and was proposed by Becker and Döring (1935). Though it can successfully predict the occurrence of condensation phenomena, it fails to give an accurate position of the condensation wave. Different nucleation models have been proposed and they apply correction factors to equation (B.10).

B.2 Non-Isothermal correction

Equation (B.10) is obtained by considering thermodynamic and mechanical equilibrium between the liquid and vapor phases. However in some cases this assumption may lead to incorrect results. The consideration that the liquid and vapor phases have different temperatures was first addressed by Kantrowitz (1951) and his results are quite simple in fact: it simply multiplies the classical nucleation rate by a factor $1/(1+\phi)$. Let the non-isothermal nucleation rate be denoted as J_{NonIso} then

$$J_{NonIso} = \left(\frac{1}{1+\phi} \right) q_c \frac{\rho_v^2}{\rho_l} \left(\frac{2\sigma}{\pi m^3} \right)^{1/2} \exp\left(-\frac{4\pi r_c^2 \sigma}{3kT_v} \right) \tag{B.11}$$

Where

$$\phi = q_c \frac{\rho_v R}{\alpha_r} \sqrt{\frac{RT_v}{2\pi}} \frac{H_e}{RT_v} \left(\frac{H_e}{RT_v} - \frac{1}{2} \right) \tag{B.12}$$

Where H_e is the specific enthalpy of evaporation and α_r is the surface heat transfer coefficient of a droplet whose radius is equal to the critical radius r_c.

It is reported Bakhtar et al. (2005) that for low pressures it is possible to simplify equation (B.12) owing to the fact that the critical radius is considerably smaller than the mean free path of a vapor molecule. Then for low pressures we have

$$\phi = 2q_c\left(\frac{\gamma-1}{\gamma+1}\right)\frac{H_e}{RT_v}\left(\frac{H_e}{RT_v}-\frac{1}{2}\right) \tag{B.13}$$

Where γ is the isentropic specific heat ratio.

B.3 The Internally Consistent Classical Theory (ICCT)

According to Bakhtar et al. (2005) the ΔG expression written as a function of g must equal zero if g is equal to one, i.e., $\Delta G(g = 1) = 0$. In order to achieve this, it is necessary to modify equation (B.1). It was proposed by Girshick et al. (1990) that (B.1) be rewritten as

$$\frac{\Delta G}{kT_v} \approx \frac{A\sigma}{kT_v}(g^{2/3}-1)-(g-1)\text{ln}S \tag{B.14}$$

The ΔG expression in equation (B.14) results in the so-called Internally Consistent Classical Theory (ICCT) whose nucleation rate is given by Girshick et al. (1990); Luo et al. (2006)

$$J_{ICCT} = q_c\frac{\rho_v^2}{\rho_l}\left(\frac{2\sigma}{\pi m^3}\right)^{1/2}\exp\left(\frac{\sigma A}{kT_v}\right)\exp\left(-\frac{4\pi r_c^2\sigma}{3kT_v}\right) \tag{B.15}$$

By comparing equation (B.15) with equation (B.10) it can be seen that

$$J_{ICCT} = \Phi J_{CNT} \tag{B.16}$$

Where

$$\Phi = \exp\left(\frac{\sigma A}{kT_v}\right) \tag{B.17}$$

As pointed out by Bakhtar et al. (2005) the ICCT correction is applied only to the smallest clusters. Because of this, the authors question the validity of the ICCT, despite the fact that its results are more accurate than those of the CNT Girshick et al. (1990).

B.4 The correction factor f

As reported by Choi et al. (2017); Costa (2020); Grübel et al. (2018); Starzmann et al. (2018) equation (B.11) can be modified to include a correction factor - commonly denoted as f - in the exponential term. According to Choi et al. (2017) this factor is used to calibrate the nucleation rate and is reported to produce the best results Choi et al. (2017); Costa et al. (2020); Costa (2020). The nucleation rate with the correction factor

(J_f) is then

$$J_f = q_c\left(\frac{1}{1+\phi}\right)\frac{\rho_v^2}{\rho_l}\left(\frac{2\sigma}{\pi m^3}\right)^{1/2}\exp\left(-f\frac{4\pi r_c^2\sigma}{3kT_v}\right) \tag{B.18}$$

Where ϕ is given by equation (B.12).

APPENDIX C – GROWTH RATE MODELS

C.1 Fundamentals of growth rate models

The process of droplet growth plays an important role in the condensation phenomena. This involves a mass transfer to the droplet - the liquid phase acquires new molecules and grows - and energy transfer from the droplet - the enthalpy difference between the vapor and liquid phases, namely, $h_v - h_l$ is released when the new phase is formed and absorbed by the vapor Luijten (1998).

The growth of a liquid droplet occurs and two different scales: a small Knudsen number region where the process of droplets moving towards and adhering to the droplet is governed by diffusion. The second region is the one with large Knudsen number where the main process affecting the droplet growth is the kinetic process of impingement of molecules onto the liquid droplets Luijten (1998).

For small Knudsen numbers, the droplet radius is considerably greater than the mean free path. For this case, the laws of continuum mechanics are valid and may be applied. For large Knudsen numbers, however, the size of the liquid droplet is smaller than the mean free path of the vapor molecules. For this case, the laws of continuum mechanics are no longer applicable and the kinetic theory of gases is need to model the process. A thorough discussion of kinetic theory of gases is beyond the scope of the present work. The interested reader may refer to Grad (1958); Lifshitz and Landau (1981) for more details on the topic.

An intermediate regime occurs for $Kn \approx 1$. This is referred to as transitional regime Barrett and Clement (1988); Luijten (1998); Peeters et al. (2001) where the size of the liquid droplets is similar to the mean free path of the vapor molecules. Two main models, one by Young (1982) and one by Gyarmathy (1982) attempt to model the phenomena. A third model also appears in the literature is the Hertz-Knudsen model Puzyrewski and Król (1976) and Hill's growth rate model Hill (1966) which is a simplification of the Hertz-Knudsen model.

The following sections present briefly the main growth rate models in the literature. A complete description of these models is beyond the scope of the present work and the interested reader may refer to Barrett and Clement (1988); Luijten (1998); Peeters et al. (2001); Puzyrewski and Król (1976); Young (1982) for a more detailed description of each model.

C.2 Young's model

The growth rate model proposed by Young (1982) considers the transition regime in the model Luijten (1998). It is assumed that the droplet growth is quasi-steady and the model divides the analysis in a Knudsen layer, where the flow is in free molecular flow, and a continuum one, both separated by an interface Luijten (1998); Peeters et al. (2001). A schematic representation of the Young model is given in figure 22.

It is proposed that inside the Knudsen layer, molecules that leave the droplet follow a Maxwell velocity distribution whereas incoming molecules follow a Grad distribution Luijten (1998). Further details of the derivation of the model can be found in Luijten (1998); Young (1982).

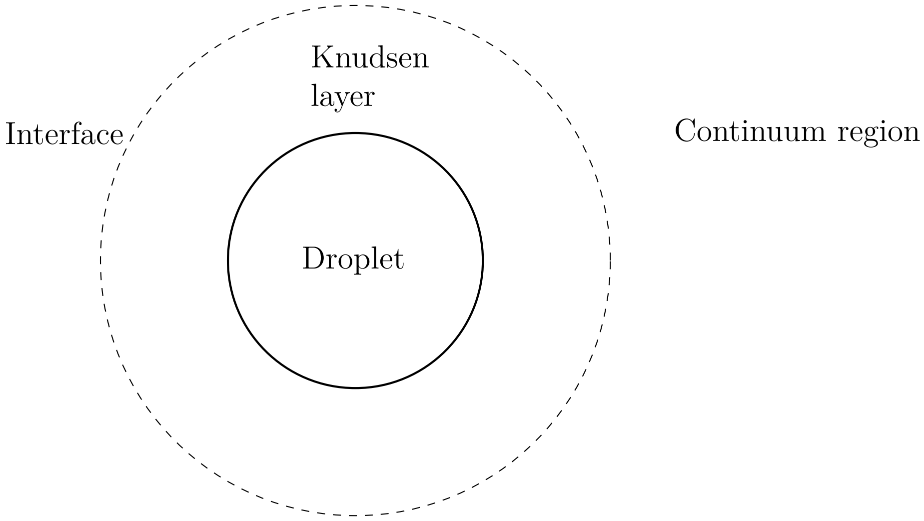

Figure 22: Droplet growth model of Young Young (1982).

The growth rate model by Young Young (1982) is expressed as follows Starzmann et al. (2018)

$$\left.\frac{dr}{dt}\right|_{Y} = \frac{\lambda_v(1 - r_c/r)(T_l - T_v)}{\rho_l H_e r(\frac{1}{1+2\beta Kn} + 3.78(1 - \nu_Y)\frac{Kn}{Pr})} \tag{C.1}$$

and

$$\nu_Y = \frac{RT_s(P)}{H_e}\left[\alpha - 0.5 - \left(\frac{2-q_c}{2q_c}\right)\left(\frac{\gamma+1}{2\gamma}\right)\left(\frac{C_p^v T_s(P)}{H_e}\right)\right] \tag{C.2}$$

Where Pr is the Prandtl number, α is a parameter that relates the condensation (q_c) and evaporation (q_e) coefficients, and β is correction factor. According to Young (1982) α is related to q_c and q_e by the following relation

$$\frac{q_c}{q_e} = 1 + \alpha\left[\frac{T_l - T_v}{T_s(P)}\right] \tag{C.3}$$

C.3 Gyarmathy's model

The Gyarmathy model Gyarmathy (1982) proposes a growth rate model that can be applied to both the continuum and free molecular regions Puzyrewski and Król (1976). According to Luijten (1998), this model uses an interpolating fit is used between the continuum and free molecular regime. It differs from Young's model since it describes the flow in the Knudsen and in the continuum layers separately and it assumes that all velocities in the Knudsen layer follow the Maxwell velocity distribution Luijten (1998).

The Gyarmathy model is given by

$$\left.\frac{dr}{dt}\right|_G = \frac{\lambda_v(T_l - T_v)}{\rho_l H_e r(1 + 3.18Kn)} \tag{C.4}$$

Where λ_v is the vapor thermal conductivity and kn is the Knudsen number.

C.4 Hertz-Knudsen model

This was the first droplet growth rate model and has the following form Hagmeijer et al. (2005); Puzyrewski and Król (1976)

$$\left.\frac{dr}{dt}\right|_{HK} = \frac{2q_c}{2-q_c}\frac{m}{\rho_l\sqrt{2\pi mk}}\left[\frac{P_v}{\sqrt{T_v}} - \frac{P_{sat}(T_l)}{\sqrt{T_l}}e^{\frac{2\sigma}{\rho_l T_l r}}\right] \tag{C.5}$$

Where α_c is the condensation coefficient, m is the mass of a molecule, R is the gas constant, and k the Boltzmann constant.

The terms in square brackets represent the net condensation rate per unit area. It is assumed that no molecules are deflected, i.e., all vapor molecules that collide with the droplet adhere to it. The term $P_v/\sqrt{T_v}$ represents the vapor molecules that condense whereas the term $(P_{sat}(T_l)/\sqrt{T_l})e^{(2\sigma/\rho_l T_l r)}$ represents the molecules that evaporate. Also, the term $2\alpha_c/(2-\alpha_c)$ is introduced to account for the fact that not all vapor molecules that collide with the droplet surface condense.

In an equilibrium situation the rate of condensation is equal to the rate of evaporation. Thus

$$P_{sat}(T_v) = P_v \tag{C.6}$$

$$T_l = T_v \tag{C.7}$$

and the growth rate term is equal to zero.

As pointed out by Puzyrewski and Król (1976), for a metastable equilibrium condition

$$T_l = T_v \tag{C.8}$$

Then sum of the terms in square brackets is equal to zero, which leads to the expression for the critical droplet radius (r_c) Puzyrewski and Król (1976).

$$\begin{aligned} \frac{P_v}{\sqrt{T_v}} - \frac{P_{sat}(T_l)}{\sqrt{T_l}} e^{\frac{2\sigma}{\rho_l T_l r_c}} &= 0 \Leftrightarrow \\ ln\left(\frac{P_v}{T_v}\right) - ln\left(\frac{P_{sat}}{T_v}\right) &= \frac{2\sigma}{\rho_l T_l r_c} \Leftrightarrow \\ r_c &= \frac{2\sigma}{\rho_l T_l r_c ln(P_v/P_{sat}(T_v))} \end{aligned} \tag{C.9}$$

Note that equation (C.9) is equal to equation (2.2).

C.5 Hill's model

The growth model proposed by Hill Hill (1966) is based on the Hertz-Knudsen model Hill (1966); Puzyrewski and Król (1976). It assumes that the growth rate is weakly dependent on the droplet radius r and sets the exponential term in equation (C.5) to approximately unity Puzyrewski and Król (1976).

$$e^{\frac{2\sigma}{\rho_l T_l r}} \approx 1$$

Hence

$$\left.\frac{dr}{dt}\right|_{Hill} = \frac{2q_c}{2-q_c} \frac{m}{\rho_l \sqrt{2\pi m k}} \left[\frac{P_v}{\sqrt{T_v}} - \frac{P_{sat}(T_l)}{\sqrt{T_l}}\right] \tag{C.10}$$

APPENDIX D – CONSERVATION EQUATIONS

Conservation equations are necessary to solve vapor-droplet problems. However, these kind of problems require extra equations. As reported by Young (1995), an additional relation for the conservation of droplets is included in the system of equations composed of mass continuity equations, momentum equations, and energy equation.

In the present work, the droplet conservation equation is given by the zeroth order moment. The liquid mass continuity equation is given by the third order moment, which is related to the wetness fraction Put (2003). The first and second order moment equations are necessary to the calculation of the third order moment, as the moment equations are written recursively (section 2.3).

A comprehensive discussion on mass, energy, momentum conservation equations, and entropy equations concerning single component flows in the absence of phase change can be found in Thompson (1988). For the case of flows with phase change, two approaches can be used to model the phenomena: the so-called single phase model, which writes the conservation and entropy equations for the vapor and liquid phases together, and the two-phase model, which writes separate set of equations for each phase. The latter model is reported to be more accurate than the former one Azzini (2019); Dykas and Wróblewski (2011).

On writing separate equations for the vapor and liquid phases, inter-phase transfer terms appear in the conservation equations. Therefore, the discussion presented in Thompson (1988) needs to be extended and include these terms as presented in Dykas and Wróblewski (2011); Luo et al. (2018); Young (1995). A brief discussion on the topic will be discussed in the following subsections.

For the following subsections, let ϑ be a volume with a closed surface Ω and let $\delta\vartheta$ be a small control volume within ϑ. The flow is considered to be inviscid, adiabatic, and unsteady.

D.1 Droplet conservation equation

Let n_l denote the number of spherical liquid droplets per unit mass of vapor plus liquid. Thus, the equation for n_l can be written in the following control volume form Young (1995)

$$\frac{\partial}{\partial t}\iiint_{\vartheta}\rho_m n_l dV + \oiint_{\Omega} n_l u_i dA_i = \iiint_{\vartheta}\rho_m J dV \tag{D.1}$$

Where u_i is the velocity vector of the liquid phase, A_i is the element of area with an outward normal vector, and J is the nucleation rate of droplets per unit mass of vapor plus liquid.

By applying Gauss's Theorem and by letting $\delta\vartheta$ become infinitesimally small, one obtains

$$\frac{\partial(\rho_m n_l)}{\partial t} + \frac{\partial(\rho_m n_l u_i)}{\partial x_i} = \rho_m J \tag{D.2}$$

For the two-phase fluid

$$\frac{\partial(\rho_m)}{\partial t} + \frac{\partial(\rho_m \bar{u}_i)}{\partial x_i} = 0 \tag{D.3}$$

Where $\bar{u}_i$ is the velocity vector of the two-phase fluid.

For the case of no-slip between the vapor and liquid phases $\bar{u}_i = u_i$, and thus

$$\boxed{\frac{\partial n_l}{\partial t} + \frac{\partial(n_l u_i)}{\partial x_i} = J} \tag{D.4}$$

Note the similarity between equations (D.4) and (2.28a). This occurs due to the fact that the method of moments estimates the value of n_l through the zeroth order moment, namely μ_0 Azzini (2019); Hagmeijer (2004); Put (2003); White and Hounslow (2000); Young (1995).

As reported by Young (1984), the assumption of no-slip between the vapor and liquid phases is acceptable for the case of condensing flows under low pressure conditions, in which the droplet radii is in the range of $0.05\mu m < r < 0.5\mu m$, where r is the droplet radius.

D.2 Mass conservation equation

The continuity equation for a two-phase fluid can be written in the following control volume form Young (1995)

$$\frac{\partial}{\partial t}\iiint_{\vartheta}\rho_m dV + \oiint_{\Omega}\rho_m(1-y)v_i dA_i + \oiint_{\Omega}\rho_m y u_i dA_i = 0 \tag{D.5}$$

Where v_i is the velocity vector of the vapor phase and $(1-y)$ is the mass fraction of vapor.

By applying the same procedure of the previous subsection, one has

$$\frac{\partial \rho_m}{\partial t} + \frac{\partial[\rho_m(1-y)v_i]}{\partial x_i} + \frac{\partial(\rho_m y u_i)}{\partial x_i} = 0 \tag{D.6}$$

According to Young (1995), the mass conservation equation for the liquid phase can be obtained by multiplying (D.2) by the liquid mass m_l and by using the multiplication rule for derivatives

$$m_l\left[\frac{\partial(\rho_m n_l)}{\partial t} + \frac{\partial(\rho_m n_l u_i)}{\partial x_i}\right] = m_l\rho_m J \Rightarrow$$

$$\frac{\partial(\rho_m n_l m_l)}{\partial t} + \frac{\partial(\rho_m n_l m_l u_i)}{\partial x_i} - \rho_m n_l\left[\frac{\partial m_l}{\partial t} + \frac{\partial(m_l u_i)}{\partial x_i}\right] = \rho_m m_l J$$

$$\frac{\partial(\rho_m y)}{\partial t} + \frac{\partial(\rho_m y u_i)}{\partial x_i} = \rho_m\left\{n_l\left[\frac{\partial m_l}{\partial t} + \frac{\partial(m_l u_i)}{\partial x_i}\right] + m_l J\right\} \tag{D.7}$$

Let

$$\check{m}_l = \frac{\partial m_l}{\partial t} + \frac{\partial(m_l u_i)}{\partial x_i} \tag{D.8}$$

Then

$$\frac{\partial(\rho_m y)}{\partial t} + \frac{\partial(\rho_m y u_i)}{\partial x_i} = \rho_m(n_l\check{m}_l + m_l J) \tag{D.9}$$

Equation (D.7) is related to the third order moment owing to the fact that the liquid mass fraction y is related to μ_3 through equation (2.30). Some author Hill (1966); Put (2003) substitute the third moment equation (2.28d) by a conservation equation of the form of (D.7).

As for the mass conservation for the vapor phase, it can be obtained by subtracting equation (D.7) from (D.6), which leads to

$$\begin{array}{r} \dfrac{\partial[\rho_m(1-y)]}{\partial t} + \dfrac{\partial[\rho_m(1-y)v_i]}{\partial x_i} + \dfrac{\partial(\rho_m y)}{\partial t} + \dfrac{\partial(\rho_m y u_i)}{\partial x_i} = 0 \\ -\left\{\dfrac{\partial(\rho_m y)}{\partial t} + \dfrac{\partial(\rho_m y u_i)}{\partial x_i} = \rho_m\left\{n_l\left[\dfrac{\partial m_l}{\partial t} + \dfrac{\partial(m_l u_i)}{\partial t}\right] + m_l J\right\}\right\} \\ \hline \end{array}$$

$$\frac{\partial[\rho_m(1-y)]}{\partial t} + \frac{\partial[\rho_m(1-y)v_i]}{\partial x_i} = -\rho_m\left\{n_l\left[\frac{\partial m_l}{\partial t} + \frac{\partial(m_l u_i)}{\partial t}\right] + m_l J\right\} \tag{D.10}$$

Note that for spherical droplets

$$\begin{aligned} n_l m_l &= \mu_0 \frac{4}{3}\pi\langle r\rangle^3 \rho_l \Leftrightarrow \\ n_l m_l &= \mu_0 \frac{4}{3}\pi \frac{\mu_3}{\mu_0}\rho_l \Leftrightarrow \\ n_l m_l &= \frac{4}{3}\pi\rho_l\mu_3 = y \end{aligned}$$

For the no-slip case $\bar{u}_i = u_i$, $v_i = u_i$, and from equation (D.3), one has for the liquid phase

$$\frac{\partial y}{\partial t} + \frac{\partial(y\bar{u}_i)}{\partial x_i} = n_l\left[\frac{\partial m_l}{\partial t} + \frac{\partial(m_l\bar{u}_i)}{\partial t}\right] + m_l J \tag{D.11}$$

or

$$\boxed{\frac{\partial y}{\partial t} + \frac{\partial(y\bar{u}_i)}{\partial x_i} = n_l\check{m}_l + m_l J} \tag{D.12}$$

Similarly, for the vapor phase one has

$$\frac{\partial(1-y)}{\partial t} + \frac{\partial[(1-y)\bar{u}_i]}{\partial x_i} = -\left\{n_l\left[\frac{\partial m_l}{\partial t} + \frac{\partial(m_l u_i)}{\partial t}\right] + m_l J\right\} \tag{D.13}$$

or

$$\boxed{\frac{\partial(1-y)}{\partial t} + \frac{\partial[(1-y)\bar{u}_i]}{\partial x_i} = -(n_l\check{m}_l + m_l J)} \tag{D.14}$$

The evolution of the liquid phase may be estimated through the method of moments (section 2.3 and appendix E). In this case, two additional moment equations are needed, as well as the droplet conservation (zeroth order moment) and liquid mass conservation (third order moment), for closure of the system of moment equations. These are the first order $\langle r\rangle$ and second order $\langle r^2\rangle$ moments due to the fact that the moment equations are calculated recursively, i.e., the nth order moment calculation requires the value of the (n-1)st-order moment and so forth.

D.3 Momentum equations

The following derivation of the moment equations does not account for the effects of viscous shear stresses. Also, according to Young (1995), the total force acting on the control surface is simply the vapor pressure integrated over all control surface. This is due to the fact that the surface tension term which appears in the liquid phase pressure, equation (2.12), is balanced by the surface tension force acting on the point where the droplet intersects the control surface as represented schematically in figure 23.

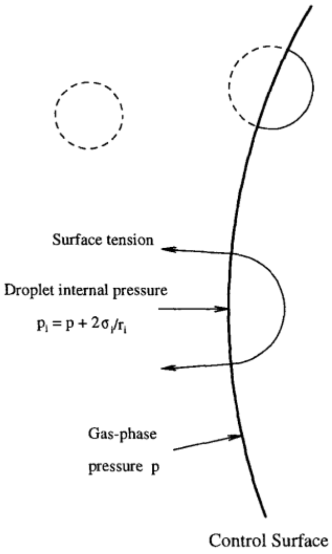

Figure 23: Liquid droplet intersected by the control surface, reproduced from Young (1995).

The control volume formulation for the momentum equations for te two-phase fluid can thus be written as follows

$$\frac{\partial}{\partial t}\left\{\iiint_{\vartheta}\rho_m(1-y)v_i dV+\iiint_{\vartheta}\rho_m y u_i dV\right\}+\oiint_{\Omega}\rho_m(1-y)v_i v_i dA_i+\oiint_{\Omega}\rho_m y u_i u_i dA_i+\oiint_{\Omega}P_v dA_i=0 \tag{D.15}$$

On letting $\delta\vartheta$ become infinitesimally small and on applying Gauss's Theorem to the flux integrals, one obtains the differential form of equation (D.15).

$$\frac{\partial[\rho_m(1-y)v_i]}{\partial t}+\frac{\partial(\rho_m y u_i)}{\partial t}+\frac{\partial[\rho_m(1-y)v_i v_i]}{\partial x_i}+\frac{\partial(\rho_m y u_i u_i)}{\partial x_i}+\frac{\partial P_v}{\partial x_i}=0 \tag{D.16}$$

By applying the differentiation rule of multiplication to the terms on the left hand side of equation (D.16) and on substituting the results of equations (D.7) and (D.10) into equation (D.16), one obtains

$$(1-y)\left[\frac{\partial v_i}{\partial t}+\frac{\partial(v_i v_i)}{\partial x_i}\right]+y\left[\frac{\partial u_i}{\partial t}+\frac{\partial(u_i u_i)}{\partial x_i}\right]=-\frac{1}{\rho_m}\frac{\partial P_v}{\partial x_i}+(n_l\check{m}_l+m_l J)(v_i-u_i) \quad \text{(D.17)}$$

For a case o zero relative velocity between the phases, $\bar{u}_i = v_i = u_i$, one has

$$\boxed{(1-y)\left[\frac{\partial \bar{u}_i}{\partial t}+\frac{\partial(\bar{u}_i \bar{u}_i)}{\partial x_i}\right]+y\left[\frac{\partial \bar{u}_i}{\partial t}+\frac{\partial(\bar{u}_i \bar{u}_i)}{\partial x_i}\right]=-\frac{1}{\rho_m}\frac{\partial P_v}{\partial x_i}} \quad \text{(D.18)}$$

It is worth noting that according to equation (D.18) the only term affecting the momentum equations for an Euler problem in which there is no-slip between the vapor and liquid phases is the pressure gradient.

D.4 Energy conservation equation

On following the approach of Young (1995), the derivation of the energy equation does not take into account the effects of heat conduction, viscosity, and diffusion.

The elemental area δA is split into two parts, $\delta A_{i,v}$ and $\delta A_{i,l}$ Jackson and Davidson (1983); Young (1995). The vapor phase passes only through the control surface $\delta A_{i,v}$ whereas the liquid phases passes only through $\delta A_{i,l}$.

The control volume form of the energy equation can be expressed as follows

$$\begin{aligned}\frac{\partial}{\partial t}\left\{\iiint_\vartheta \rho_m(1-y)\left(e_v+\frac{v_i v_i}{2}\right)dV+\iiint_\vartheta \rho_m y\left(e_l+\frac{u_i u_i}{2}\right)dV\right\}+\\ +\oiint_\Omega \rho_m(1-y)\left(e_v+\frac{v_i v_i}{2}\right)v_i dA_i+\oiint_\Omega \rho_m y\left(e_l+\frac{u_i u_i}{2}\right)u_i dA_i+\\ +\oiint_\Omega \rho_m(1-y)\frac{P_v}{\rho_v}v_i dA_i+\oiint_\Omega \rho_m y\frac{P_v}{\rho_l}u_i dA_i=0 \quad \text{(D.19)}\end{aligned}$$

By adding and subtracting $\partial/\partial t \iiint_\vartheta \rho_m(1-y)P_v/\rho_v$ and $\partial/\partial t \iiint_\vartheta \rho_m y P_v/\rho_l$ to equation (D.19) and on applying the definitions of specific enthalpy, one has

$$\begin{aligned}\frac{\partial}{\partial t}\left\{\iiint_\vartheta \rho_m(1-y)\left(h_v+\frac{v_i v_i}{2}\right)dV+\iiint_\vartheta \rho_m y\left(h_l+\frac{u_i u_i}{2}\right)dV\right\}-\frac{\partial}{\partial t}\iiint_\vartheta \rho_m P\left[\frac{(1-y)}{\rho_v}+\frac{y}{\rho_l}\right]dV+\\ +\oiint_\Omega \rho_m(1-y)\left(h_v+\frac{v_i v_i}{2}\right)v_i dA_i+\oiint_\Omega \rho_m y\left(h_l+\frac{u_i u_i}{2}\right)u_i dA_i=0 \Rightarrow\end{aligned}$$

$$\frac{\partial}{\partial t}\left\{\iiint_{\vartheta}\rho_m(1-y)\left(h_v+\frac{v_iv_i}{2}\right)dV+\iiint_{\vartheta}\rho_m y\left(h_l+\frac{u_iu_i}{2}\right)dV\right\}-\frac{\partial}{\partial t}\iiint_{\vartheta}P_v dV+$$
$$+\oiint_{\Omega}\rho_m(1-y)\left(h_v+\frac{v_iv_i}{2}\right)v_i dA_i+\oiint_{\Omega}\rho_m y\left(h_l+\frac{u_iu_i}{2}\right)u_i dA_i=0 \quad \text{(D.20)}$$

On proceeding in the same way as in the previous subsection, one obtains the differential form of equation (D.20).

$$\frac{\partial}{\partial t}\left[\rho_m(1-y)\left(h_v+\frac{v_iv_i}{2}\right)\right]+\frac{\partial}{\partial x_i}\left[\rho_m(1-y)\left(h_v+\frac{v_iv_i}{2}\right)v_i\right]-\frac{\partial P_v}{\partial t}+$$
$$+\frac{\partial}{\partial t}\left[\rho_m y\left(h_l+\frac{u_iu_i}{2}\right)\right]+\frac{\partial}{\partial x_i}\left[\rho_m y\left(h_l+\frac{u_iu_i}{2}\right)u_i\right]=0 \quad \text{(D.21)}$$

Substituting the results of the the mass conservation equations (D.9) and (D.14) into equation (D.21), one obtains

$$(1-y)\frac{\partial}{\partial t}\left[\left(h_v+\frac{v_iv_i}{2}\right)\right]+\frac{\partial}{\partial x_i}\left[\left(h_v+\frac{v_iv_i}{2}\right)v_i\right]-\frac{\partial P_v}{\partial t}+$$
$$+y\frac{\partial}{\partial t}\left[\left(h_l+\frac{u_iu_i}{2}\right)\right]+y\frac{\partial}{\partial x_i}\left[\left(h_l+\frac{u_iu_i}{2}\right)u_i\right]=(n_l\check{m}_l m_l J)\left[(h_v-h_l)+\left(\frac{v_iv_i}{2}-\frac{u_iu_i}{2}\right)\right] \quad \text{(D.22)}$$

or, in terms of stagnation enthalpy, one has

$$(1-y)\left[\frac{\partial H_{0,v}}{\partial t}+\frac{\partial(H_{0,v}v_i)}{\partial x_i}\right]-\frac{\partial P_v}{\partial t}+y\left[\frac{\partial H_{0,l}}{\partial t}+\frac{\partial(H_{0,l}u_i)}{\partial x_i}\right]=$$
$$=(n_l\check{m}_l m_l J)\left[(h_v-h_l)+\left(\frac{v_iv_i}{2}-\frac{u_iu_i}{2}\right)\right] \quad \text{(D.23)}$$

where $H_{0,v}$ and $H_{0,l}$ are the vapor and liquid stagnation enthalpies, respectively, which are given by

$$H_{0,v}=h_v+\frac{v_iv_i}{2} \quad \text{(D.24a)}$$
$$H_{0,l}=h_l+\frac{u_iu_i}{2} \quad \text{(D.24b)}$$

For the no-slip case $\bar{u}_i=v_i=u_i$, equation (D.23) becomes

$$\boxed{(1-y)\left[\frac{\partial H_{0,v}}{\partial t}+\frac{\partial(H_{0,v}\bar{u}_i)}{\partial x_i}\right]+y\left[\frac{\partial H_{0,l}}{\partial t}+\frac{\partial(H_{0,l}\bar{u}_i)}{\partial x_i}\right]-\frac{\partial P_v}{\partial t}=0} \quad \text{(D.25)}$$

D.5 Entropy production rate equation

As stated by Young (1995), the production of entropy is due to the departure from equilibrium. Also, it is important to write the conservation equations correctly as this impacts the rate of entropy production calculations. An equation in control volume form can be written for the entropy production rate as follows

$$\iiint_{\vartheta} \rho_m \omega dV = \frac{\partial}{\partial t}\left\{ \iiint_{\vartheta} \rho_m (1-y) s_v dV + \iiint_{\vartheta} \rho_m y s_l dV \right\} + \\ + \oiint_{\Omega} \rho_m (1-y) s_v v_i dA_i + \oiint_{\Omega} \rho_m y s_l u_i dA_i \quad \text{(D.26)}$$

Where ω is the rate of production of entropy per unit mass, s_v and s_l are the specific entropy of the vapor and liquid phases, respectively.

On applying Gauss's theorem and on letting $\delta\vartheta$ become infinitesimally small, one obtains the differential form of equation (D.26)

$$\rho_m \omega = \frac{\partial}{\partial t}[\rho_m (1-y) s_v] + \frac{\partial}{\partial x_i}[\rho_m (1-y) s_v v_i] + \frac{\partial(\rho_m y s_l)}{\partial t} + \frac{\partial(\rho_m y s_l u_i)}{\partial x_i} \quad \text{(D.27)}$$

On substituting (D.9) and (D.14) into equation (D.27), one has

$$\omega = \underbrace{\frac{\partial s_v}{\partial t} + \frac{\partial(s_v v_i)}{\partial x_i}}_{\text{vapor contribution}} + \underbrace{\frac{\partial s_l}{\partial t} + \frac{\partial(s_l u_i)}{\partial x_i}}_{\text{liquid contribution}} - \underbrace{(n_l \check{m}_l + m_l J)(s_v - s_l)}_{\text{mass that changes phase contribution}} \quad \text{(D.28)}$$

It is interesting to note that there are three terms which contribute to the generation of entropy: one related to the vapor phase, one associated with the liquid phase, and one associated with the mass of vapor that condenses, i.e., the term $(n_l \check{m}_l + m_l J)$.

On assuming that the relative velocity between the vapor and liquid phases is zero $\bar{u}_i = v_i = u_i$, one has

$$\boxed{\omega = \frac{\partial s_v}{\partial t} + \frac{\partial(s_v \bar{u}_i)}{\partial x_i} + \frac{\partial s_l}{\partial t} + \frac{\partial(s_l \bar{u}_i)}{\partial x_i} - (n_l \check{m}_l + m_l J)(s_v - s_l)} \quad \text{(D.29)}$$

D.6 Final remarks

The equations for the conservation of momentum, energy, and entropy generation were written for the two-phase fluid. It is possible to slit these equations into two equations: one for the vapor and another one for the liquid phase - for a gas mixture it is also possible to include a third set of conservation equations for the non-condensing component of the gas mixture.

To write conservation equation for the phases and/or components separately is quite a difficult task as it involves modeling inter-phase transfer terms. According to Young (1995) this task is a complex one and care must be taken in deriving these equations as wrong assumptions can surely lead to incorrect forms of these equations. Few references provide a careful explanation on the topic. The interested reader may refer to Young (1995) for a detailed derivation of the inter-phase transfer terms.

The conservation equations used in the present work for the vapor phase are given by the system of equations (3.2) which is based on the works ofAzzini (2019); White and Hounslow (2000).

APPENDIX E – THE METHOD OF MOMENTS EQUATIONS

The deductions made in this appendix are based on Put (2003).

Let us rewrite the General Dynamic Equation

$$\frac{\partial f}{\partial t} + \frac{\partial}{\partial r}(Gf) + \frac{\partial (f u_i)}{\partial x_i} = \delta J (r - r_c) \tag{E.1}$$

Where δ is the Dirac delta function, G is the growth rate, J is the nucleation rate and f is a distribution function which is defined by equation (2.25), which can be rewritten as

$$n(r, \vec{x}, t) = \int_0^r f(r, \vec{x}, t) dr \tag{E.2}$$

Where $n(r, \vec{x}, t)$ is the droplet number density.

We then multiply equation (E.1) by r^n. Thus, obtaining

$$r^n \frac{\partial f}{\partial t} + r^n \frac{\partial}{\partial r}(Gf) + r^n \frac{\partial (f u_i)}{\partial x_i} = J r^n \delta (r - r_c) \tag{E.3}$$

It is necessary to use the rule for differentiating the product uv, where u and v are any two differentiable functions. Let $u = r^n$. Then

$$r^n \frac{\partial v}{\partial x_j} = \frac{\partial (r^n v)}{\partial x_j} - v \frac{\partial r^n}{\partial x_j} \tag{E.4}$$

The differentiable function v will take the values f and $f u_i$.

Substituting (E.4) into (E.3) we have

$$\frac{\partial (r^n f)}{\partial t} - f \frac{\partial r^n}{\partial t} + r^n \frac{\partial}{\partial r}(Gf) + \frac{\partial (r^n f u_i)}{\partial x_i} - f u_i \frac{\partial r^n}{\partial x_i} = J r^n \delta (r - r_c) \tag{E.5}$$

On rearranging the terms in equation (E.5) we have

$$\frac{\partial (r^n f)}{\partial t} + r^n \frac{\partial}{\partial r}(Gf) + \frac{\partial (r^n f u_i)}{\partial x_i} - f \left(\frac{\partial r^n}{\partial t} + u_i \frac{\partial r^n}{\partial x_i} \right) = J r^n \delta (r - r_c) \tag{E.6}$$

Note that the fourth term on the left hand side of equation (E.6) is the total (or material) derivative of r^n which is given by

$$\frac{Dr^n}{Dt} \equiv \frac{\partial r^n}{\partial t} + u_i \frac{\partial r^n}{\partial x_i} \tag{E.7}$$

In order to obtain the final equations of moments, it is necessary that the material derivative of r^n be equal to zero — this is a seemingly strong assumption which is required to obtain the final moment equations. Thus we have

$$\frac{Dr^n}{Dt} = 0 \tag{E.8}$$

We would have, provided that (E.8) holds.

$$\frac{\partial(r^n f)}{\partial t} + r^n \frac{\partial}{\partial r}(Gf) + \frac{\partial(r^n f u_i)}{\partial x_i} = J r^n \delta(r - r_c) \tag{E.9}$$

We now integrate equation (E.9) with respect to r from 0 to ∞.

$$\int_0^\infty \frac{\partial(r^n f)}{\partial t} dr + \int_0^\infty r^n \frac{\partial}{\partial r}(Gf) dr + \int_0^\infty \frac{\partial(r^n f u_i)}{\partial x_i} dr = \int_0^\infty J r^n \delta(r - r_c) dr \tag{E.10}$$

As mentioned in chapter 2.3, it is assumed that there is no phase slip. Therefore the velocity u_i is not a function of the droplet radius r so that

$$\frac{\partial}{\partial t} \int_0^\infty r^n f dr + \frac{\partial}{\partial x_i}\left(u_i \int_0^\infty r^n f dr\right) = \int_0^\infty J r^n \delta(r - r_c) dr - \int_0^\infty r^n \frac{\partial}{\partial r}(Gf) dr \tag{E.11}$$

Now we define the moment of order n as

$$\langle r^n \rangle \equiv \int_0^\infty r^n f dr \qquad (n{=}0{,}1{,}...) \tag{E.12}$$

The moment μ_n with the subscript n is not to be confused with the viscosity μ.

Then

$$\frac{\partial\langle r^n\rangle}{\partial t} + \frac{\partial(u_i \langle r^n \rangle)}{\partial x_i} = J \int_0^\infty r^n \delta(r - r_c) dr - \int_0^\infty r^n \frac{\partial}{\partial r}(Gf) dr \tag{E.13}$$

Note that J depends only on r_c and not on r - it can be taken outside of the integral.

We now proceed to evaluate the integrals on the right hand side of equation (E.13). The first integral on the right hand side of (E.13) can be easily evaluated using the following Dirac delta property

$$\int_{-\infty}^{\infty} f(x)\delta(x-a) = f(a) \tag{E.14}$$

For $a > 0$ we have can write

$$\int_{0}^{\infty} f(x)\delta(x-a) = f(a) \tag{E.15}$$

Thus

$$\int_{0}^{\infty} r^n \delta(r-r_c)dr = r_c^n \tag{E.16}$$

On substituting (E.16) into (E.13) we have

$$\frac{\partial\langle r^n\rangle}{\partial t} + \frac{\partial(u_i\langle r^n\rangle)}{\partial x_i} = Jr_c^n - \int_{0}^{\infty} r^n \frac{\partial}{\partial r}(Gf)dr \tag{E.17}$$

The last integral on the right hand side of (E.13) can be evaluated analytically integrating it with the integration by parts method. On integrating (E.13) by parts we have

$$\int udv = \int d(uv) - \int vdu \tag{E.18}$$

Table 10 presents the relations that were made in order to perform the integration

Table 10: Integration by parts relations

Relations	
$u = r^n$	$du = nr^{n-1}dr$
$dv = \frac{\partial}{\partial r}(\frac{dr}{dt}f)dr$	$v = \frac{dr}{dt}f$

Thus we have

$$\int_{0}^{\infty} r^n \frac{\partial}{\partial r}(Gf)dr = [r^n fG]_0^{\infty} - \int_{0}^{\infty} nr^{n-1}fGdr \tag{E.19}$$

The term dr/dt in the integral on the right hand side of (E.19) is a function of r, $\vec{x}$, and t Put (2003), i.e., $dr/dt = dr(r,\vec{x},t)/dt$. In order to take it outside of the integral we define Hill's radius (r_{Hill})

$$r_{Hill} \equiv \left(\frac{\mu_2}{\mu_0}\right)^{1/2} \tag{E.20}$$

Where μ_2 is the second order moment and μ_0 is the zeroth order moment. Note that $r_{Hill} \propto r$.

In this way we may write dr/dt in terms of r_{Hill} instead of r, i.e., $dr/dt = dr(r_{Hill}, \vec{x}, t)/dt$, so that it may be taken outside of the integral in (E.19). The first term on the right hand side of equation (E.19) is equal to zero since the radius size distribution function approaches zero for infinitely large radius ($r \to \infty$) and for radius equal to zero ($r = 0$), i.e., there are no droplets with radius equal to zero and nor infinitely large droplets Put (2003). Then

$$\int_0^\infty r^n \frac{\partial}{\partial r}\left(\frac{dr}{dt}f\right)dr = -nG\langle r^{n-1}\rangle \tag{E.21}$$

Where

$$\langle r^{n-1}\rangle = \int_0^\infty r^{n-1} f dr \tag{E.22}$$

Finally, substituting (E.21) into (E.17) we have

$$\boxed{\frac{\partial\langle r^n\rangle}{\partial t} + \frac{\partial(u_i\langle r^n\rangle)}{\partial x_i} = J r_c^n + nG\langle r^{n-1}\rangle} \tag{E.23}$$

Which is the the moment equation (2.26).

Note that one may use as many moment equations as needed. If a problem presents m unknown parameters, for instance, one may write m moment equations for each unknown parameter - there is no insolvable closure problem.

For the condensation model, only four moments - the zeroth order moment and the first three - are used together with the three conservation equations. Unlike the case of turbulence, condensation - with the additional moment equations - is a closed problem.

APPENDIX F – SU2 THERMODYNAMIC MODELS FOR WET-STEAM AND WATER

In this appendix presents several models used in the SU2 code, e.g., the density mixture model, saturation pressure, etc, to simulate the condensation of water. Other substances such as CO_2 may require different models.

F.1 Saturation pressure model

The saturation pressure model is given by

$$P_{sat} = 10^6 \times \left(\frac{2q[2]}{-q[1] + \sqrt{q[1]^2 - 4q[0]q[2]}} \right)^4 \tag{F.1}$$

Where

$$\mathbf{q} = \begin{bmatrix} q[0] \\ q[1] \\ q[2] \end{bmatrix} = \begin{bmatrix} Q^2 + C[0]Q + C[1] \\ C[2]Q^2 + C[3]Q + C[4] \\ C[5]Q^2 + C[6]Q + C[7] \end{bmatrix} \tag{F.2}$$

And

$$Q = T_{min} + \frac{C[8]}{T_{min} - C[9]} \tag{F.3}$$

Where T_{min} is given by

$$T_{min} = \min(T, T_{Sat}) \tag{F.4}$$

And the saturation coefficients C are given by

$$\mathbf{C} = \begin{bmatrix} C[0] \\ C[1] \\ C[2] \\ C[3] \\ C[4] \\ C[5] \\ C[6] \\ C[7] \\ C[8] \\ C[9] \end{bmatrix} = \begin{bmatrix} 0.11670521452767 \times 10^4 \\ -0.72421316703206 \times 10^6 \\ -0.17073846940092 \times 10^2 \\ 0.12020824702470 \times 10^5 \\ -0.32325550322333 \times 10^7 \\ 0.14915108613530 \times 10^2 \\ -0.48232657361591 \times 10^4 \\ 0.40511340542057 \times 10^6 \\ -0.23855557567849 \\ 0.65017534844798 \times 10^3 \end{bmatrix} \tag{F.5}$$

F.2 Saturation temperature model

The saturation temperature model is given by

$$T_{sat} = \frac{1}{2}\{-[(C[9]+\xi)^2 - 4(C[9]+C[8]\xi)]^{1/2} + C[9] + \xi\} \tag{F.6}$$

Where

$$\begin{cases} \xi = 2\delta/(-\iota - \sqrt{\iota^2 - 4\beta\delta}) \\ \beta = \alpha^2 + C[2]\alpha + C[5] \\ \iota = C[0]\alpha^2 + C[3]\alpha + C[6] \\ \delta = C[1]\alpha^2 + C[4]\alpha + C[7] \\ \alpha = (P/10^6)^{1/4} \end{cases} \tag{F.7}$$

Where P is the vapor pressure, and the saturation coefficients C are given by equation (F.5).

F.3 Liquid temperature model

The liquid temperature model depends on the droplet radius r. If $r = 0$, then $T_l = T$, i.e., the liquid temperature is equal to that of the gas/vapor phase. On the other hand, if $r > 0$, then the liquid temperature is given by

$$T_l = \max\left\{T, T_{sat}\left[1 - \left(1 - \frac{T}{T_{sat}}\right)\frac{r_c}{r}\right]\right\} \tag{F.8}$$

Where T is the gas temperature, T_{sat} is the saturation temperature, r_c is the critical radius, and r is the droplet radius.

F.4 Liquid density model

The liquid density model is given by

$$\rho_l = R[0] + R[1]\left(\frac{T_l}{T_{sat}}\right) + R[2]\left(\frac{T_l}{T_{sat}}\right)^2 + R[3]\left(\frac{T_l}{T_{sat}}\right)^3 \tag{F.9}$$

Where T_l is the liquid temperature, T_{sat} is the saturation temperature. The coefficients $R[0]$, $R[1]$, $R[2]$, and $R[3]$ are given by

$$\mathbf{R} = \begin{bmatrix} R[0] \\ R[1] \\ R[2] \\ R[3] \end{bmatrix} = \begin{bmatrix} 928.08 \\ 464.63 \\ -568.46 \\ -255.17 \end{bmatrix} \tag{F.10}$$

F.5 Liquid enthalpy model

The liquid enthalpy model implemented on the SU2 branch is

$$h_l = h_v - \left[H[0] + H[1]\frac{T_l}{T_{sat}} + H[2]\left(\frac{T_l}{T_{sat}}\right)^2 + H[3]\left(\frac{T_l}{T_{sat}}\right)^3\right] \tag{F.11}$$

Where h_v is the vapor enthalpy, T_l is the liquid temperature, T_{sat} is the saturation temperature, and the coefficients $H[0]$, $H[1]$, $H[2]$, and $H[3]$ are given by

$$\mathbf{H} = \begin{bmatrix} H[0] \\ H[1] \\ H[2] \\ H[3] \end{bmatrix} = \begin{bmatrix} 3.8788 \times 10^6 \\ -5.9196 \times 10^6 \\ 8.8253 \times 10^6 \\ -5.9584 \times 10^6 \end{bmatrix} \tag{F.12}$$

F.6 Surface tension model

The default surface tension model available on the SU2 branch is the Vargaftik, Volkov, Voljak surface tension model Vargaftik et al. (1983-07) which is given by

$$\boxed{\sigma = B\left(1 - \frac{T}{T_c}\right)^{\mu}\left[1 + b\left(1 - \frac{T}{T_c}\right)\right]} \tag{F.13}$$

where $B = 0.2358$ N/m, $b = -0.625$, $\mu = 1.236$, and $T_c = 647.15$ K.

APPENDIX G – NOZZLE GEOMETRY

G.1 Moses & Stein Moses and Stein (1978)

The nozzle geometry used in the simulations was based on Moses's Moses and Stein (1978). In the original work the nozzle is three-dimensional and has a rectangular section. In this work a two-dimensional nozzle was used. The nozzle geometry[1] is given in table.

Table 11: Moses Moses and Stein (1978) nozzle geometry

Point	x (m)	y (m)
1	0.00000	0.02000
2	0.00012	0.01990
3	0.00654	0.01574
4	0.01320	0.01188
5	0.02059	0.00883
6	0.02798	0.00680
7	0.03367	0.00599
8	0.03924	0.00569
9	0.04917	0.00538
10	0.06880	0.00518
11	0.08091	0.00528
12	0.09629	0.00569
13	0.11676	0.00640
14	0.12960	0.0071
15	0.14329	0.0082
16	0.16000	0.0099

---

[1] I would like to thank my colleague and PhD candidate Ulisses A. Silva for allowing me to use this nozzle geometry - which he made himself - in my simulations.

G.2 Moore B nozzle Moore et al. (1973)

The (x, y) points of Moore B nozzle Moore et al. (1973) are given in table 12. These points were taken from Yang and Shen (2009) and they were used in the simulations of Moore B nozzle in the present work.

Table 12: Moore B nozzle Moore et al. (1973) geometry obtained from Yang and Shen (2009).

Point	x (m)	y (m)
1	-0.25	0.05635
2	-0.20	0.05635
3	0.00	0.05000
4	0.05	0.07200